
**Towards personalized internal radionuclide therapies
with ^{90}Y SIRT and ^{177}Lu -PSMA: an investigation of
3D image based dosimetry**

Julia Franziska Brosch-Lenz geb. Brosch



2021

Aus der Klinik und Poliklinik für Nuklearmedizin
des LMU Klinikums
der Ludwig-Maximilians-Universität München
Direktor: Prof. Dr. med. Peter Bartenstein

**Towards personalized internal radionuclide therapies
with ^{90}Y SIRT and ^{177}Lu -PSMA: an investigation of
3D image based dosimetry**

Julia Franziska Brosch-Lenz geb. Brosch

Kumulative Dissertation
zum Erwerb des Doktorgrades der Naturwissenschaften (Dr. rer. nat.)
an der Medizinischen Fakultät
der Ludwig-Maximilians-Universität München

vorgelegt von
Julia Franziska Brosch-Lenz geb. Brosch
aus München

2021

Mit Genehmigung der Medizinischen Fakultät
der Universität München

Betreuer: Priv. Doz. Dr. rer. nat. Guido Böning
Zweitgutachter: Prof. Dr. rer. nat. Michael Ingrisch
Dekan: Prof. Dr. med. dent. Reinhard Hickel
Tag der mündlichen Prüfung: 16.07.2021

Eidesstattliche Versicherung

Brosch-Lenz geb. Brosch, Julia Franziska

Ich erkläre hiermit an Eides statt,

dass ich die vorliegende Dissertation mit dem Titel

*Towards personalized internal radionuclide therapies with ^{90}Y SIRT and ^{177}Lu -PSMA:
an investigation of 3D image based dosimetry*

selbständig verfasst, mich außer der angegebenen keiner weiteren Hilfsmittel bedient und alle Erkenntnisse, die aus dem Schrifttum ganz oder annähernd übernommen sind, als solche kenntlich gemacht habe und nach ihrer Herkunft unter Bezeichnung der Fundstelle einzeln nachgewiesen habe.

Ich erkläre des Weiteren, dass die hier vorgelegte Dissertation nicht in gleicher oder in ähnlicher Form bei einer anderen Stelle zur Erlangung eines akademischen Grades eingereicht wurde.

Julia Brosch-Lenz geb. Brosch

München, 19.07.2021

Contents

Eidesstattliche Versicherung	v
Contents	viii
Nomenclature	x
List of publications	xi
Abstract	xv
Zusammenfassung	xvii
1 Introduction	1
2 Background	5
2.1 General concept of radiation therapy	5
2.2 General aspects of cancer therapies in nuclear medicine	7
2.3 Selected cancer therapies	8
2.3.1 Yttrium-90 SIRT of liver malignancies	8
2.3.2 Lutetium-177-PSMA therapy for prostate cancer	10
2.4 The concept of image based dosimetry	12
2.4.1 1) Quantitative activity measurement	14
2.4.2 2) Identification of organs and tumors	16
2.4.3 3) Fit of model function to data points	17
2.4.4 4) Conversion to dose	18
3 Studies	23
3.1 Motivation of this work	23
3.2 Yttrium-90 SIRT	24
3.2.1 Challenges in SIRT dosimetry	24
3.2.2 Preliminary phantom studies for quantitative imaging within the therapy workflow of ⁹⁰ Y SIRT	27
3.2.3 Investigation of the impact of the underlying activity imaging method on absorbed dose estimates for ⁹⁰ Y SIRT of hepatocel- lular carcinoma	32
3.3 Lutetium-177-PSMA therapy	37
3.3.1 Challenges in ¹⁷⁷ Lu-PSMA therapy dosimetry	37
3.3.2 Preliminary work for 3D time-integrated activity map creation . .	39

3.3.3	Impact of dosimetry method on absorbed dose estimate for bone lesions for ^{177}Lu -PSMA therapy of patients with mCRPC	41
4	Contributions to the original publications included in this work	47
5	Discussion	49
6	Conclusion	55
7	Publication I	57
8	Publication II	69
	Bibliography	93
	Danksagung	99

Nomenclature

3D	Three Dimensional
BRS	Bremsstrahlung
CT	Computed Tomography
D75	Minimum Absorbed Dose To 75 % Of The VOI Volume
DVH	Dose Volume Histogram
EANM	European Association Of Nuclear Medicine
FOV	Field Of View
HCC	Hepatocellular carcinoma
^{166}Ho	Holmium-166
HU	Hounsfield Unit
^{131}I	Iodine-131
ICRP	International Commission On Radiological Protection
ICRU	International Commission on Radiation Units and Measurements
^{177}Lu	Lutetium-177
MAA	Macroaggregated Albumin
MAP	Maximum A Posteriori
MC	Monte Carlo
mCRPC	Metastatic, Castration-Resistant Prostate Cancer
MELP	Medium-Energy-Low-Penetration
MIRD	Medical Internal Radiation Dose
MR	Magnetic Resonance
OAR	Organ At Risk
p.i.	Post Injection
PD	Percentage Difference
PET	Positron Emission Tomography
PSMA	Prostate Specific Membrane Antigen
QSPECT	Quantitative SPECT
RC	Recovery Coefficient
SIRT	Selective Internal Radiation Therapy
SNR	Signal-To-Noise-Ratio
SPECT	Single Photon Emission Computed Tomography
$^{99\text{m}}\text{Tc}$	Technetium-99m
TIAM	Time-Integrated Activity Map
TOF	Time-Of-Flight
TSV	Tumor S Value
VOI	Volume Of Interest
VSV	Voxel S Value
^{90}Y	Yttrium-90
^{90}Zr	Zirconium-90

List of publications

Original publications

The following two original publications are subject of this cumulative dissertation in accordance with the promotion regulation for natural sciences of the medical faculty of the Ludwig-Maximilians-University Munich.

J. Brosch, A. Gosewisch, L. Kaiser, M. Seidensticker, J. Ricke, J. Zellmer, P. Bartenstein, S. Ziegler, H. Ilhan, A. Todica, and G. Böning. "3D image-based dosimetry for Yttrium-90 radioembolization of hepatocellular carcinoma: Impact of imaging method on absorbed dose estimates." *Physica Medica*, 80, 2020.
<https://doi.org/10.1016/j.ejmp.2020.11.016>

J. Brosch-Lenz, C. Uribe, A. Gosewisch, L. Kaiser, A. Todica, H. Ilhan, F. J. Gildehaus, P. Bartenstein, A. Rahmim, A. Celler, S. Ziegler, and G. Böning. "Influence of dosimetry method on bone lesion absorbed dose estimates in PSMA therapy: application to mCRPC patients receiving Lu-177-PSMA-I&T." *EJNMMI Physics*, 8, 2021.
<https://doi.org/10.1186/s40658-021-00369-4>

Further original publications

A. Delker, H. Ilhan, C. Zach, **J. Brosch**, F.-J. Gildehaus, S. Lehner, P. Bartenstein, and G. Böning. "The influence of early measurements onto the estimated kidney dose in [177 Lu][DOTA 0, Tyr 3] Octreotate peptide receptor radiotherapy of neuroendocrine tumors." *Molecular Imaging and Biology*, 17(5), 2015.

<https://doi.org/10.1007/s11307-015-0839-3>

A. Gosewisch, A. Delker, S. Tattenberg, H. Ilhan, A. Todica, **J. Brosch**, L. Vomacka, A. Brunegraf, F. J. Gildehaus, S. Ziegler, P. Bartenstein, and G. Böning. "Patient-specific image-based bone marrow dosimetry in Lu-177-[DOTA 0, Tyr 3]-Octreotate and Lu-177-DKFZ-PSMA-617 therapy: investigation of a new hybrid image approach." *EJNMMI Research*, 8(1), 2018.

<https://doi.org/10.1186/s13550-018-0427-z>

L. Vomacka, M. Unterrainer, A. Holzgreve, E. Mille, A. Gosewisch, **J. Brosch**, S. Ziegler, B. Suchorska, F.-W. Kreth, J.-C. Tonn, P. Bartenstein, N. L. Albert, and G. Böning. "Voxel-wise analysis of dynamic 18 F-FET PET: a novel approach for non-invasive glioma characterisation." *EJNMMI Research*, 8(1), 2018.

<https://doi.org/10.1186/s13550-018-0444-y>

A. Gosewisch, H. Ilhan, S. Tattenberg, A. Mairani, K. Parodi, **J. Brosch**, L. Kaiser, F. J. Gildehaus, A. Todica, S. Ziegler, P. Bartenstein, and G. Böning. "3D Monte Carlo bone marrow dosimetry for Lu-177-PSMA therapy with guidance of non-invasive 3D localization of active bone marrow via Tc-99m-anti-granulocyte antibody SPECT/CT." *EJNMMI Research*, 9(1), 2019.

<https://doi.org/10.1186/s13550-019-0548-z>

A. Gosewisch, M. Schleske, F. J. Gildehaus, I. Berg, L. Kaiser, **J. Brosch**, P. Bartenstein, A. Todica, H. Ilhan, and G. Böning. "Image-based dosimetry for 225 Ac-PSMA-I&T therapy using quantitative SPECT." *European Journal of Nuclear Medicine and Molecular Imaging*, 2020.

<https://doi.org/10.1007/s00259-020-05024-1>

X. Hou, **J. Brosch**, C. Uribe, A. Desy, G. Böning, J.-M. Beaugard, A. Celler, and A. Rahmim. "Feasibility of single-time-point dosimetry for radiopharmaceutical therapies." *Journal of Nuclear Medicine*, 2020.

<https://doi.org/10.2967/jnumed.120.254656>

F. Völter, L. Mittlmeier, A. Gosewisch, **J. Brosch-Lenz**, F. J. Gildehaus, M. Zacherl, L. Beyer, C. Stief, A. Holzgreve, J. Rübenthaler, C. Cyran, G. Böning, P. Bartenstein, A. Todica, and H. Ilhan. "Correlation of an index-lesion based SPECT dosimetry method with mean tumor dose and clinical outcome after ^{177}Lu -PSMA-617 radioligand therapy." *Diagnostics*, 11(3), 2021.
<https://doi.org/10.3390/diagnostics11030428>

Conference abstracts

J. Brosch, A. Gosewisch, A. Delker, P. Bartenstein, H. Ilhan, A. Todica, and G. Böning. "Vergleich einer vereinfachten, quantitativen Yttrium-90 Bremsstrahlung-SPECT Rekonstruktion mit Yttrium-90 PET hinsichtlich der Quantifizierbarkeit für die Dosimetrie." *Nuklearmedizin* 57, 2018.

J. Brosch, A. Gosewisch, A. Delker, P. Bartenstein, A. Todica, H. Ilhan, and G. Böning. "Untersuchung einer vereinfachten quantitativen Yttrium-90 Bremsstrahlung-SPECT Rekonstruktion unter Verwendung von Untergrundkompensation und patientenspezifischen Kalibrationsfaktoren." *Nuklearmedizin*, 57, 2018.

J. Brosch, A. Gosewisch, A. Delker, L. Vomacka, P. Bartenstein, H. Ilhan, A. Todica, and G. Böning. "Comparison of a simplified quantitative yttrium-90 bremsstrahlung SPECT reconstruction with yttrium-90 PET in terms of quantification for dosimetry of SIR-therapy in the liver." *European Journal of Nuclear Medicine and Molecular Imaging*, 45, suppl. 1, 2018.

J. Brosch, A. Gosewisch, A. Delker, L. Vomacka, P. Bartenstein, A. Todica, H. Ilhan, and G. Böning. "Investigation of a simplified quantitative yttrium-90 bremsstrahlung SPECT reconstruction by usage of background compensation and patient-specific calibration factors for yttrium-90 SIRT dosimetry." *European Journal of Nuclear Medicine and Molecular Imaging*, 45, suppl. 1, 2018.

J. Brosch, A. Gosewisch, L. Kaiser, P. Bartenstein, H. Ilhan, A. Todica, and G. Böning. "3D image-based dosimetry for Yttrium-90 SIR-therapy of HCC: comparison of three different techniques." *Journal of Nuclear Medicine*, 60, suppl. 1, 2019.

J. Brosch, A. Gosewisch, H. von Zimmermann, L. Kaiser, P. Bartenstein, A. Todica, H.

Ilhan, and G. Böning. "Evaluation von Yttrium-90-PET und Yttrium-90-SPECT Phantommessungen angepasst an Messbedingungen von 20 SIRT Patienten." *Nuklearmedizin*, 58(02), 2019.

J. Brosch, A. Gosewisch, H. von Zimmermann, L. Kaiser, P. Bartenstein, H. Ilhan, A. Todica, and G. Böning. "Image-based 3D Dosimetry Techniques For Yttrium-90 SIRT Of HCC: Quantitative Comparison Of Tumor And Healthy Liver Absorbed Doses." *European Journal of Nuclear Medicine and Molecular Imaging*, 46, suppl. 1 2019.

J. Brosch, A. Gosewisch, C. Uribe, L. Kaiser, P. Bartenstein, S. Ziegler, and G. Böning. "Vergleich der Tumordosimetrie basierend auf Voxel-S-Wert-Kernen und Monte Carlo Simulation bei der Lu-177-PSMA Therapie von mCRPC Patienten mit ausgeprägter Knochenmetastasierung." *Nuklearmedizin*, 59(02), 2020.

J. Brosch, C. Uribe, A. Gosewisch, L. Kaiser, P. Bartenstein, A. Rahmim, A. Celler, S. Ziegler, and G. Boening. "Comparison of bone lesion dosimetry based on voxel S-values and Monte Carlo simulation for Lu-177-PSMA-therapy of mCRPC patients with pronounced bone metastases." *Proc. Annual AAPM Meeting*, 2020.

J. Brosch, C. Uribe, A. Gosewisch, L. Kaiser, P. Bartenstein, A. Todica, H. Ilhan, A. Rahmim, A. Celler, S. Ziegler, and G. Böning. "Lesion-wise dosimetry for multiple bone metastases in mCRPC patients undergoing Lu-177-PSMA therapy: comparison of five dosimetric methods." *European Journal of Nuclear Medicine and Molecular Imaging*, 47, suppl. 1, 2020.

J. Brosch, C. Uribe, A. Gosewisch, L. Kaiser, P. Bartenstein, A. Todica, H. Ilhan, A. Rahmim, A. Celler, S. Ziegler, and G. Böning. "Performance comparison of different dosimetry methods with respect to complexity and accuracy." *European Journal of Nuclear Medicine and Molecular Imaging*, 47, suppl. 1, 2020.

Abstract

Internal radionuclide therapies became a valuable treatment choice for various cancer types by now. The involvement of patient-individual, 3D image based dosimetry may offer the potential to improve tumor response and prevent therapy side-effects related to overdosing of organs at risk. However, a deeper insight into the heterogeneity of patient therapy responses is impeded by the lack of broadly available and reliable dosimetry data. So far, no standard for dosimetry nor for the therapy workflow was provided for the majority of internal radionuclide therapies, though they were introduced years ago. Further, the implementation of dosimetry into clinical routine and therapy workflow varies over Europe and Worldwide.

The complex processing, which is required for 3D image based dosimetry, hinder its routine realization towards personalized therapy. The required processing steps include 1) the quantitative imaging of the radiopharmaceutical distribution over time, 2) the co-registration of multi-modality image data, the segmentation of volumes of interests (i.e. tumors and organs at risk), 3) the determination of the total number of decays per volume of interest or per voxel, and 4) the conversion to absorbed dose estimates. Depending on the therapy, different challenges arise within these processing steps. Consequently, the aim of this work was to identify accurate 3D image based dosimetry that is applicable in the clinical therapy workflow of two different internal radionuclide therapies.

The dosimetry of the selective internal radiotherapy (SIRT) of liver tumors and metastases with ^{90}Y microspheres is hampered by the difficulty of quantitative imaging of ^{90}Y . Phantom experiments were carried out to improve image quantification and quality for both, ^{90}Y SPECT/CT and ^{90}Y PET/CT. The latter is affected by the low branching ratio of only $(31.86 \pm 0.47) \cdot 10^{-6}$ for internal pair production. However, ^{90}Y PET/CT still showed better activity quantification than SPECT/CT imaging of the broad energy distribution of the ^{90}Y bremsstrahlung spectrum that directly affects image acquisition and reconstruction. Since ^{90}Y PET/CT is not yet available in all centers that perform SIRT, an optimized scaled $^{99\text{m}}\text{Tc}/^{90}\text{Y}$ SPECT/CT dosimetry approach was developed. For this, as an alternative, the use of the pre-therapeutic $^{99\text{m}}\text{Tc}$ -MAA SPECT/CT image as a surrogate for ^{90}Y distribution for dosimetry was compared to ^{90}Y SPECT/CT and ^{90}Y PET/CT based dosimetry.

This analysis revealed a good comparability of healthy liver absorbed dose estimates independent of the underlying activity imaging method. However, ^{90}Y SPECT/CT showed a non-negligible underestimation of tumor absorbed dose estimates of $-50 \pm 13\%$ compared against ^{90}Y PET/CT based dosimetry. If no post-therapeutic PET/CT imaging is possible, the scaled $^{99\text{m}}\text{Tc}/^{90}\text{Y}$ SPECT/CT based dosimetry serves as an alternative with only $-2 \pm 18\%$ percentage difference in tumor absorbed dose estimates. It enables the

retrospective analysis of existing ^{90}Y SIRT data before ^{90}Y PET/CT was introduced.

The majority of presently available dosimetry methods rely on the simplification of assuming soft tissue for all absorbed dose estimation. This is questionable in the case of mCRPC patients receiving ^{177}Lu -PSMA therapy. These patients present with a large spread of metastases to the skeleton. Therefore dosimetry needs to address very heterogeneous tissue and density distributions. Thus, this work compared a broad spectrum of available dosimetry methods and their applicability in regions with heterogeneous densities, i.e. bone lesions. The investigation included the use of tumor S values, the application of voxel S values, both with and without lesion- or voxel-individual density weighting, and compared their results against a full patient-individual Monte Carlo (MC) absorbed dose estimation. The latter offers the potential to include patient-individual radiopharmaceutical and density distribution into absorbed dose simulation. The analysis of accuracy of absorbed dose estimation for bone lesions is essential to address heterogeneous therapy response of individual bone lesions for patients receiving ^{177}Lu -PSMA therapy.

The importance to account for heterogeneous density distribution was demonstrated during the evaluation of 289 bone lesions with an average lesion density of $1.25 \pm 0.11 \text{ g/cm}^3$. The results for bone lesion absorbed dose estimation showed improved comparability with the reference MC absorbed dose estimation, when a lesion- or voxel-individual density weighting was used rather than assuming fixed density with less than 10 % difference compared to MC absorbed dose simulation. Both, the use of tumor S values as well as the use of voxel S values with individual density weighting demonstrated a fast and accurate absorbed dose estimation for bone lesions in ^{177}Lu -PSMA therapy, with differences against MC of $-8 \pm 1 \%$ and $-2 \pm 1 \%$, respectively. Due to its computational requirements and additional processing, the full patient-individual Monte Carlo absorbed dose estimation likely remains a tool for research purposes. However, it supports the derivation of simplified absorbed dose estimation methods by assessing their capabilities to account for patient-individual 3D activity and density distributions.

Obtaining a deeper insight into possibilities and limitations of certain dosimetry approaches is necessary to understand patient-individual therapy response and to improve the outcome of internal radionuclide therapies. The promising findings of this work supported derivation of accurate absorbed dose estimation for ^{90}Y SIRT and ^{177}Lu -PSMA therapy. In the case of ^{90}Y SIRT of the liver, the proposed scaled $^{99\text{m}}\text{Tc}/^{90}\text{Y}$ SPECT/CT dosimetry approach encourages the derivation of dose-response analyses on existing patient data. The comparison of multiple dosimetry methods for bone lesion absorbed dose estimation for ^{177}Lu -PSMA therapy of mCRPC supports the comparability of reported dosimetry estimated from different institutions using different dosimetry methods. To conclude, the herein investigated approaches for 3D image based dosimetry offer the potential to be routinely performed in the clinics. And as a consequence, this might in future enable personalized internal radionuclide therapies with improved therapy response.

Zusammenfassung

Interne Radionuklidtherapien haben sich heutzutage zu einer wertvollen Therapieoption für verschiedene Krebsarten entwickelt. Hierbei bietet die Berücksichtigung von 3D bildbasierter Dosimetrie die Möglichkeit, das Therapieergebnis zu verbessern und Nebenwirkungen durch Überdosierung von Risikoorganen zu vermeiden. Jedoch wird ein tieferes Verständnis der heterogenen Therapieergebnisse der Patienten vor allem dadurch behindert, dass es nur wenig verlässliche Dosimetriedaten gibt. Für den Großteil der internen Radionuklidtherapien wurden keine Standards für die therapiebegleitende Bildgebung und Dosimetrie formuliert, obwohl diese teils seit Jahren durchgeführt werden. Des Weiteren variiert die Anwendung von Dosimetrie in der klinischen Routine in Europa und weltweit.

Die Komplexität der Arbeitsschritte, welche für 3D bildbasierte Dosimetrie benötigt werden, erschwert die Anwendung auf die Therapie in der Praxis und hat damit direkt Einfluss auf personalisierte Therapie. Die benötigten Arbeitsschritte umfassen: 1) die quantitative Bildgebung der Aktivitätsverteilung über die Zeit; 2) die Überlagerung der verschiedenen Bilddaten und die Segmentierung von Tumoren und Risikoorganen; 3) die Bestimmung der Gesamtzahl an Zerfällen je Zielregion oder pro Bildvoxel; und 4) die Abschätzung der absorbierten Dosis. In Abhängigkeit der Therapieform variiert die Schwierigkeit der einzelnen Schritte. Das Ziel dieser Arbeit war daher die Untersuchung der Komplexität der 3D bildbasierten Dosimetrie zweier unterschiedlicher Therapiearten.

Die Herausforderungen in der quantitativen Bildgebung von ^{90}Y erschweren die Dosimetrie der selektiven internen Radiotherapie (SIRT) von Lebertumoren und -metastasen mit ^{90}Y Mikrosphären. Zur Verbesserung von Bildqualität und Quantifizierung von ^{90}Y SPECT/CT und ^{90}Y PET/CT wurden Phantomstudien durchgeführt. Obwohl das ^{90}Y PET/CT durch die geringe Anzahl der internen Paarproduktion von nur 31.86 ± 0.47 bei einer Million Zerfällen erschwert wird, weist sie bessere Aktivitätsquantifizierungen auf als die SPECT/CT Bildgebung des Bremsstrahlungsspektrums von ^{90}Y . Letztere ist dahingehend limitiert, dass ein Photo-Peak während der SPECT-Akquisition und -Rekonstruktion angenommen wird. Da die post-therapeutische Bildgebung mit ^{90}Y PET/CT nicht in allen SIRT-Zentren möglich ist, wurde ein Dosiemetrieansatz auf einem skalierten $^{99\text{m}}\text{Tc}/^{90}\text{Y}$ SPECT/CT weiterentwickelt. Dieser Ansatz verwendet die Aktivitätsverteilung des prä-therapeutischen $^{99\text{m}}\text{Tc}$ -MAA SPECT/CTs als Ersatz für die therapeutische ^{90}Y Mikrosphärenverteilung und wurde gegen ^{90}Y SPECT/CT und ^{90}Y PET/CT basierte Dosimetrie verglichen.

Diese Untersuchung zeigte eine gute Vergleichbarkeit der geschätzten absorbierten Dosis im gesunden Lebergewebe unabhängig von der verwendeten Bildgebungsmethode. Für die Schätzung der absorbierten Dosis im Tumor zeigte die ^{90}Y SPECT/CT basierte Do-

simetrie eine nicht zu vernachlässigende Unterschätzung von $-50\pm 13\%$ gegenüber der auf ^{90}Y PET/CT geschätzten Dosis. Wenn die post-therapeutische Bildgebung nicht mittels ^{90}Y PET/CT erfolgen kann, liefert die Dosisschätzung auf einem skalierten $^{99\text{m}}\text{Tc}/^{90}\text{Y}$ SPECT/CT eine solide Alternative mit nur $-2\pm 18\%$ Abweichung der Tumordosis gegenüber der ^{90}Y PET/CT basierten Dosisschätzung. Dieser Dosimetrieansatz ermöglicht des Weiteren die retrospektive Auswertung bestehender ^{90}Y Datensätze ohne ^{90}Y PET/CT.

Der Großteil der bestehenden Dosimetrieansätze beinhaltet die vereinfachte Annahme von ausschließlich Weichteilgewebe bei der Schätzung der absorbierten Dosis. Diese Herangehensweise ist fraglich in der Anwendung bei Patienten mit mCRPC, die die ^{177}Lu -PSMA Therapie erhalten. Diese Patienten weisen bereits eine ausgedehnte Metastasierung im Skelett auf, wodurch der Dosimetrieansatz auch in Regionen mit heterogener Gewebe- und Dichteverteilung geeignet sein muss. Daher untersuchte diese Arbeit ein großes Spektrum von verfügbaren bildbasierten Dosimetrieansätzen und verglich ihre Anwendung auf Regionen mit heterogener Dichte, d.h. für Knochenläsionen. Das beinhaltete die Anwendung von Tumor-S-Werten, die Verwendung von Voxel-S-Werten - jeweils mit und ohne Dichtegewichtung auf Läsions- bzw. Voxel Ebene - und verglich alle Ansätze mit Patienten-individueller Monte Carlo (MC) Dosimetriesimulation. Letztere bietet die Möglichkeit sowohl die Patienten-individuelle Verteilung der zeit-integrierten Aktivität als auch die Dichte bei der absorbierten Dosis zu berücksichtigen. Die genaue Analyse der Dosisabschätzung für Knochenläsionen ist essentiell, um die heterogene und teils Läsions-individuelle Therapieantwort der Patienten bei der ^{177}Lu -PSMA Therapie zu verstehen.

Die Analyse von 289 Knochenläsionen mit einer mittleren Dichte von $1.25\pm 0.11\text{ g/cm}^3$ unterstrich die Bedeutung, die heterogene Dichteverteilung bei der Dosimetrie zu berücksichtigen. Die Ergebnisse zeigten eine verbesserte Vergleichbarkeit der verschiedenen Dosimetrieansätze, wenn eine Dichtegewichtung auf Läsions- bzw. Voxel Ebene anstatt mit einer konstanten Dichte verwendet wurde, mit weniger als 10% Abweichung zur MC Dosimetriesimulation. Die Verwendung von Tumor-S-Werten als auch Voxel-S-Werten mit Dichtegewichtung repräsentieren eine schnelle und präzise Dosisschätzung für Knochenläsionen bei der ^{177}Lu -PSMA Therapie mit Abweichungen von $-8\pm 1\%$ bzw. $-2\pm 1\%$ gegenüber MC. Durch die aufwendigen Anforderungen und zusätzlichen Verarbeitungsschritte für die Berechnung, bleibt die Anwendung von MC Dosimetriesimulationen voraussichtlich auf die Forschung beschränkt. Jedoch unterstützt sie die Entwicklung vereinfachter Dosimetriemethoden hinsichtlich ihrer Berücksichtigung von Patienten-individueller 3D Aktivitäts- und Dichte-/Gewebeverteilungen.

Ein fundiertes Verständnis der Limitationen und Möglichkeiten einzelner Dosimetrieansätze ist unverzichtbar, um die Patienten-individuelle Therapieantwort besser zu verstehen und damit die Ergebnisse von interner Radionuklidtherapie zu verbessern. Die vielversprechenden Ergebnisse dieser Arbeit unterstützen das Definieren von akkurater Dosimetrie der ^{90}Y SIRT sowie der ^{177}Lu -PSMA Therapie. Der skalierte $^{99\text{m}}\text{Tc}/^{90}\text{Y}$ SPECT/CT Dosimetrieansatz ermöglicht Dosis-Wirkungs-Analysen von bestehenden ^{90}Y SIRT Datensätzen. Der umfangreiche Vergleich verschiedener Dosimetrieansätze für Knochenläsionen bei der ^{177}Lu -PSMA Therapie von mCRPC unterstützt die Einordnung von publizierten Dosiswerten verschiedener Institutionen mit unterschiedlichen Dosimetriemethoden. Zusammenfassend können die in dieser Arbeit untersuchten 3D bildba-

sierten Dosimetrieansätze in der klinischen Routine Anwendung finden. Das begünstigt zukünftige personalisierte Radionuklidtherapien mit einem verbessertem Therapieansprechen.

Chapter 1

Introduction

Cancer related deaths are amongst the most frequent deaths in Germany with increasing numbers of newly diagnosed cases per year. A report of the Robert-Koch-Institute, which is published every 5 years, estimates that there were almost 500.000 new cancer cases in Germany in 2016 [1]. When distinguishing between cancer types, there were 57.370 new diagnosed prostate carcinomas in Germany in 2014 with around 13.900 related deaths in 2015 [2]. The prognosis of new prostate carcinomas in 2020 is 66.800, when assuming a constant rate of new diseases between 2013 and today [1]. When regarding at other cancer types, e.g. hepatocellular carcinomas (HCC), the number of newly diagnosed cases in Germany in 2014 is smaller with 5730 cases but with 4416 HCC related deaths in 2015 [3]. Moreover, the five-year survival rates determined between 2012 and 2014 varied significantly between these two cancer types, being 16 % for HCC [3] while being 91 % for prostate cancer [2].

The available strategies for disease treatment depend on the cancer type, the cancer classification and grading, and on the patient's constitution. Resection of the tumor, chemotherapy, external beam radiation therapy, and nuclear medicine radionuclide therapy are among the applied techniques. As a matter of fact, in many cases the sole application of a single technique did not provide sufficiently strong therapeutic effects, and consequently the treatment strategies involve appropriate combinations thereof. The individual therapy decision is made by experienced physicians based on guidelines and is adapted to the patient's wishes [1].

Regarding at nuclear medicine therapies, there is a long history of using radioisotopes for therapy of malignancies. Beginning in the 1940s, Iodine-131 (^{131}I) is used for therapy of thyroid cancer based on the uptake of iodine in the physiology of the thyroid gland [4]. Internal radionuclide therapy relies on the principle of absorbed radiation based damage to the DNA of cells. The concept exploits the accumulation of a radiopharmaceutical at tumor sites, and with that local irradiation of tumors. Physiological processes and direct binding to cancer cell receptors are assessed during radio-pharmaceutical design. The use of β^- or α emitters allows for high absorbed radiation doses in proximity of the radionuclide accumulation in the tumor cells. Nowadays, various different internal radionuclide therapies for different diseases exist and a total of 37476 therapies was performed in Germany in 2015 [5]. A detailed survey on radionuclide therapies was conducted in Europe in 2016 with 12 responding centres from Germany [6]. It revealed that there were 708 therapies with Lutetium-177 (^{177}Lu) targeting the prostate specific

membrane antigen (PSMA) for prostate cancer patients in Germany in 2015 [6]. ^{177}Lu -PSMA is a therapy that was first introduced in 2013 [7] and is performed in the late stage of the disease in individual patient cases. Another example is the selective internal radiation therapy (SIRT) with Yttrium-90 (^{90}Y) labelled microspheres for liver tumors such as HCC or liver metastases with 1605 therapies in Germany in 2015 [5]. As an example, the total treatment numbers of ^{90}Y SIRT and ^{177}Lu -PSMA in our institution in 2015 compared to 2020 are given in figure 1.1 (p. 2).

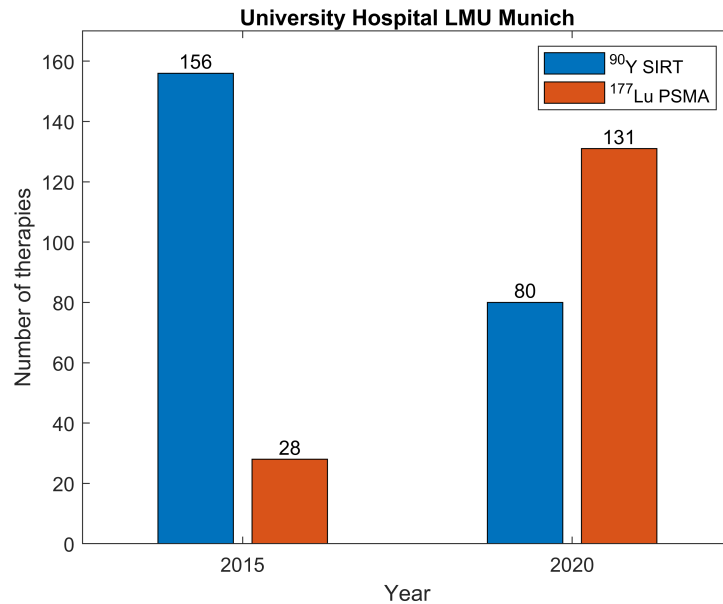
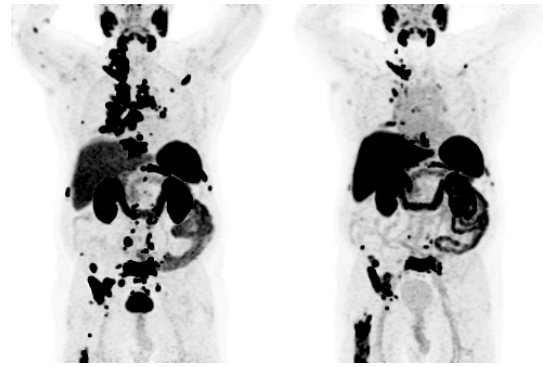
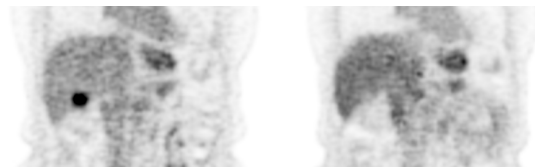


Figure 1.1: Therapy numbers of ^{90}Y SIRT and ^{177}Lu -PSMA for 2015 compared against 2020 in the university hospital of LMU Munich.

The great interest of research and clinics in nuclear medicine therapies such as SIRT, peptide receptor radionuclide therapy or radioligand therapy is motivated by the promising results of therapy response and minimal therapy side effects compared to other therapy forms [8] [9] [10]. Figure 1.2 (p. 3) illustrates the response to ^{177}Lu -PSMA and ^{90}Y SIRT therapy of two exemplary patients on their pre- and post-therapeutic combined positron emission tomography (PET) and computed tomography (CT) images, both showing a decrease in radiopharmaceutical uptake. However, there remains a risk of damaging healthy cells and organs besides the tumor cells during internal radionuclide therapy. Depending on the severity of the damage, this could cause severe side effects influencing the overall survival and affecting the patient's quality of life. Therefore, it is indispensable to determine the amount of radioactivity that can be delivered to the patient during therapy with minimalized risk of healthy tissue damage. Therapy optimization would hence imply to maximize absorbed dose to tumors whilst minimizing absorbed dose to organs at risk (OAR). As such, the optimization is emphasized in article 56 of the European council directive 2013/59/Euratom with the goal to optimise, plan and verify absorbed dose to target and non-target regions during radionuclide therapies [11].



(a) Maximum intensity projection highlighting the decrease in activity uptake and size of the metastases of a prostate cancer patient pre- and after 4 cycles of ^{177}Lu -PSMA therapy.



(b) Coronal slice showing the total decrease in activity uptake of the liver lesion after receiving ^{90}Y SIRT.

Figure 1.2: Exemplary patient therapy response on pre- and post-therapeutic PET/CT images.

To achieve the goal of therapy optimization, patient-individual absorbed dose estimation for tumors and OARs is required - pre- and post-therapeutically. The derivation of dose-response relationships will then allow for therapy activity planning towards personalized internal radionuclide therapies. For this, the absorbed dose calculation needs to account for patient-individual anatomy and radionuclide accumulation during therapy. Currently, very little absorbed dose calculation is implemented in clinical routine. Existing absorbed dose estimation often suffers from simplifications and is not yet patient-individual. However, to facilitate the implementation of dosimetry into clinical routine, the workflow needs to remain simple and fast at an acceptable level of accuracy. This trade-off is crucial when addressing patient's safety.

The aim of this work is to improve the target and OAR dose estimation with respect to patient-individual anatomy, radionuclide distribution and kinetics during internal radionuclide therapy. For this purpose, two nuclear medicine therapies with completely different therapy procedure were chosen: Selective Internal Radiotherapy with ^{90}Y microspheres for liver tumors and metastases, and ^{177}Lu -PSMA radioligand therapy for metastasized prostate cancer. Each of the examined therapies has its own challenges hindering accurate patient-individual absorbed dose estimation. The motivation of choosing ^{90}Y SIRT was the difficulty in acquiring post-therapeutic quantitative activity distribution images of the patients for absorbed dose calculation. ^{177}Lu -PSMA therapy was chosen since the patients receiving ^{177}Lu -PSMA therapy often present with a large spread of metastases in the skeleton, which directly influences the target absorbed dose estimation.

Chapter 2

Background

2.1 General concept of radiation therapy

Radiation therapy - external and internal - makes use of the radiation-induced damage to tissue caused by the interaction of ionizing radiation with matter. The effects occur within different stages at different timescales: a physical, a physical-chemical, a chemical and a biological phase, compare with the approximate orders of magnitude in figure 2.1 (p. 5) [12] [13].

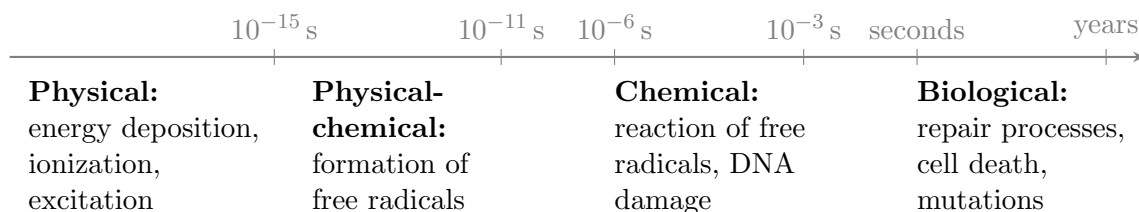


Figure 2.1: Different stages within the effect of ionizing radiation on tissue.

The radiation effect on the cell nucleus can be categorized into (i) direct effects, stemming from the direct physical interactions with the DNA, and (ii) indirect effects stemming from the chemical reactions of free radicals with the DNA. Free radicals, which are produced when a water molecule in the cell is ionized are highly chemically reactive and can diffuse to the DNA [13]. The possible DNA damages range from a base damage over single strand breaks (SSB) to double strand breaks (DSB). Amongst these, DSB are most complex to repair and when repair mechanisms fail, this can lead to cell death [14]. The radiation effect on a cell with $10 \mu\text{m}$ diameter is as follows: 1 Gy (radiation dose estimated via the absorbed energy per unit of mass) leads to 10^5 ionizations, producing over 1000 base damages, over 1000 SSBs, and max. 40 DSBs [12] [15]. However, this causes cell death in just 30% of cells due to biological repair processes [12].

Nuclear medicine therapies exploit the spontaneous transition of unstable radioisotopes into more stable ground states via emission of ionizing radiation. Common therapeutic radionuclides undergo β^- decay (e.g. ^{90}Y , ^{177}Lu , and Holmium-166 (^{166}Ho) [16]). Along their path through tissue, the β^- particles experience interactions with the Coulomb

fields of the atoms of the matter. Interactions with either the Coulomb field of the electronic shell or the atomic nucleus of the interaction medium atoms are possible. Elastic or inelastic scattering of the radiation particle and ionization of the interaction atoms are amongst the results. The ionization energy of water is in the order of 10 eV [17], and with typical initial β^- energies from keV to MeV, they ionize up to 10^7 atoms along their path through tissue. Another kinetic energy loss is bremsstrahlung (BRS), when the charged particles are decelerated or deflected from their initial path. [18]

While it is desired to cause damage to tumor cells, it should be avoided to cause any damage to healthy tissue. Radiation therapy takes advantage of the fact that different tissue and tumor types obey different DNA damage repair capabilities [12]. With the maximum range in tissue of β^- particles being only a few millimetres (see ^{90}Y : $E_{\beta^-}^{max} = 2.28$ MeV, leading to $R_{\beta^-}^{max} = 11.3$ mm; ^{177}Lu : $E_{\beta^-}^{max} = 0.497$ MeV, leading to $R_{\beta^-}^{max} = 2$ mm [16]), this causes a concentrated damage in the proximity of the radionuclide accumulation.

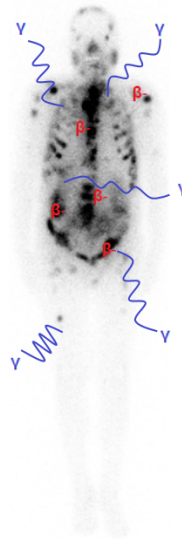


Figure 2.2: Schematic illustration of the concept of "theranostics": simultaneous emission of β^- , used for therapy, and γ , used for imaging.

Over the past few years, so-called "theranostic radioisotopes" have gained increasing interest [19]. These have a certain probability for γ decay in addition to the β^- decay. The photons of the γ decay can interact with tissue via the photo-electric absorption, Compton scattering and pair production [18]. However, the uncharged photons are a very penetrating radiation and undergo very little interactions along their path through tissue, hence allowing to be detected outside the patient's body. This enables direct imaging of the therapeutic radionuclide distribution in the patient further allowing for patient-individual, image based dosimetry estimation, exemplarily illustrated in figure 2.2 (p. 6).

2.2 General aspects of cancer therapies in nuclear medicine

The general workflow for cancer therapies in nuclear medicine includes a pre-therapeutic part for diagnosis and the therapy part. The first part involves acquisition of all required images and clinical parameters for diagnosis, and enables a treatment decision. The actual therapy part includes the therapy planning, therapy administration and direct post-therapeutic imaging for therapy monitoring and to allow image based dosimetry estimation.

The details in pre-therapeutic and post-therapeutic parts can differ between nuclear medicine therapies. Different patient images such as CT or magnetic resonance (MR) imaging, PET/CT imaging or scintigraphy images as well as combinations thereof can be required for a therapy decision and to exclude contra-indications. The pre-therapeutic parts are of great importance to ensure a safe therapy and are usually described in therapy guidelines [20] [21]. When multiple therapy sessions or cycles are planned, it is important to repeat all necessary pre-therapeutic steps between therapies to avoid complications. Post-therapeutic dosimetry can further support the patient-individual adaption of the following therapy sessions to meet the goal of therapy optimization [11].

Nuclear medicine therapies make use of cancer cell specific receptors or of metabolic processes to bring the radiopharmaceutical directly to the tumor site. By β^- emitting radionuclides with a short range in tissue, the radiation-induced damage is concentrated locally within the radiopharmaceutical accumulation, compare with section 2.1. The therapy administration is in such a manner to exploit this unique therapy design. Therapy forms range from radioactive capsules for ^{131}I therapy of thyroid diseases to radioactive microspheres which are administered via a catheter into the tumor to cause a radioembolization effect. Radioligand or radioreceptor therapy compounds on the other hand are directly injected into the patient's blood circulation and bind to the tumor cells.

2.3 Selected cancer therapies

This work evaluates the absorbed dose estimation for two chosen cancer therapies in nuclear medicine. Hence, the following sections 2.3.1 and 2.3.2 will describe the details of the pre- and post-therapeutic parts for these two very different internal radionuclide therapies.

2.3.1 Yttrium-90 SIRT of liver malignancies

The selective internal radiotherapy (also termed radioembolization) of liver malignancies was first realized in the 1960s [22]. Ever since many studies investigating the use of ^{90}Y SIRT for different liver tumors and metastases from other primary cancers were conducted (see e.g. [22] [23] [24] [25]). Nowadays, it became a valuable therapy option for patients being ineligible for resection or who do not respond to other therapy forms [26]. As reported by Hellwig et al. [5], this yielded to more than 1500 therapies with ^{90}Y glass or resin microspheres in Germany in 2015. The potential of ^{90}Y SIRT is indicated in figure 2.3 (p. 8), where an observable decrease of lesion size on the follow-up MR image compared to the pre-therapeutic MR image demonstrates noticeable therapy response.

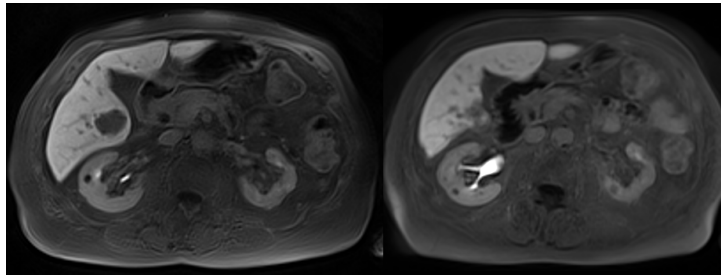


Figure 2.3: Patient example showing the therapy response 6 months after ^{90}Y SIRT on the right MR image.

The typical workflow for ^{90}Y SIRT is given in figure 2.4 (p. 9). Once a patient becomes eligible for ^{90}Y SIRT, it is mandatory to perform a therapy simulation to ensure a safe therapy delivery for the individual patient. This becomes necessary due to the possible risk of a reflux of the ^{90}Y microspheres to extra-hepatic regions such as the lungs [27]. Technetium-99m ($^{99\text{m}}\text{Tc}$)-macroaggregated albumin (MAA) is injected into the liver from the planned therapy catheter position with subsequent planar gamma camera and single photon emission computed tomography (SPECT)/CT imaging to evaluate this risk. The final therapy decision is made based on this treatment simulation. During SIRT, the ^{90}Y microspheres are administered via a catheter in the hepatic arteries directly into the liver tumors and metastases under fluoroscopic supervision. The therapy effect is obtained by two ways: (i) the embolization effect of the microspheres, and (ii) the irradiation from ^{90}Y [28]. The microspheres are fabricated out of resin or glass with a maximum diameter of $60\ \mu\text{m}$ [28]. By injecting these microspheres into the hepatic artery, an occlusion of the blood vessels occurs, which is blocking the tumor blood supply [29]. Further, ^{90}Y is a high energy β^- emitter with a maximum β^- range in tissue

of 11.3 mm [16]. This yields a high local energy deposition causing radiation damage to the tumor cells. As a rough estimation: one decay of ^{90}Y causes an absorbed dose of approximately $1.14 \cdot 10^{-10}$ Gy (compare with the S-values of OLINDA [30]) in a sphere of unit density with a volume of 1 ml, and a diameter of 12.4 mm, which is greater than the maximum β^- range in soft tissue usually obeying a density of 1. With typical average activity concentrations of 2 MBq/ml of ^{90}Y during SIRT, this would correspond to a total number of decays of $6.66 \cdot 10^{11}$ per millilitre, and thus to 75.8 Gy in the 1 ml sphere.

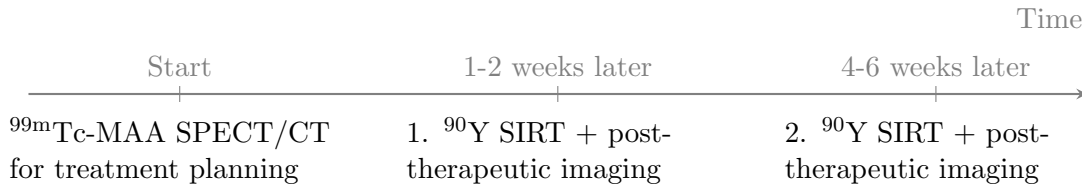


Figure 2.4: Time frame for ^{90}Y SIRT.

The actual SIRT is usually performed as a lobar or segmental therapy to spare healthy liver parenchyma. For bilobar tumor involvement, SIRT is performed separately for the left and right liver lobe according to the time frame in figure 2.4 (p. 9). This aims in allowing the healthy liver tissue to recover and potentially take over the function of the treated liver sections [28]. Each of the individual ^{90}Y SIRTs is routinely followed by post-therapeutic imaging within 24 h after microsphere administration to enable visual therapy administration success evaluation [26].

2.3.2 Lutetium-177-PSMA therapy for prostate cancer

The ^{177}Lu -PSMA therapy was first introduced for prostate cancer patients in Germany in 2013 [7]. It could be an option for patients for whom all existing approved therapy alternatives are exhausted. These patients are in the late stage of their disease and typically present with a large spread of metastases in lymph nodes and in the whole skeleton as shown in the patient example in figure 2.5 (p. 10).

However, the great value of ^{177}Lu -PSMA therapy is highlighted by figure 1.2(a) (p. 1.2(a)), showing the staging PET/CT images of a patient suffering from prostate cancer before and after receiving ^{177}Lu -PSMA therapy.

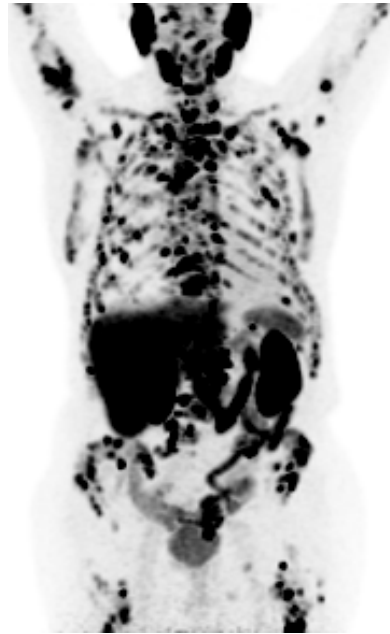


Figure 2.5: Prostate cancer metastasizes to lymph nodes and into the skeleton as demonstrated by this PSMA PET image of a patient.

^{177}Lu -PSMA is a radioligand therapy substance targeting the prostate specific membrane antigen. This antigen is specific for prostate cancer cells and increasingly expressed on prostate cancer cells [31]. It is therefore the ideal target for therapy. The overall principle of radioligand therapies is illustrated by the sketch in figure 2.6 (p. 11). The exact counterpart to the cancer cell specific antigen or receptor is used to allow for the direct binding of the radiopharmaceutical to the tumor cell. This counterpart is further labeled with a photon or positron emitting radionuclide to support diagnostic imaging or a α or β^- emitter being suitable for internal radionuclide therapy.

The strength of systemic therapy approaches, where the therapeutic substances is injected into the blood system, lies in their inherent capability to deliver the therapeutic selectively to the tumorous tissue throughout the patient's body. Patients presenting with a large and diffuse metastatic spread are ineligible for palliative external beam radiation therapy [32]. For these patients, and especially for patients suffering from metastatic, castration-resistant prostate cancer (mCRPC), ^{177}Lu -PSMA therapy became a valuable

option. According to the guidelines for prostate cancer treatment, all options of hormonal therapies and chemotherapy must have been exhausted for these patients, and further an image-proven uptake of PSMA ligands must be given [21].

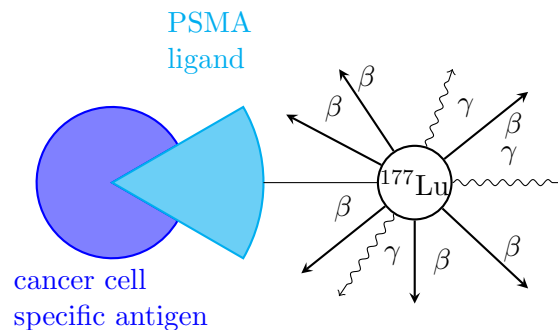


Figure 2.6: Schematic representation of the principle of radioligand therapies.

The kidneys as well as the bone marrow are amongst the critical OARs for all systemic therapies that are directly injected into the patient's blood system. Therefore, a kidney function test is recommended prior to ^{177}Lu -PSMA therapy, and all clinical parameters in addition to overall patient condition are precisely monitored. A patient solely becomes eligible for ^{177}Lu -PSMA therapy when therapy can be safely administered with respect to the kidney function test and the overall patient condition as deemed by the physician. The therapy is typically realized in multiple therapy cycles to prevent from exceeding the absorbed dose thresholds for OARs. This therapeutic scheme schedules the therapy cycles at six week intervals which enables close monitoring of kidney and bone marrow function between therapies. Furthermore, the therapy response can be monitored after each two cycles with PSMA PET/CT imaging. So far, the ^{177}Lu therapy activities are standardized values, which can be slightly adapted according to the patient's condition, kidney function, metastases spread and from therapy cycle to cycle. [21]

2.4 The concept of image based dosimetry

The first physical quantity towards radiation damage induced by interactions of ionizing radiation with tissue (compare with section 2.1), is the absorbed dose, given in Gray (Gy) [33]. The absorbed dose D is defined in line with report 85 of the International Commission on Radiation Units and Measurements (ICRU) [34] as the amount of absorbed energy dE per unit mass m , $D = dE/dm$, during interaction of radiation with tissue and is estimated based on quantitative imaging of the radionuclide distribution within the patient over time.

The estimation of absorbed dose to healthy tissue and tumors is necessary to improve patient-individual therapy and to prevent from therapy side effects caused by increased absorbed dose to healthy tissue.

In brief, the 3D image based estimation of absorbed dose can be categorized into the following steps in flowchart 2.7 (p. 12). [35]

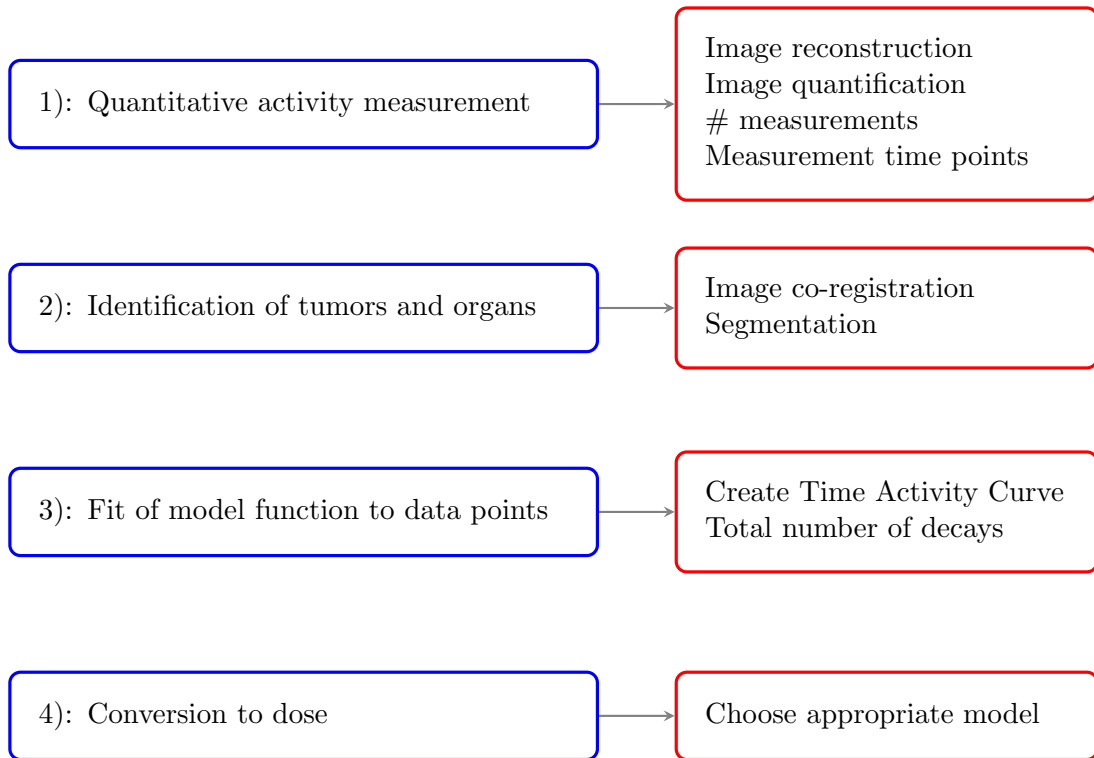


Figure 2.7: Required processing steps within the general dosimetry workflow.

The physical decay of a radionuclide follows the decay law,

$N(t) = N_0 \cdot e^{-\ln(2) \cdot t / t_{1/2}^{phys}}$. The initial number of unstable nuclei N_0 decays over time t according to the radionuclide specific physical half-life $t_{1/2}^{phys}$. Speaking of radioactivity, the decay rate is defined as $A(t) = -dN/dt(t)$, as the number of decays per time interval. Consequently, the formula for activity transforms to $A(t) = A_0 \cdot e^{-\ln(2) \cdot t / t_{1/2}^{phys}}$. The

resulting curve is of a mono-exponential shape, as illustrated in figure 2.8 (p. 13). [18]

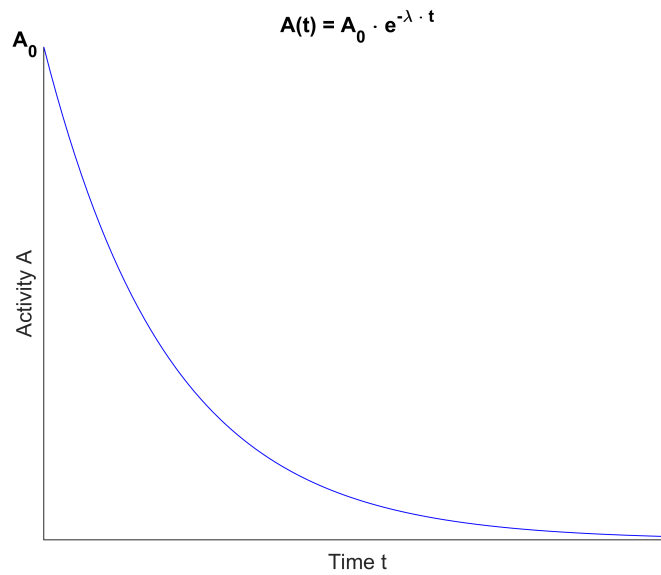


Figure 2.8: Example of the mono-exponential decay of activity when considering the physical half-life.

However, the situation in radionuclide therapies is more complex and the radionuclide, i.e. activity biodistribution in the patient's body, can vary over the time. A metabolism or biological excretion influences this distribution, hence yielding a biological half-life $t_{1/2}^{biol}$. The combination of biological half-life and physical half-life leads to a patient- and tissue-specific effective half-life $t_{1/2}^{eff}$ [36]. For all dosimetry estimations, it is necessary to determine this effective half-life on organ-, or voxel-level. The following sections 2.4.1 to 2.4.4 will describe the workflow of absorbed dose estimation in more detail.

2.4.1 1) Quantitative activity measurement

The mandatory pre-requisite for any absorbed dose estimation is to quantitatively measure the radioactivity distribution within the patient over time. These measurements can be done with either probes, gamma cameras, or with by SPECT [37] or PET imaging. The aim of these measurements is to obtain the above mentioned patient-individual effective half-life of the radiopharmaceutical in organs and tumors. Nuclear medicine imaging therefore enables an assessment of the biokinetic behaviour of the radiopharmaceutical in the patient. Figure 2.9(a) (p. 14) illustrates the measurement of activity over time assuming solely mono-exponential decay.

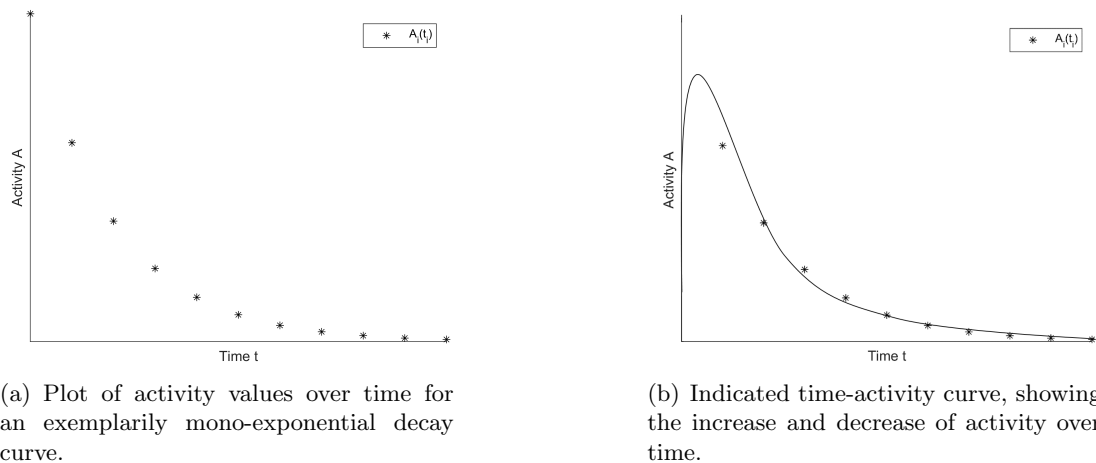


Figure 2.9: Illustrations of exemplarily activity values over time.

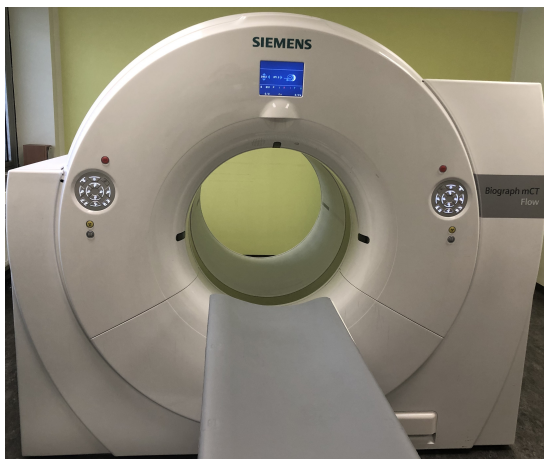
Figure 2.9(a) (p. 14) is showing a mono-exponential decay of the initial amount of activity over time in a specific region. Remembering the therapy principle of the ^{177}Lu -PSMA therapy described in section 2.3.2, this neglects the initial increase of radiopharmaceutical accumulation in the region of interest after injection. An exemplary activity curve showing this increase of activity is given in figure 2.9(b) (p. 14). However, the pharmacokinetic of a radiopharmaceutical can follow complex processes and it can potentially become very difficult to describe this curve. Consequently, the number and time point of the activity measurement has an impact on the determination of this curve. Usually, when a new radiopharmaceutical is introduced, the first patient's undergo multiple measurements at various time points to determine an appropriate measurement schedule. This is not only influenced by the pharmacokinetics of the radiopharmaceutical but also limited by the increased patient discomfort with increased number of measurements. This was for example investigated for the kidney absorbed dose estimation in ^{177}Lu -DOTATATE therapy by our group [38].

Assuming the appropriate time schedule for measurements has been determined for a certain radionuclide therapy, the measurement as such needs to be quantitative.

The term quantitative imaging in context of nuclear medicine describes the measurement of radioactive decay in units of Becquerel, which is in general not simple. Probes, gamma cameras, SPECT, and PET devices measure the emitted photons or annihila-

tion radiation from a radionuclide. These photons are subject to scatter and attenuation when traversing the patients body. The measured counts hence require a correction for attenuation and scatter. Nowadays, most of these corrections are based on the simultaneously acquired CT image of the patient which is converted into an attenuation map of the patient. The corrected measured counts are converted to units of activity in a next step. This is done via a calibration factor, which is obtained by measurements of known amounts of radioactivity. The detected counts of these measurements can thus be converted into activity values giving the calibration factor. Details of nuclear medicine imaging and reconstruction are described in the literature, e.g. by Simon Cherry et al. in [39].

Today's activity measurements often take advantage of tomographic imaging such as PET/CT and SPECT/CT (see photos 2.10(a) and 2.10(b), p. 15) revealing three dimensional (3D) activity distribution images of the patient on which this work on radionuclide therapy absorbed dose estimation is based.



(a) State of the art PET/CT.



(b) Example of a SPECT/CT.

Figure 2.10: Photos of a PET/CT and a SPECT/CT in the department of nuclear medicine of the LMU Klinikum.

2.4.2 2) Identification of organs and tumors

To determine the radioactivity distribution over time in organs and tumors, these need to be identified by segmentation on the quantitative activity images. Various options for segmentation and definition of volume of interests (VOI) exist [40]. The complexity varies from manual delineation on anatomical images such as MR or CT images to semi-automatic segmentation on functional images such as SPECT or PET.

To enable a transfer of the defined VOIs between images from different time points or modalities but for the same patient, the images need to be co-registered. A common form of co-registration in nuclear medicine images is the rigid registration to a chosen reference image [40]. This method for image registration makes use of rotation and translation to move and align the images to a fixed reference image. This can be applied inter- and intra-modality-wise.

Once the images from different time points are co-registered to each other, the VOIs can easily be copied to extract the activity per organ.

The patient example in image 2.11 shows the fused view of a co-registered CT and SPECT image with whole-body, kidney and tumor VOIs.

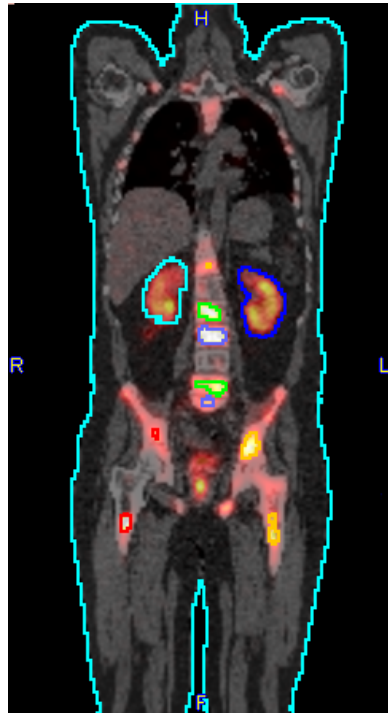


Figure 2.11: Patient example of fused CT and SPECT image and defined VOIs for whole-body, kidneys and tumors.

2.4.3 3) Fit of model function to data points

After completion of steps number 1) and 2) from figure 2.7 (p. 12), the next step aims in determination of the time-integrated activity per organ or tumor or per voxel. The time-integrated activity serves as input for all subsequent absorbed dose estimations in nuclear medicine therapies [41]. Thus, the calculation of total number of decays is essential for subsequent absorbed dose estimation.

The time-integrated activity per VOI or per voxel is calculated with formula $\tilde{A} = \int_0^{\infty} A(t)dt$. This implies the knowledge of the pharmacokinetic of the radiopharmaceutical over time. This includes knowledge of the patient-individual effective half-life, which can be estimated based on the patient activity images. The patient-individual half-life is assessed by fitting a selected model function to the obtained activity data points, compare to the curve from figure 2.9(b) (p. 14). Common fitting includes either a mono- or bi-exponential fit model.

The subsequent time-integration of the model function yields to the time-integrated activity \tilde{A} , compare with the gray area in figure 2.12, i.e. the total number of decays per organ or per voxel. The generation of voxel-wise time-integrated activity images allows for 3D absorbed dose estimation, although being potentially influenced by image artefacts or noise in individual voxels.

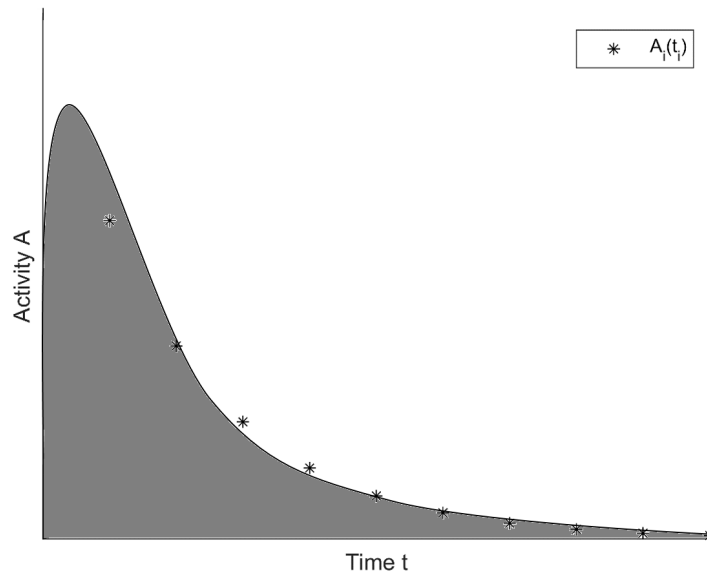


Figure 2.12: Illustration of the determination of the time-integrated activity \tilde{A} per organ or per voxel.

2.4.4 4) Conversion to dose

Step number 3) from figure 2.7 (p. 12) reveals the time-integrated activity per organ or per voxel. This enables absorbed dose estimation incorporating the biodistribution of the radionuclide and the physics of the radionuclide [42]. Multiple dosimetry methods with different pre-requisites, processing steps, complexity, and accuracy are available. This work examines the three dosimetry methods of particular interest in nuclear medicine: the organ S value approach - described by the committee of Medical Internal Radiation Dose (MIRD) [43], the voxel S value (VSV) approach from MIRD [44], and the full patient-individual Monte Carlo (MC) absorbed dose simulation.

An overview of the above mentioned dosimetry methods is given in table 2.1 (p. 18). To summarize, the organ S value approach assumes homogeneous activity distribution and tissue composition, while the VSV approach is applicable to non-uniform activity distributions on a voxel-level, while assuming a homogeneous medium. The full patient-individual MC simulation is capable to account for heterogeneous activity distribution and heterogeneous patient anatomy during absorbed dose simulation. The choice of dosimetry method strongly depends on the radionuclide therapy and field of application or area of interest. [36]

Organ S value	Voxel S value	MC absorbed dose simulation
$D_t = \sum_{s=1}^N \tilde{A} \cdot S_{s \rightarrow t}$	$D(x, y, z) = (\tilde{A} * VSV)(x, y, z)$	3D MC simulation
– Homogeneous activity distribution	+ Heterogeneous activity distribution	+ Heterogeneous activity distribution
– Homogeneous medium	– Homogeneous medium	+ Heterogeneous medium
Mean organ dose	3D dose image	3D dose image

Table 2.1: Overview of absorbed dose estimation methods.

Organ S value approach

The organ based dosimetry approach from MIRD [43] was already introduced in 1975. It makes use of organ-specific S values, which are calculated for standardized, digital human phantoms and tabulated for various radionuclides. The S value describes the absorbed dose per targeted organ per unit of time-integrated activity. The concept is explained by figure 2.13 (p. 19): a source organ being homogeneously filled with activity leads to self irradiation and to cross irradiation of a target organ. The absorbed dose per target organ is composed by the irradiation of multiple source organs, including possible self irradiation. Consequently, the average absorbed dose in an organ is calculated with formula $D_t = \sum_{s=1}^N \tilde{A} \cdot S_{s \rightarrow t}$ including all possible combinations of source and target organs. The advantage of this method lies in the availability of pre-calculated source-target combinations of $S_{s \rightarrow t}$ for multiple radionuclides, e.g. provided by Andersson et al. [45]. The subsequent calculation of absorbed dose after the above given formula is naturally simple and fast.

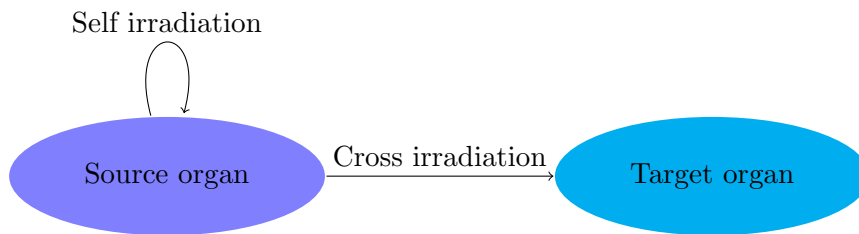


Figure 2.13: MIRD organ S value scheme: a source organ with homogeneous activity distribution yields a self irradiation of the source organ and a cross irradiation of other target organs.

However, this dosimetry approach is limited in its application for patient anatomies which differ significantly from those from the reference phantom. A more realistic patient organ S value can be obtained by multiplication of the organ S value with the phantom organ mass divided by the actual patient organ mass [46], compare with equation 2.1 (p. 19). However, this cannot account for differences in organ shape between the phantom and the patient.

$$S_{s \rightarrow t}^{patient} = S_{s \rightarrow t}^{phantom} \cdot \frac{m_t^{phantom}}{m_t^{patient}}. \quad (2.1)$$

The location, size and shape of tumors are highly patient- and disease-individual. Thus, this dosimetry approach uses the reasonable simplification of a spherical model for tumors. Multiple different sphere sizes of unit density are simulated to obtain tumor S values. Clearly, this approach can solely address the tumor self-dose component and cannot account for cross irradiation from other source organs or tumors. Similar adjustments as in equation 2.1 (p. 19) can be made for the actual tumor mass.

Voxel S value approach

The use of VSVs for absorbed dose estimation was first proposed by MIRDO in 1999 [44]. VSVs are radionuclide- and tissue-specific and can be applied to 3D time-integrated activity images. The great advantage is consequently the possibility to account for heterogeneous activity distributions. VSVs are obtained from MC simulations and represent the fraction of absorbed radiation dose per voxel around a source voxel. For this purpose, a source of the radionuclide of interest is placed in the central voxel of a sufficiently large matrix of a certain tissue type and composition. All interactions and hence energy depositions are scored on a voxel level, compare with the simplified 2D example in figure 2.14 (p. 20).

Although this approach is on a macroscopic voxel level scale, it mimics the uniform irradiation of tissue around a source of a radionuclide in this specific tissue. The convolution of VSVs with the voxelized 3D time-integrated activity image gives a 3D absorbed dose image per patient. The limitation of this approach is the application to heterogeneous tissue types. While for the abdominal region, the assumption of soft tissue is adequate, the application to skeletal regions has to be questioned. The appropriate VSVs must therefore be chosen according to the voxel size, source and target region tissue and radionuclide.

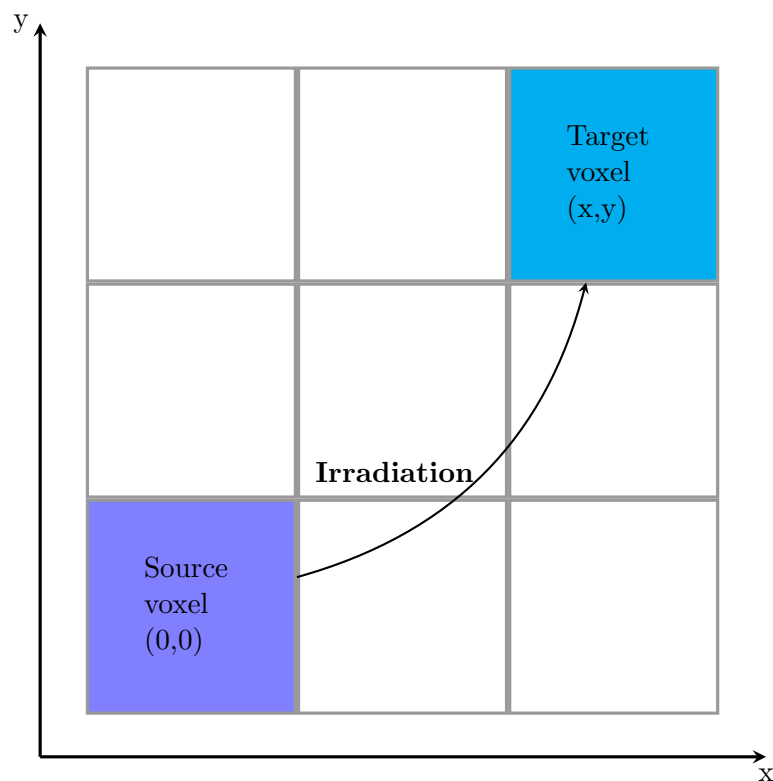


Figure 2.14: Simplified representation of the concept of VSVs: a central source voxel irradiates a target voxel. The central source voxel of course irradiates itself and all surrounding voxels.

MC absorbed dose simulation

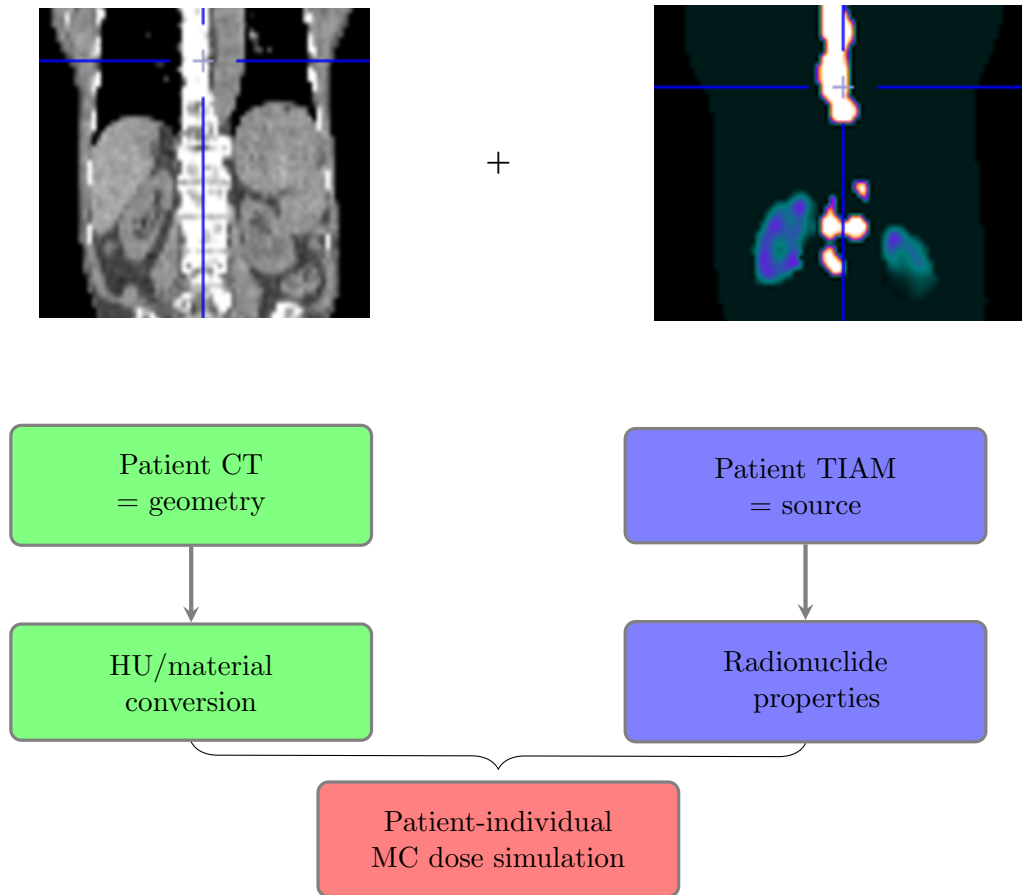


Figure 2.15: Simplified representation of a MC absorbed dose simulation set-up. TIAM: time-integrated activity map.

Patient-individual 3D dosimetry with respect to the patient's anatomy and radionuclide biodistribution is obtained from MC simulation [47]. The particle interaction probabilities, interaction types and the mean free path length before interaction are tissue dependent. By incorporating patient-specific activity and anatomy during particle sampling with MC simulations, it is possible to account for situations with heterogeneous activity distributions and heterogeneous tissue types. MC simulation reproduces the decay of the radionuclide and precisely models all physical processes such as particle transport, interactions and associated energy depositions. The particles are tracked until the remaining energy of the particle is too low to require further consideration in estimation of local energy deposition. The absorbed dose per voxel is consequently estimated by dividing the deposited energy per voxel by the voxel mass. MC absorbed dose simulations takes into account the highest level of physical processes and can therefore be considered as a reference method when evaluating simplified absorbed dose estimation methods. The drawback of patient-individual MC absorbed dose simulations are clearly their complexity and long computation times hindering the implementation into clinical routine.

The required input for MC simulation is a description of the aligned source and geometry. The specification includes the radionuclide, its decay spectrum and spatial distribution. The geometry definition includes a description of density and elemental composition. Both, analytical and voxelized input is possible. Patient-individual absorbed dose simulating is usually based on the 3D time-integrated activity image containing the total number of decays in a voxel grid and the patient CT image revealing the geometry, compare with figure 2.15 (p. 21). The CT image needs to be converted into density and material composition per voxel. This was first in-depth achieved by Schneider et al. giving the conversion of Hounsfield units (HU) to materials and density [48].

The total number of decays according to the source input is simulated for the specified radionuclide in the defined geometry input using random number generators coupled with probability density functions containing the physics information such as the radionuclide decay spectrum, particle interaction cross sections, particle ranges, attenuation and absorption.

GATE MC code

This work used the open source GATE code for MC simulations which is a dedicated tool for nuclear medicine imaging [49] and therapy application [50].

The GATE toolkit is based on the GEANT4 MC simulation structures but can be easily operated using macro language commands.

In general, a GATE absorbed dose simulation requires a certain structure. A material database contains all atomic data and some pre-defined materials with density and composition information. Additional materials or tissue types can be added by the user. The simulation geometry setup can either be defined mathematically or directly incorporate voxelized input like for example CT images. A HU to material and density conversion table can be loaded. Physic processes can be specified by using physics lists and are easily controlled by macro commands. The source can be defined similar to the geometry input by directly loading a voxelized input and specifying the radioisotope from an ion source list containing all decay properties for common nuclear medicine radioisotopes. The simulation output can be determined with so-called actors for example in a voxelized output and many possible scoring options exist, e.g. the deposited energy, the absorbed dose, the number of hits, and the related uncertainties per voxel. [33]

Chapter 3

Studies

3.1 Motivation of this work

This work on absorbed dose estimation focusses on two common nuclear medicine therapies. Although the therapy principle as such is different for ^{90}Y SIRT and ^{177}Lu -PSMA therapy, the general dosimetry concept, given in the flowchart 2.7 (p. 12), applies for both. Either therapies have their individual strengths, limitations and challenges for dosimetry.

The difference between SIRT and radioligand therapy is not restricted to the different therapy indication, but further addresses the way of therapy administration which has a direct impact on the dosimetry workflow.

While the challenge for ^{90}Y SIRT lies more in quantitative activity imaging (compare with step 1) of figure 2.7, p. 12), the crucial part of dosimetry for ^{177}Lu -PSMA is the choice of dosimetry method for application in regions with heterogeneous tissues, especially for bone metastases (compare with step 4) of figure 2.7, p. 12).

However, dosimetry is of importance for understanding patient-individual therapy response and assessment of treatment optimization towards personalized therapy. This work has particularly addressed absorbed dose estimation methods for bone metastases, since mCRPC patients typically present with a large bone metastases load. The heterogeneous density and medium of bone lesions in combination with heterogeneous activity distribution further complicates the absorbed dose estimation. In contrast, for liver tumors receiving SIRT, the medium can be assumed to be homogeneous with possible heterogeneous activity distribution.

The aim of this work is to investigate dosimetry estimation of ^{90}Y SIRT and ^{177}Lu -PSMA therapy. The facilitation of dosimetry within the clinical workflow offers the potential to retrieve the analysis of absorbed dose and response relationships and to move the field to personalized medicine.

3.2 Yttrium-90 SIRT

^{90}Y SIRT combines the therapeutic effects of embolization and radiation damage from β^- decay of ^{90}Y . By the intra-arterial administration, it is possible to place the ^{90}Y microspheres directly into the liver tumor, compare with section 2.3.1. Pre- and post-therapeutic absorbed dose estimation is required to assure optimal tumor treatment with minimized absorbed dose to the healthy liver to obviate affecting the liver function. This could imply an increase or decrease of the ^{90}Y therapy activity for the second SIRT or demonstrate the importance of therapy repetition to reach optimal tumor treatment.

3.2.1 Challenges in SIRT dosimetry

The ^{90}Y microspheres cause an embolization in the blood supply vessels of the tumor. Due to this unique way of therapy administration, the ^{90}Y microspheres are not subject to biological excretion or washout and remain stationary in the liver. This has a direct influence on step 1) of the required steps for dosimetry (see flowchart 2.7, p. 12). With no biological half-life, the effective half-life is equal to the physical half-life. Post-therapeutic imaging at one time point is consequently sufficient and the number of data points in figure 2.9(a) (p. 14) are reduced to a single time point.

The decay spectrum of ^{90}Y needs to be considered before the detailed description of ^{90}Y imaging. The unstable isotope Yttrium-90 ($^{90}_{39}\text{Y}$) decays via β^- decay and a half-life of 64.053 h [51] to the ground state of Zirconium-90 ($^{90}_{40}\text{Zr}$). As a β^- emitter with a maximum β^- energy of 2.3 MeV [13] and a maximum β^- range in soft tissue of 11.3 mm, ^{90}Y is favourable for the therapy of extended soft tissue lesions and is therefore suitable for SIRT of pronounced liver lesions. ^{90}Y has no discrete photo-peak, but as a β^- emitter it presents with a continuous bremsstrahlung spectrum which could be used for SPECT imaging. In addition, ^{90}Y has a small probability of internal pair production, when it decays to the 0^+ first excited state of ^{90}Zr [52] [53] with a branching ratio of $(31.86 \pm 0.47) \cdot 10^{-6}$ [54]. The annihilation radiation of the positron from internal pair production can be exploited in PET imaging. The ^{90}Y photon spectrum with bremsstrahlung spectrum and annihilation peak is shown in figure 3.1 (p. 24).

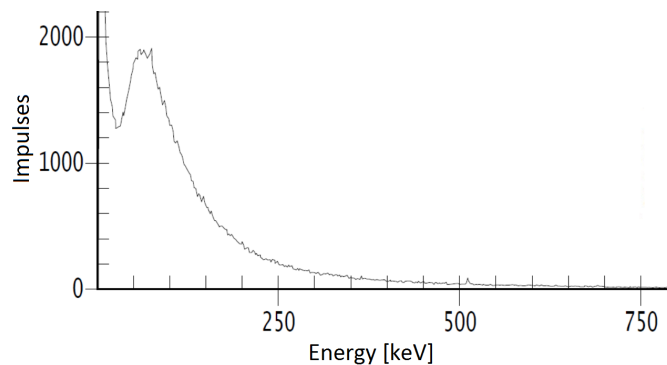
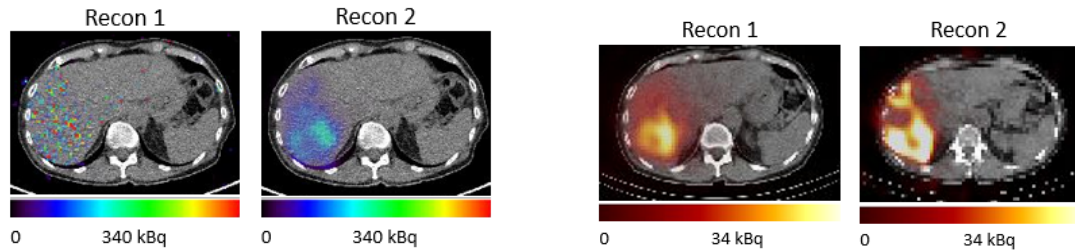


Figure 3.1: Photon spectrum of a ^{90}Y sample in a germanium detector.

SPECT imaging of bremsstrahlung is challenging due to the fact that SPECT imaging as such was designed to detect "single photons" of a specific photo-peak, which is assumed during acquisition and reconstruction. This limits the quantification capabilities of ^{90}Y BRS SPECT imaging for the use of post-SIRT absorbed dose estimation. On the other hand, post-therapeutic ^{90}Y PET imaging suffers from the small signal of 511 keV photons of the decay of ^{90}Y , compare with the small peak in the spectrum (figure 3.1, p. 24).

It becomes even more comprehensible that quantitative ^{90}Y imaging is the challenging part, when regarding at figure 3.2 (p. 25), which is showing an exemplary ^{90}Y SIRT patient who underwent post-therapeutic ^{90}Y BRS SPECT/CT and ^{90}Y PET/CT imaging. The differences between imaging modalities and the impact of appropriate reconstruction parameters for both, SPECT and PET, is nicely illustrated.



(a) ^{90}Y PET/CT images, reconstructed with different reconstruction parameters.

(b) ^{90}Y BRS SPECT/CT images, reconstructed with different reconstruction parameters.

Figure 3.2: ^{90}Y SIRT activity images from different imaging modalities and with different reconstruction parameter choice.

Since the quantitative activity measurement is the crucial part hindering routine absorbed dose estimation for ^{90}Y SIRT, the first investigation of this work was a phantom imaging study on ^{90}Y to improve the quality and quantitative accuracy of ^{90}Y imaging.

The subsequent steps 2) to 4) of flowchart 2.7 (p. 12) for ^{90}Y SIRT dosimetry are less challenging than step 1), but still require various processing efforts. Step 2) is commonly performed by manual delineation of tumor and liver VOIs on the pre-therapeutic MR image. To allow for further evaluation of activity images, the MR image needs to be co-registered to the post-therapeutic SPECT/CT or PET/CT in order to copy the VOIs. For this purpose, typically a rigid co-registration of the CT and MR is performed and the translation is subsequently applied to the activity image.

The fitting of step 3) can be obtained assuming only physical decay and using the decay constant λ_{phys} of ^{90}Y . This further facilitates the time-integrated activity determination to formula 3.1 (p. 26). By using the activity $A(t)$ per voxel from SPECT or PET imaging and the imaging time point t , this can be calculated per voxel.

$$\tilde{A} = \int_0^{\infty} A(t)dt = \int_0^{\infty} A_0 \cdot e^{-\lambda_{phys} \cdot t} dt = \frac{A_0}{\lambda_{phys}} = \frac{A(t) \cdot e^{\lambda_{phys} \cdot t}}{\lambda_{phys}}. \quad (3.1)$$

The conversion to absorbed dose within step 4) does not necessarily require a full patient-individual MC absorbed dose simulation. Although the maximum range of the β^- of ^{90}Y in soft tissue is 11.3 mm, it is assumed that the volume of interest consists fully of soft tissue (=liver). However, due to the nature of therapy administration of SIRT, a heterogeneous activity distribution of ^{90}Y is very likely. Hence, the method of choice with respect to table 2.1 (p. 18) is the voxel S value approach.

To summarize, the following figure 3.3 (p. 26) shows the general dosimetry workflow, modified for ^{90}Y SIRT.

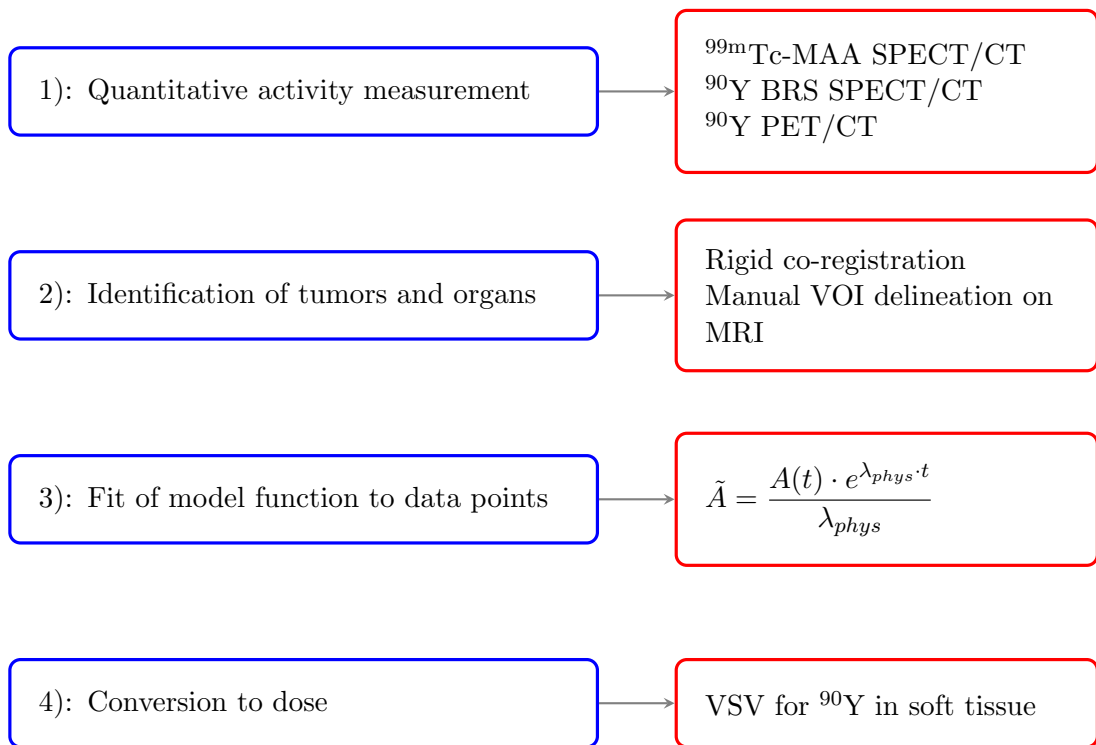


Figure 3.3: Required processing steps within the general dosimetry workflow, modified for ^{90}Y SIRT.

3.2.2 Preliminary phantom studies for quantitative imaging within the therapy workflow of ^{90}Y SIRT

Background

The quantitative measurement of the ^{90}Y microsphere distribution in the patient is necessary for all subsequent absorbed dose estimations. As introduced above, the ^{90}Y imaging is the crucial part within the ^{90}Y SIRT dosimetry workflow (flowchart 3.3, p. 26). Consequently, this work started with phantom measurements to quantify the image quality and accuracy. Different reconstruction parameters were investigated to improve both. For this purpose, the NEMA IEC Body Phantom SetTM was used. This phantom represents the human abdomen with its large roughly cylindrical shape and further has six fillable sphere inserts, see photo 3.4 (p. 27). The general phantom parameters are given in table 3.1 (p. 27). Measurements were performed for ^{90}Y BRS SPECT and ^{90}Y PET.

Methods

For all phantom experiments, it is crucial to reproduce the clinical setting of patient imaging in view of activity concentrations and total activity. Typical patient activity concentrations within the liver were determined for ^{90}Y microspheres. Different ratios of activity concentrations in the spheres and the phantom background were measured. So called sphere-to-background ratios of 8:1, 6:1, 4:1, and 3:1 were measured to mimic different tumor to healthy liver activity uptake ratios.



Figure 3.4: NEMA IEC Body Phantom SetTM.

Phantom	Volume [ml]
ø37 mm sphere	26.52
ø28 mm sphere	11.49
ø22 mm sphere	5.58
ø17 mm sphere	2.57
ø13 mm sphere	1.15
ø10 mm sphere	0.52
Phantom background (BG)	~ 9700

Table 3.1: NEMA IEC Body Phantom SetTM parameters.

Phantom preparation

The phantom background for the ^{90}Y measurements was filled with one-tenth of the average patient activity concentration in the whole liver. This decision was made for two reasons: Firstly, the volume of the phantom background is much larger than typical patient liver volumes. This would artificially increase the total phantom activity far beyond the maximum ^{90}Y SIRT activities. With higher activities being present in the SPECT or PET field of view (FOV), the detected noise would be raised and not mim-

icking the patient situation. A second reason for this decision was the personal radiation protection during phantom preparation and handling.

The corresponding sphere activity was set according to the aimed sphere-to-background ratio in relation to the phantom background activity concentration. The smaller ratios were subsequently reached by adding activity to the phantom background. However, the imaging time points were planned to measure with a constant phantom background activity concentration for all ratios by taking advantage of the radioactive decay. Thus, the ^{90}Y background activity concentration was 0.2 MBq/ml. All activity concentrations in spheres and background were verified with a gamma counter from PACKARD.

Phantom imaging

The image acquisition parameter for all SPECT based phantom measurements were set to the same settings as exploited in the clinical routine for ^{90}Y SPECT/CT acquisition. These parameters are listed in table 3.2 (p. 28). This would enable a possible application of improved reconstruction parameter settings to the existing patient data if raw data is available. The only difference between the patient imaging parameters for ^{90}Y SPECT/CT was the time per step of 400 s which is ten-times the patient step time. This adjustment was made to obtain similar count statistics per voxel for the patient case and for the ^{90}Y phantom, where the activity concentration in the phantom background was one-tenth of the patient activity concentration. All SPECT measurements were performed on a Siemens Symbia T2 SPECT/CT.

Energy windows	Collimator	Matrix	# Angular steps	Time/step
primary: 108 keV ($\pm 20\%$), back-ground: 360 keV ($\pm 15\%$)	MELP	128x128	32	400 s

Table 3.2: ^{90}Y BRS SPECT acquisition parameter; medium-energy-low-penetration (MELP).

The PET measurements were performed with time-of-flight (TOF) on a Siemens Biograph mCT flow PET/CT. The acquisition was made in one bed position with 300 min scan time per bed, which should mimic a tolerable patient scan time times ten, to reach similar count statistics per voxel for patient and phantom measurements.

Additional phantom scans in flow mode for ^{90}Y PET/CT and with 40 s time per step for ^{90}Y BRS SPECT/CT were acquired for future evaluations in combination with patient scans.

Image reconstruction

Different sets of reconstruction parameters of an in-house maximum a posteriori (MAP) reconstruction for SPECT [55] and of the Siemens TrueX TOF reconstruction algorithm

for PET were used. SPECT images were reconstructed in 128x128 matrix sizes with $(4.7952\text{ mm})^3$ voxel size. For PET images, different matrix and voxel sizes were tested. The reconstruction for ^{90}Y BRS SPECT used CT-based attenuation correction with a background compensation method as described by Siman et al. [56]. The conventional scatter correction during MAP reconstruction is replaced by the background compensation. The projection data from the background energy window was added up to the primary energy window with a weighting to adjust for the different widths of the energy windows.

Different numbers of iterations, subsets and full-width-half-maximum (FWHM) of post-reconstruction Gauss filters were tested for the TrueX TOF reconstruction of PET.

The PET images are already given in values of activity concentrations (e.g. kBq/ml) by using the branching ratio information of the radionuclide and a cross-calibration with ^{18}F , which is routinely performed for quality control. The SPECT images, on the other hand, need to be converted into values of activity concentrations. ^{90}Y BRS SPECT imaging is limited by the assumption of a photo-peak during image acquisition and reconstruction of the bremsstrahlung spectrum. Therefore, the ^{90}Y BRS SPECT calibration factor can exhibit an object dependency and a self-calibration approach was used herein [57]. This individual calibration factor is determined by dividing the total activity, which is either the applied therapy activity of ^{90}Y or the known total phantom ^{90}Y activity, by the total counts in the SPECT image. Obviously, the total activity needs to be decay corrected to the imaging time point.

Image evaluation

Recovery coefficients (RC) and signal-to-noise-ratio (SNR) were used to evaluate differences in quantification and image quality between the different imaging modalities, PET acquisition modes and all tested reconstruction parameters. The RC is defined as the ratio of the measured image activity concentration in a VOI divided by the known activity concentration in the belonging phantom region. The SNR is calculated by the difference of the VOI mean values of the spheres and a VOI mean value in the phantom background which is divided by the standard deviation of the phantom background VOI [58].

$$\boxed{\text{RC} = \frac{(A/V)_{\text{image}}}{(A/V)_{\text{phantom}}}}, \quad \text{and} \quad \boxed{\text{SNR} = \frac{\text{VOI}_{\text{insert}} - \text{VOI}_{\text{background}}}{\sigma_{\text{background}}}}. \quad (3.2)$$

Results

Amongst the herein investigated reconstruction parameter sets, the following were identified as being suitable for application within the SIRT post-therapeutic imaging workflow:

- ^{90}Y BRS SPECT: 15 iterations, 16 subsets, 0.01 penalty.
- ^{90}Y PET: 128x128 matrix, 2 iterations, 21 subsets, 10 mm FWHM Gauss filter.

The impact of smaller sphere-to-background ratios is visualized for ^{90}Y BRS SPECT in figure 3.5 (p. 30) and for ^{90}Y PET in figure 3.6 (p. 30). With decreasing ratio, the number of visible spheres and overall image quality decreases. In dependence on the tumor entity being treated with ^{90}Y SIRT, the ratio of tumor to healthy liver uptake varies. However, the above identified reconstruction parameter were suitable for all investigated phantom sphere-to-background ratios.

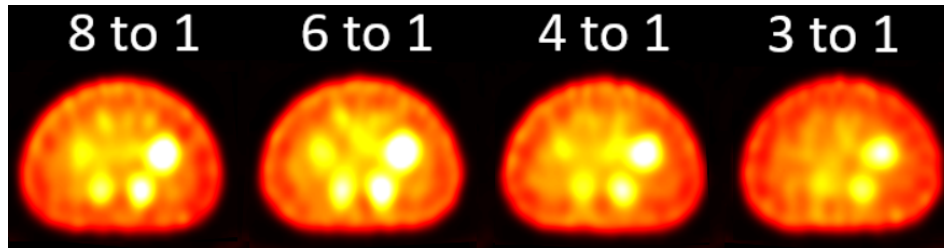


Figure 3.5: Transversal slices of the ^{90}Y BRS SPECT phantom image for different sphere-to-background ratios.

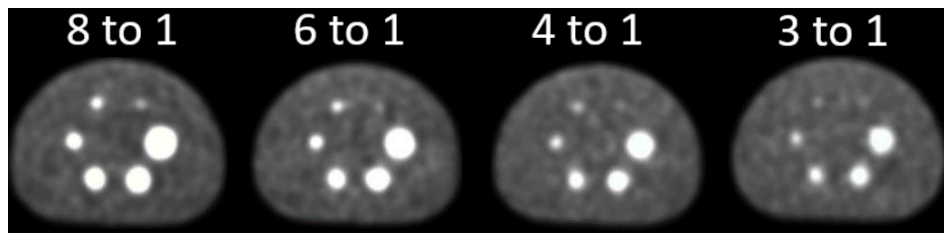


Figure 3.6: Transversal slices of the ^{90}Y PET phantom image for different sphere-to-background ratios.

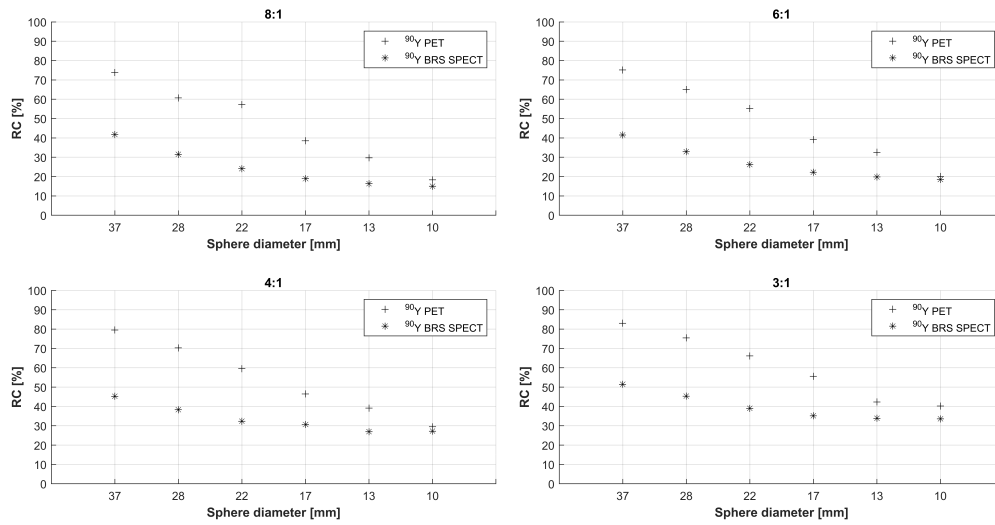
The results of the evaluation of RCs and SNRs for ^{90}Y PET and ^{90}Y BRS SPECT are given in figures 3.7(a) and 3.7(b) (p. 31) for the previously identified reconstruction parameters. The related RCs of the phantom background are given in table 3.3 (p. 30).

RC BG [%]	8:1	6:1	4:1	3:1
^{90}Y PET	89	92	92	97
^{90}Y BRS SPECT	110	100	99	99

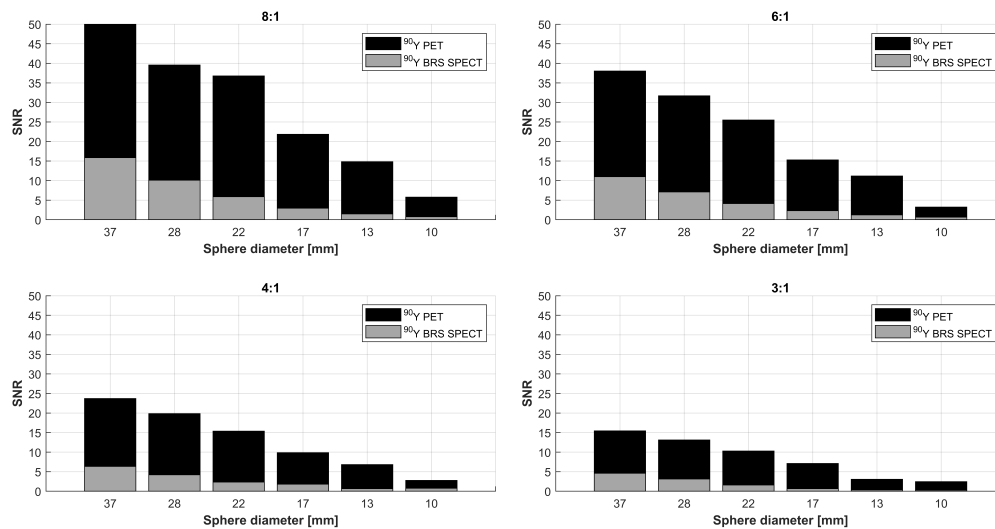
Table 3.3: RCs of the phantom background for ^{90}Y PET and ^{90}Y BRS SPECT and all sphere-to-background ratios.

^{90}Y PET imaging of ^{90}Y SIRT patients will be performed using flow mode. This acquisition allows for a trade-off between required scan length to cover the entire liver and overall scan time to assure a scan duration with limited patient movements due to

discomfort, while acquiring enough true coincidences.



(a) RCs of ^{90}Y PET and ^{90}Y BRS SPECT for the above listed reconstruction parameters.



(b) SNRs of ^{90}Y PET and ^{90}Y BRS SPECT for the above listed reconstruction parameters.

Figure 3.7: Results of ^{90}Y PET and ^{90}Y phantom measurements with different sphere-to-background ratios.

3.2.3 Investigation of the impact of the underlying activity imaging method on absorbed dose estimates for ^{90}Y SIRT of hepatocellular carcinoma

The following paragraphs cover the work of the first original publication of this thesis. The overall content is summarized by figure 3.8 (p. 32).

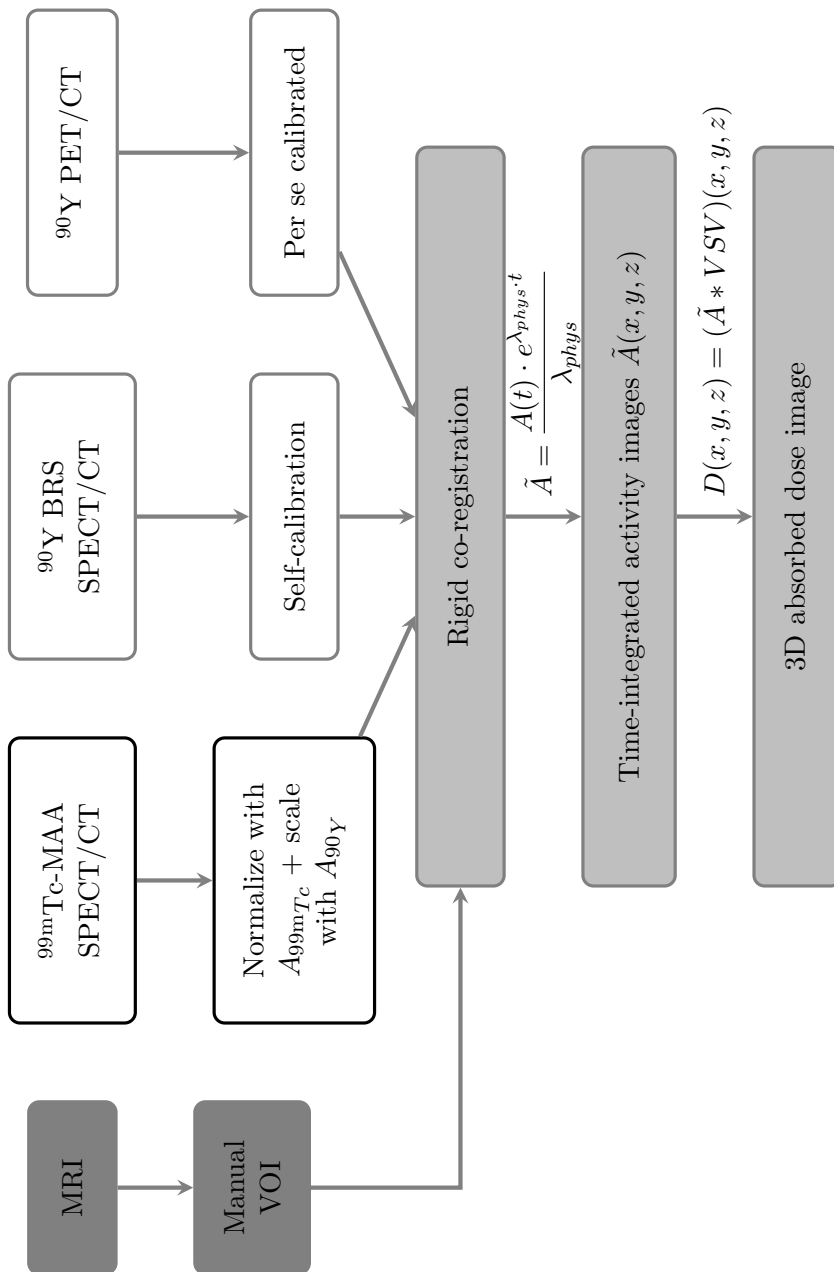


Figure 3.8: Required processing steps within the general dosimetry workflow, modified for ^{90}Y SIRT.

Background

The preliminary phantom study (described in section 3.2.2) demonstrated the improved quantification capabilities of ^{90}Y PET imaging compared to ^{90}Y BRS SPECT imaging. However, ^{90}Y PET post-therapy imaging is not yet routinely implemented into the clinical ^{90}Y SIRT workflow. Furthermore, there is a large amount of existing ^{90}Y SIRT patient data in our institution, which were acquired before ^{90}Y PET imaging was first introduced. Over 1900 ^{90}Y SIRTs were performed in our institution between 2003 and today. A broad retrospective analysis of these existing data in view of tumor and healthy liver absorbed dose estimates correlated e.g. with overall survival could potentially improve the future ^{90}Y SIRT planning and response.

The goal of this work was consequently to investigate possible ^{90}Y SIRT dosimetry approaches for the application in both scenarios, with and without ^{90}Y PET image. Three different processing approaches for ^{90}Y SIRT were chosen. The difference between the approaches is the activity image upon the dosimetry estimation is based. Three different activity images are available within the therapy workflow of SIRT: the pre-therapeutic $^{99\text{m}}\text{Tc}$ -MAA SPECT versus the post-therapeutic ^{90}Y PET or ^{90}Y BRS SPECT.

Methods

At first, the preliminary phantom study, acquired with the patient image acquisition parameters, was compared to a $^{99\text{m}}\text{Tc}$ SPECT/CT phantom study at a sphere-to-background ratio of 8:1.

While the post-therapeutic ^{90}Y PET and ^{90}Y BRS SPECT can be used directly for absorbed dose estimation, the $^{99\text{m}}\text{Tc}$ -MAA SPECT requires additional processing to allow to be used for post-therapeutic dosimetry. In addition, the latter approach is only reasonable under the condition that the pre-therapeutic $^{99\text{m}}\text{Tc}$ -MAA and therapeutic ^{90}Y microsphere distributions agree. Figure 3.8 (p. 32) provides an overview of the three dosimetry approaches.

The comparison of the approaches was performed retrospectively on existing anonymized patient data. Inclusion criteria were available post-therapeutic ^{90}Y PET and ^{90}Y BRS SPECT image data limiting the number of patients and/or available ^{90}Y SIRTs for the evaluation. This evaluation setup was approved by the local ethics committee of LMU Munich (19-134 KB).

An initial investigation for a single tumor entity was performed. The first publication within this cumulative dissertation was focussed on patients suffering from hepatocellular carcinoma. ^{90}Y SIRT is a possible and established treatment form for this tumor entity in accordance with the German S3 guideline for the therapy of HCC [59].

A small collective of nine patients suffering from HCC and in total ten ^{90}Y SIRTs could be analysed in view of absorbed dose of tumor and healthy liver parenchyma in dependence on the underlying activity image for absorbed dose estimation. All existing image data was reconstructed using the above identified best possible reconstruction parameter for the three different imaging modalities. The reference absorbed dose estimate was obtained from ^{90}Y PET/CT due to its better activity quantification. Although the hybrid dosimetry approach using the scaled $^{99\text{m}}\text{Tc}/^{90}\text{Y}$ activity image is limited by the

mandatory comparability of ^{99m}Tc -MAA and ^{90}Y microsphere pattern, the investigation is justified by the similar quantification capabilities of ^{99m}Tc SPECT/CT and ^{90}Y PET, see figure 3.9 (p. 35).

Before any further processing, all images were co-registered to each other. The co-registration of the pre-therapeutic MR, ^{99m}Tc -MAA SPECT/CT, ^{90}Y PET/CT and ^{90}Y SPECT/CT was performed rigidly and the CT image from ^{99m}Tc -MAA SPECT/CT was used as a reference image. This decision was made since the first in-house medical image within the SIRT therapy workflow is the ^{99m}Tc -MAA SPECT/CT because the MR images can possibly come from external institutions and potentially have varying voxel sizes and acquisition parameters. The pre-therapeutic MR image was used for manual delineation of tumor and liver VOIs using PMOD (v4.003; PMOD Technologies LLC). The first dosimetry approach used the pre-therapeutic ^{99m}Tc -MAA SPECT/CT data as a surrogate for the quantitative image of the ^{90}Y activity distribution. The SPECT data was normalized with the total ^{99m}Tc activity in the image. Because of delivering ^{90}Y SIRT as a lobar or segmental treatment, it became necessary to adjust or "crop" the ^{99m}Tc -MAA SPECT activity image to the actual treated therapy volume from ^{90}Y SIRT. A treated volume VOI was obtained from the ^{90}Y BRS SPECT image by applying a 10% iso-contour. The normalized ^{99m}Tc -MAA SPECT was then scaled inside the treated volume VOI with the administered ^{90}Y SIRT activity. This created scaled $^{99m}\text{Tc}/^{90}\text{Y}$ SPECT/CT image enabled the use for post-therapeutic dosimetry. It consequently used the distribution information from ^{99m}Tc -MAA in combination with the actual ^{90}Y therapy activity. The two other dosimetry approaches were directly based on ^{90}Y activity image data.

The time-integrated activity image was created with formula 3.1 (p. 26) using the physical half-life λ_{phys} and the time t between therapy activity administration and image acquisition. The voxel S values for ^{90}Y originate from previous MC simulations of our group [60] using FLUKA and the definition of soft tissue from the International Commission on Radiological Protection (ICRP). A 3D absorbed map per patient was derived by convolution of the time-integrated activity images with the ^{90}Y VSVs.

Results

The related RCs and the SNRs of the four largest phantom spheres are given in figure 3.9 (p. 35). The RCs of ^{90}Y PET and ^{99m}T SPECT are comparable, while those of ^{90}Y BRS SPECT are significantly smaller. On the other hand, the SNR of ^{99m}T SPECT outperforms those of ^{90}Y PET and ^{90}Y BRS SPECT. Regarding the phantom background, all three imaging modalities revealed comparable RCs with 101 %, 95 % and 96 % for ^{90}Y BRS SPECT, ^{99m}T SPECT, and ^{90}Y PET.

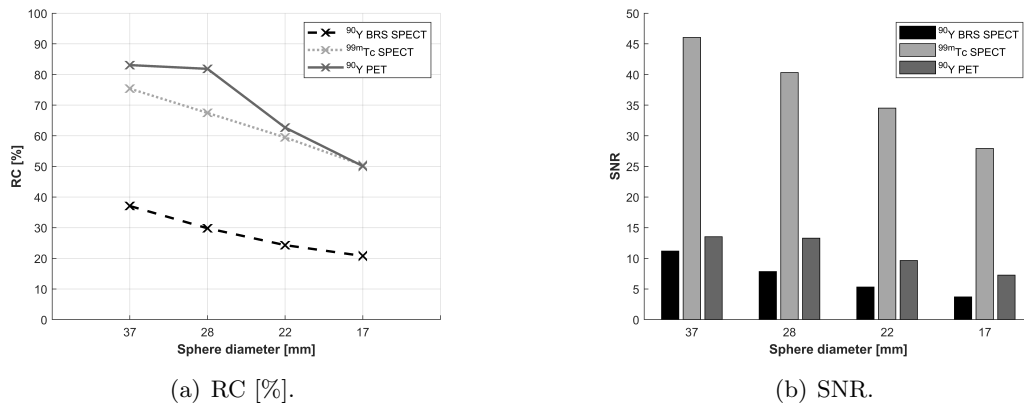


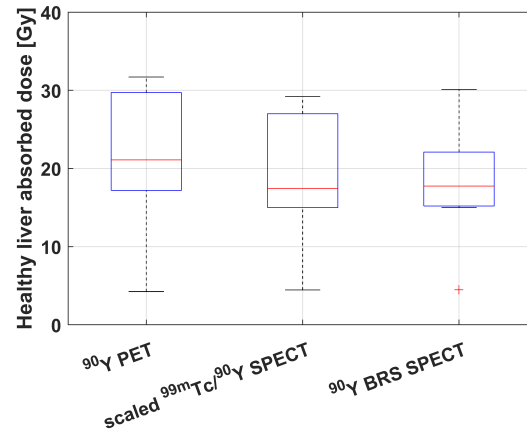
Figure 3.9: RC and SNR of the four largest spheres of the NEMA IEC Body Phantom SetTM obtained from measurements with the identified patient acquisition and reconstruction parameters for ^{90}Y BRS SPECT, $^{99\text{m}}\text{Tc}$ SPECT, and ^{90}Y PET.

The percentage differences (PD) of healthy liver and tumor absorbed dose estimates from scaled $^{99\text{m}}\text{Tc}/^{90}\text{Y}$ SPECT/CT and ^{90}Y BRS SPECT compared to the reference absorbed dose estimate from ^{90}Y PET, averaged over all ten investigated SIRTs, are summarized in table 3.4 (p. 35).

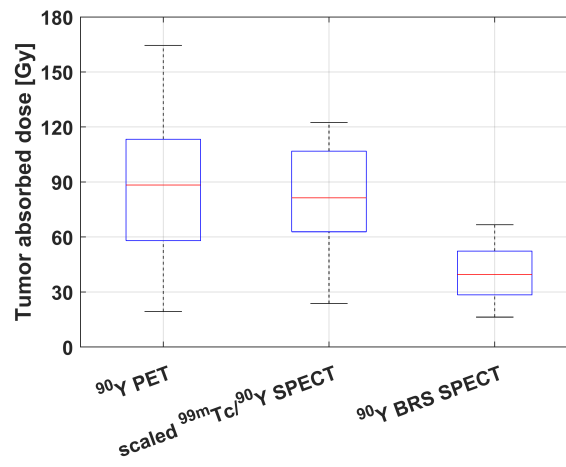
	Healthy liver		Tumor	
	scaled $^{99\text{m}}\text{Tc}/^{90}\text{Y}$ SPECT/CT	^{90}Y BRS SPECT	scaled $^{99\text{m}}\text{Tc}/^{90}\text{Y}$ SPECT/CT	^{90}Y BRS SPECT
Mean PD [%]	- 10 ± 8	-12 ± 10	-2 ± 18	-50 ± 13
Min PD [%]	- 21	- 31	- 37	- 66
Max PD [%]	+ 5	+ 6	+ 23	- 16

Table 3.4: PD of healthy liver and tumor absorbed dose estimates from scaled $^{99\text{m}}\text{Tc}/^{90}\text{Y}$ SPECT and ^{90}Y BRS SPECT compared to ^{90}Y PET, averaged over all ten evaluated SIRTs and the minimum and maximum PD per methodology are shown.

The PDs in table 3.4 (p. 35) and the boxplots in figure 3.10(a) (p. 36) showed comparable absorbed dose estimates for all three modalities for the healthy liver. This was in concordance with the comparable RCs of the phantom background for $^{99\text{m}}\text{Tc}$ SPECT, ^{90}Y BRS SPECT and ^{90}Y PET. However, the tumor absorbed dose estimates from ^{90}Y BRS SPECT showed a large underestimation of on average $-50 \pm 13\%$ compared to the reference absorbed dose estimate from ^{90}Y PET. Figure 3.10(b) (p. 36) further illustrated the underestimation of tumor absorbed doses from ^{90}Y BRS SPECT, while the absorbed doses from scaled $^{99\text{m}}\text{Tc}/^{90}\text{Y}$ SPECT were comparable to those from ^{90}Y PET.



(a) Healthy liver absorbed dose.



(b) Tumor absorbed dose.

Figure 3.10: Absorbed dose estimates for healthy liver and tumor for all three investigated imaging modalities.

3.3 Lutetium-177-PSMA therapy

The radioligand therapy with ^{177}Lu -PSMA became a valuable treatment option for patients for whom all first-line therapy alternatives are exhausted. Due to the therapy concept and administration of the radiopharmaceutical via the patient's blood circulation, this is especially of importance for patients with a large metastases spread, as introduced in section 2.3.2. However, at the same time, multiple healthy organs and tissues have to be prevented from overdosage and hence radiation damage. The OARs for internal radionuclide therapy with ^{177}Lu -PSMA are amongst others, the kidneys, bone marrow, salivary glands and lacrimal glands. The most critical and dose limiting organ is the bone marrow. Absorbed dose estimation is hence essential to minimize radiation damage to OARs. On the other hand, it is necessary to determine the absorbed dose to all metastases within the patient to enable combination of dose-response and therapy outcome analyses with the goal of therapy optimization. The absorbed dose estimation for OARs and tumors has therefore the potential to adapt subsequent therapy cycles to improve the therapy response. Dosimetry further allows for a personalized treatment by patient-individual therapy planning.

Various studies addressing the absorbed dose to OARs for ^{177}Lu -PSMA therapy exist, e.g. Gosewisch et al. [61], Baum et al. [10] and Hohberg et al. [62]. However, very few publications estimate absorbed doses of prostate cancer metastases, especially for bone lesions. Consequently, this work focussed on the comparison of different dosimetry approaches for accurate bone lesion dosimetry in ^{177}Lu -PSMA therapy.

3.3.1 Challenges in ^{177}Lu -PSMA therapy dosimetry

The quantitative imaging of ^{177}Lu has been investigated by different groups and was summarized in joint guidelines of the European Association Of Nuclear Medicine (EANM) and MIRD [63]. Quantitative imaging of ^{177}Lu with appropriate attenuation plus scatter correction and calibration was previously studied in our institution by Delker et al. [55] and is routinely incorporated into the ^{177}Lu -PSMA therapy imaging workflow.

The time points for the quantitative SPECT/CT acquisitions were chosen such that no early time point is used which could potentially be influenced by the radioligand uptake phase (compare with the curve in figure 2.9(b), p. 14). The imaging can be acquired during the four day in-house hospital stay of the patient. Consequently, quantitative SPECT imaging is performed 24 h, 48 h and 72 h post injection (p.i.). This represents a simplified sampling scheme for the imaging of radionuclide distribution over time. Clearly, more imaging time-points would be desirable, but a compromise has to be made between sampling and patient comfort or camera availability.

Referring to the segmentation of tumors and organs for step number 2) of flowchart 2.7 (p. 12), the situation for ^{177}Lu -PSMA therapy is more complex than for ^{90}Y SIRT. Quantitative SPECT/CT images from three different time points need to be carefully aligned to each other. The subsequent segmentation would require too much effort to be performed manually for VOI definition of tumors and organs. Hence, a reproducible semi-automatic segmentation has been previously investigated for ^{177}Lu -PSMA therapy in our group [64]. A robust k-means based cluster segmentation has been identified and is used during VOI definition for the ^{177}Lu -PSMA therapy dosimetry workflow of this

work.

While steps 1) and 2) have previously been examined in our group, the creation of a voxelized 3D time-integrated activity image for step number 3) of flowchart 2.7 (p. 12) for ^{177}Lu -PSMA therapy remains an open question for this work.

However, the most crucial part is the choice of dosimetry method (compare with step number 4) of flowchart 2.7, p. 12). The accurate dosimetry of regions with heterogeneous activity distribution and heterogeneous tissues and densities is challenging and the choice of dosimetry method for absorbed dose estimation is difficult. The variation between densities in the skeleton in general and bone lesions is illustrated by the density map in figure 3.11 (p. 38), which is based on a patient's CT image. The increase in bone lesion density is induced by an enhanced number of osteoblasts [65].

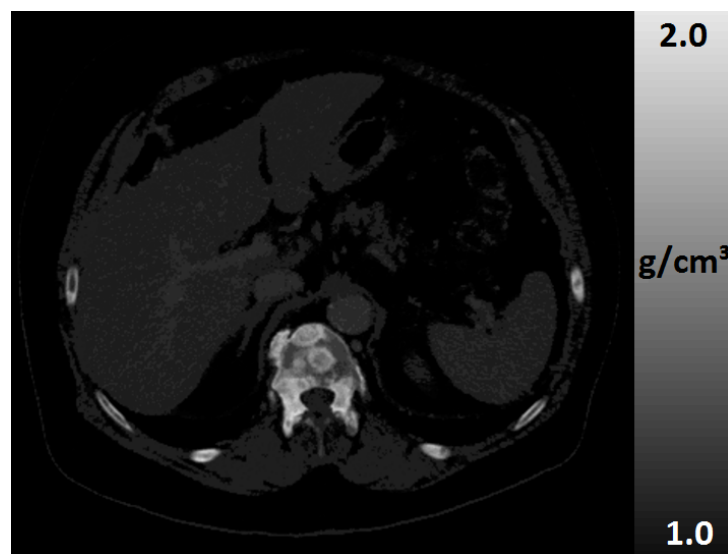


Figure 3.11: Density map of a mCRPC patient showing the increase in density in the metastasis in the vertebrae and very comparable densities in the soft tissue regions of the abdomen.

3.3.2 Preliminary work for 3D time-integrated activity map creation

Background

Besides the image acquisition and processing within steps 1) and 2) of the dosimetry workflow (compare with flowchart 2.7, p. 12), the creation of time-integrated activity maps within step 3) is required for further absorbed dose estimation in step 4). However, the choice of fit function and subsequent time-integration on either an organ or tumor level or on a voxel level is crucial. Image artifacts and quantification errors as well as co-registration discrepancies can influence the voxel-wise fitting and hence time-integration.

In contrast to the ^{90}Y SIRT, where solely physical decay can be assumed, the radioligand therapy with ^{177}Lu -PSMA exhibits a time-dependent biodistribution. Thus, the creation of a voxelized 3D time-integrated activity map was investigated at first.

Methods

Due to the possible influence of image artifacts and noise in individual voxels onto time-activity-integration, it was decided to investigate a hybrid VOI/voxel-wise approach. A mono-exponential pharmacokinetic was assumed in concordance with previous work from our group [66]. Consequently, the time-integrated activity formula is generally reduced to $\tilde{A} = \frac{A_0}{\lambda_{eff}}$. The effective half-life per VOI, $\lambda_{eff,VOI}$, was used with the aim to reduce the impact of image artifacts of individual voxels onto the time-integrated activity map creation. In contrast to that, the A_0 was supposed to be derived at the voxel level using the equation $A_0 = A(t) \cdot e^{\lambda_{eff,VOI} \cdot t}$. This did raise the question which activity image with $A(t)$ per voxel should be used to obtain A_0 - the QSPECT from 24 h, or 48 h, or 72 h p.i..

To address this question, a simple comparison for six of the patients being included in the investigations of section 3.3.3 was conducted. The time-integrated activity per lesion VOI \tilde{A}^{VOI} was calculated using the fit parameter of A_0 and λ_{eff} per VOI obtained from mono-exponential fitting. This served as a reference per lesion VOI. In addition, three 3D voxel-wise time-integrated activity maps were created based on either the 24 h, 48 h, and 72 h QSPECT, respectively, using formula 3.3 (p. 3.3).

$$\tilde{A}^{voxel} = \frac{A_{t=0}^{voxel}}{\lambda_{VOI}} = \left\{ \begin{array}{l} \frac{A_{t=24h}^{voxel} \cdot e^{\lambda_{VOI} \cdot t(t=24h)}}{\lambda_{VOI}} \\ \frac{A_{t=48h}^{voxel} \cdot e^{\lambda_{VOI} \cdot t(t=48h)}}{\lambda_{VOI}} \\ \frac{A_{t=72h}^{voxel} \cdot e^{\lambda_{VOI} \cdot t(t=72h)}}{\lambda_{VOI}} \end{array} \right. . \quad (3.3)$$

In a next step, the lesion VOIs were used to evaluate the generated time-integrated activity maps. The average time-integrated activity value of all lesion voxels was compared against the reference \tilde{A}^{VOI} per lesion VOI from the non-voxelized approach using the fit parameters. The PD per time-point against the reference lesion time-integrated activity

was compared for all lesions of the six patients.

Results

In total 82 bone lesions were evaluated. The results are displayed in figure 3.12 (p. 40).

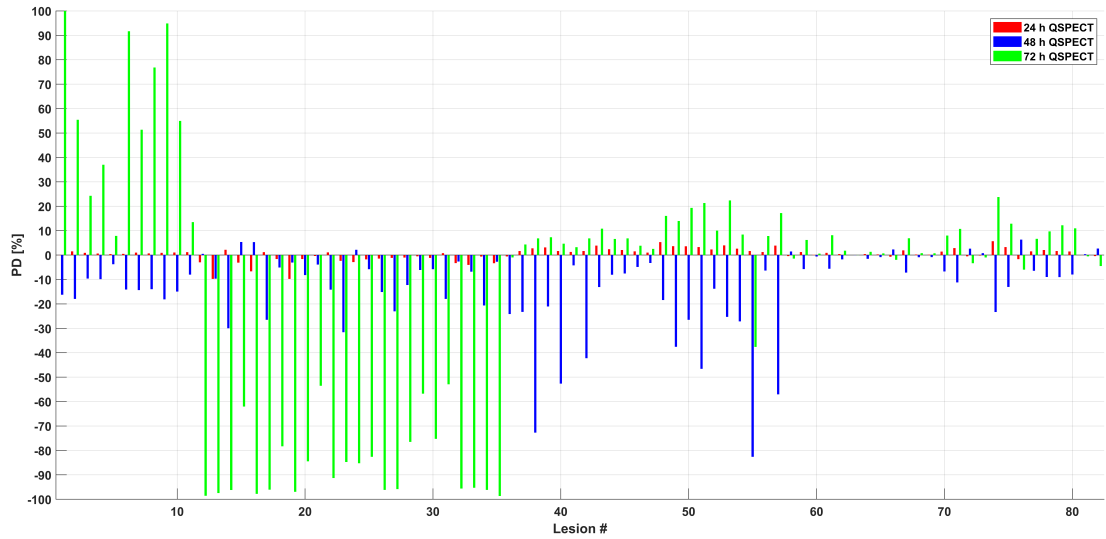


Figure 3.12: Percentage differences in average time-integrated activity per lesion VOI, obtained from QSPECT compared against the reference \tilde{A}^{VOI} .

For all 82 evaluated lesion, the 24 h QSPECT showed the smallest PDs compared against the reference \tilde{A}^{VOI} per lesion VOI. It was hence decided to use the 24 h QSPECT for the creation of a voxel-wise time-integrated activity map.

3.3.3 Impact of dosimetry method on absorbed dose estimate for bone lesions for ¹⁷⁷Lu-PSMA therapy of patients with mCRPC

Figure 3.13 (p. 41) illustrates the key points of the research of the second original publication of this thesis, which is covered within this section.

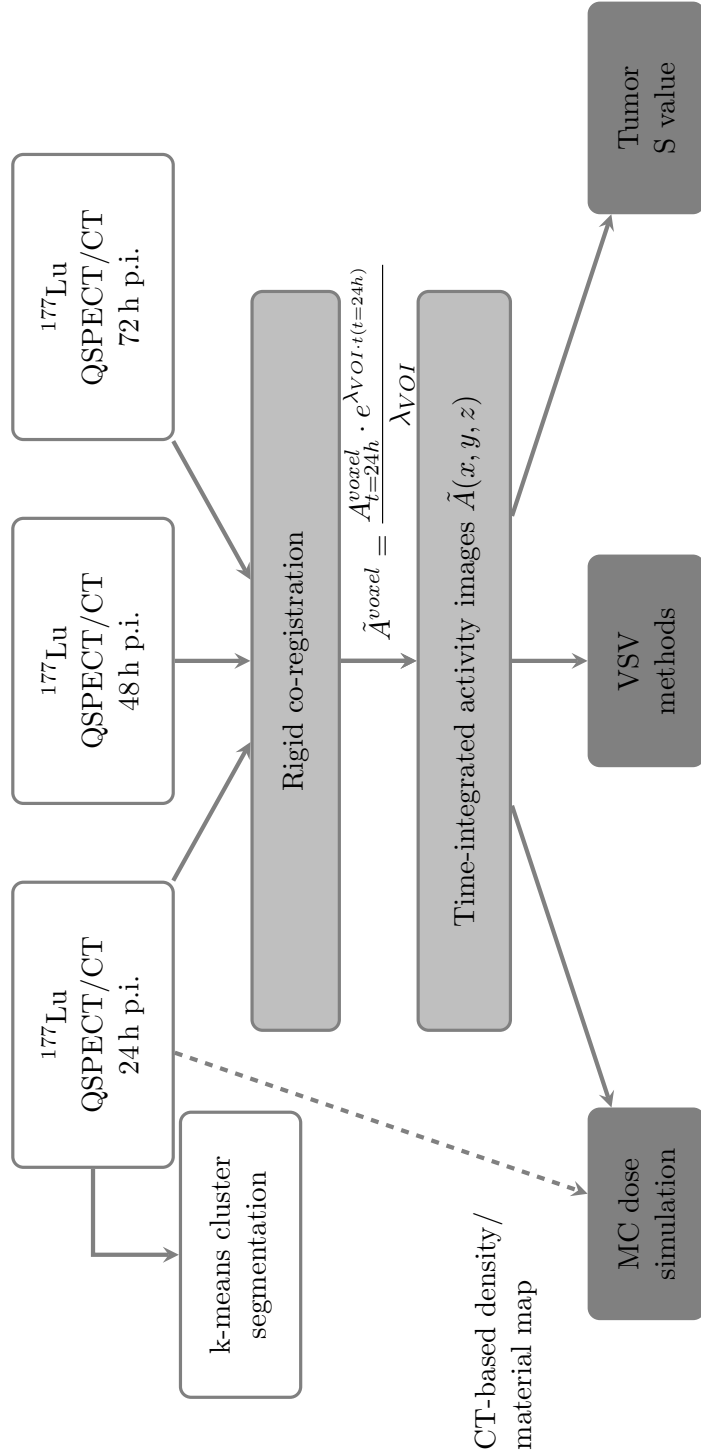


Figure 3.13: Processing steps within the dosimetry workflow of ¹⁷⁷Lu-PSMA therapy.

Background

This investigation aimed at comparing different absorbed dose estimation methods using the dosimetry calculation methods described in section 2.4.4 for the special case of bone lesions of patients with mCRPC receiving ^{177}Lu -PSMA therapy.

Existing publications that reported tumor absorbed dose estimates for ^{177}Lu -PSMA therapy predominantly used the S values of the unit density sphere model for tumors (e.g. the following publications [55], [67], [68], [10], [69], [70]). No separation or possible adaptation of dosimetry method was described between bone lesions and e.g. lymph node metastases. This motivated the extensive comparison of dosimetry calculations.

Methods

Patients suffering from prostate cancer with pronounced metastatic spread to the skeleton were chosen for this investigation. Irreversible anonymized data from 15 patients was retrospectively analysed. This study protocol was approved by the ethics committee of LMU Munich (20-520).

Dosimetry estimation was performed for the first cycle of ^{177}Lu -PSMA-I&T therapy. Quantitative ^{177}Lu SPECT/CT (QSPECT) imaging was performed at 24 h, 48 h and 72 h p.i. according to the routine clinical workflow of ^{177}Lu -PSMA therapy of our institution.

The alignment of QSPECT and CT images from the different time points was performed using rigid co-registration to the reference of 24 h QSPECT/CT image with PMOD. Volumes of interest (VOI) included the whole body, kidneys, and bone lesions. The whole body VOI was obtained by threshold-based VOI definition and the kidney VOIs by manual segmentation on the 24 h CT image. The before mentioned k-means based cluster segmentation was used for bone lesion VOI definition on the 24 h QSPECT image. These VOIs were transferred to the co-registered 48 h and 72 h QSPECT images for retrieval of VOI activities over time. The subsequent VOI-wise fitting was performed using a mono-exponential fit function to obtain the effective VOI half-lives $\lambda_{eff,VOI}$. A voxel-wise time-integrated activity map was obtained using the $\lambda_{eff,VOI}$ per VOI and the 24 h QSPECT image according to formula 3.4 (p. 42), which was identified as a robust compromise during preliminary work of this study.

$$\tilde{A}^{voxel} = \frac{A_{t=0}^{voxel}}{\lambda_{VOI}} = \frac{A_{t=24h}^{voxel} \cdot e^{\lambda_{VOI} \cdot t(t=24h)}}{\lambda_{VOI}}. \quad (3.4)$$

The flowchart in figure 3.13 (p. 41) gives an overview of the herein included dosimetry estimation methods for bone lesions. Absorbed dose calculation was performed using the organ/tumor S value (TSV) approach, VSV approaches for either soft tissue or cortical bone and combinations thereof, and full patient-individual MC absorbed dose simulations. The latter served as the ground truth for the comparison of all dosimetry methods. The unit density sphere approach for tumors used the S values from OLINDA/EXM™2.0 from HERMES Medical Solutions. The time-integrated activity in the bone lesion was retrieved per VOI from the time-integrated activity map to enable a comparison with the 3D voxel-wise dosimetry methods. The absorbed dose per lesion VOI was calculated

by multiplying the time-integrated activity in the lesion with the related lesion S value. The VSV approaches were described in detail in the related publication (given in section 8) and the absorbed dose images are obtained from convolution of the patient-individual time-integrated activity map with the related VSVs.

Full patient-individual MC absorbed dose simulation used the patient CT image, the conversion of HU to densities according to Schneider et al. [48] and the patient-individual time-integrated activity map as input. All MC simulations were performed with GATE version 8.2, which was build on GEANT4 version 10.5.1. The tabulated Schneider conversion was included in the GATE MC code and converted the patients CT image voxel-wise into a material and density geometry for simulation.

The VSV based methods and the full patient-individual MC simulation reveal 3D absorbed dose images, while the TSV approach reveals mean tumor absorbed doses. A drawback of the TSV and VSV approach is their limited applicability to heterogeneous tissue regions, compare with the overview in table 2.1 (p. 18). A CT-based density weighting was thus included into this investigation to overcome this limitation.

The CT-based density weighting approach incorporated the conversion of HU to densities from Schneider et al. [48] to transform the patient CT into a voxel-wise density map. The average bone lesion densities were then calculated based on the density map per lesion VOI.

Using these density maps, the 3D absorbed dose maps obtained from the voxel S value approaches were weighted voxel-wise using the actual voxel density ρ_{voxel} and the density which was assumed during simulation of VSVs, ρ_{VSV} , compare with formula 3.5 (p. 43) [71].

$$D_{weighted}^{voxel} = D^{voxel} \cdot \frac{\rho_{VSV}}{\rho_{voxel}}. \quad (3.5)$$

The mean tumor absorbed dose estimates from the TSV approach were weighted with the average lesion density $\bar{\rho}_{lesion}$. Consequently, the lesion absorbed dose D^{lesion} was multiplied with the ratio $\frac{1g/cm^3}{\bar{\rho}_{lesion}}$.

The average lesion absorbed dose estimates from 3D absorbed dose images of MC simulations were obtained in line with equation 6.3 of ICRU Report 86 [72] to enable a comparison to the average lesion absorbed dose estimates obtained from the TSV dosimetry method. Percentage differences were calculated according to 3.6 (p. 43):

$$PD = \frac{\bar{D}_{method} - \bar{D}_{MC}}{\bar{D}_{MC}}. \quad (3.6)$$

For the 3D dosimetry methods, the PD was calculated voxel-wise for the 3D absorbed dose maps obtained from the VSV methods against MC.

Results

The investigation included in total 289 bone lesions. The PD for the TSV method against the full MC reference dose is visualized in plot 3.14 (p. 44).

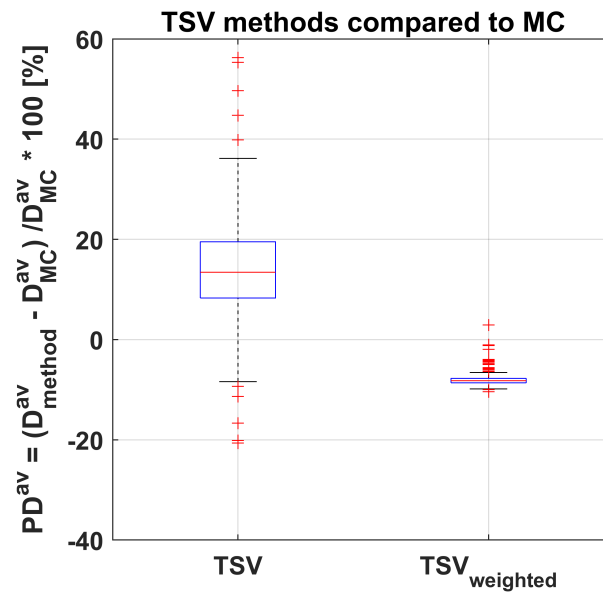


Figure 3.14: Percentage difference of average lesion absorbed dose from TSV methods compared against MC.

The results of the voxel-wise comparison of the 3D dosimetry methods were averaged per lesion VOI and are given in figure 3.15 (p. 45). The weighted VSV approaches showed similar absorbed dose estimates with little deviation from full MC absorbed dose simulation.

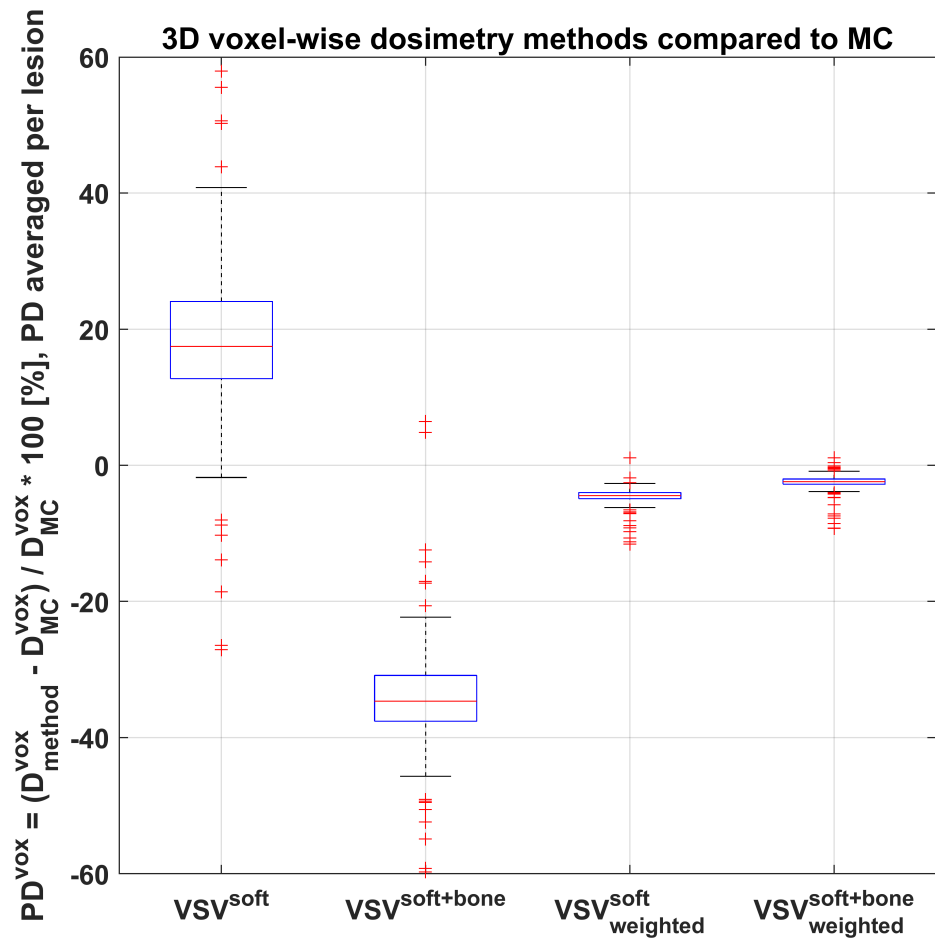


Figure 3.15: Percentage difference compared per voxel and then averaged per lesion VOI.

Chapter 4

Contributions to the original publications included in this work

This chapter 4 is included to summarize and explicitly state my own contributions to the preliminary work and the two original publications upon which this cumulative dissertation is based.

Section 3.2.2:

I planned all SPECT/CT and PET/CT phantom measurements with ^{90}Y and $^{99\text{m}}\text{Tc}$, which are described in sections 3.2.2 and 3.2.3 respectively. Furthermore, I filled and prepared the NEMA IEC Body Phantom SetTM for all scans. All SPECT/CT and PET/CT scans were performed by me. I evaluated different reconstruction parameter sets for all scans in view of image quality and quantification. The results were included in publication I in chapter 7 [60].

Section 3.2.3:

Section 3.2.3 summarizes the first original publication given in chapter 7. The study on the impact of the underlying activity imaging method on the absorbed dose estimate for HCC patients receiving ^{90}Y SIRT was designed and planned in collaboration with all co-authors. PD Dr. Andrei Todica and PD Dr. Harun Ilhan assisted in reviewing the available patient data for dosimetry evaluation. I developed the adapted scaled $^{99\text{m}}\text{Tc}/^{90}\text{Y}$ SPECT/CT based dosimetry approach and further optimized the ^{90}Y BRS SPECT/CT and ^{90}Y PET/CT based dosimetry approaches. I carried out all data analyses starting with co-registration of the multi-modality image data and the segmentation of tumor and healthy liver parenchyma for all patients. Further, I developed a MATLAB code for the generation of the scaled $^{99\text{m}}\text{Tc}/^{90}\text{Y}$ SPECT/CT image, the time-integration of all activity images (i.e. ^{90}Y BRS SPECT/CT, ^{90}Y PET/CT, and scaled $^{99\text{m}}\text{Tc}/^{90}\text{Y}$ SPECT/CT) as well as the subsequent convolution of all time-integrated activity images per patient with the ^{90}Y absorbed dose kernel for ICRP soft tissue. The ^{90}Y absorbed dose kernel was derived with FLUKA MC simulations by me with guidance of Dr. Astrid Gosewisch. The evaluation of average absorbed dose estimates for tumors and healthy liver was performed by me using PMOD, while for the comparison of 3D absorbed dose distributions, I developed a MATLAB code to extract the minimum absorbed doses to 25%, 50%, and 75% of the VOI volumes on all three absorbed dose images per patient. The comparison of results using percentage differences, boxplots, Pearson's correlation

coefficient and Bland-Altman plots was scripted into a MATLAB code by me. PD Dr. Andrei Todica and PD Dr. Harun Ilhan guided me in the interpretation of the Bland-Altman plots. All obtained results and my interpretations built thereupon were critically discussed together with PD Dr. Guido Böning and Dr. Astrid Gosewisch.

Section 3.3.2:

All processing and analyses as described in section 3.3.2 were exclusively performed by me. The obtained results for the creation of 3D time-integrated activity images using the described hybrid VOI/voxel-wise approach based on the 24h QSPECT/CT were then included in the methods of publication II in chapter 8.

Section 3.3.3:

All co-authors contributed to the conceptual design of the study on the impact of absorbed dose estimation method on bone lesion absorbed dose estimates for ^{177}Lu -PSMA therapy of patients with mCRPC (publication II is summarized in section 3.3.3, and given in chapter 8). I decided to investigate dosimetry methods for bone lesions, which show heterogeneous density values. Hence, I investigated clinical available dosimetry approaches such as TSV and VSV, and extended them by proper density weighting to enable comparison against sophisticated MC absorbed dose estimation. The clinical data was reviewed in collaboration with Dr. Astrid Gosewisch, PD Dr. Andrei Todica, PD Dr. Harun Ilhan, and PD Dr. Guido Böning. The radiopharmaceutical was produced for the clinical routine by Dr. Franz Josef Gildehaus. With assistance of Dr. Carlos Uribe, I implemented and validated the MC absorbed dose simulation using the GATE MC code based on GEANT4. I simulated all VSVs for ^{177}Lu in ICRP soft tissue and ICRP cortical bone with GATE. I carried out all patient data processing including co-registration of the 24h, 48h, and 72h ^{177}Lu QSPECT/CT images, VOI definition, VOI statistics extraction, fitting, and time-integration according to the results from section 3.3.2. I exclusively performed all full patient-individual MC absorbed dose simulations. These MC simulations were split into multiple sub-simulations running on different CPUs to speed up the overall simulation time. I created MATLAB scripts to split the MC simulation into sub-simulations, to start the GATE simulations and to merge the results for deposited energy per voxel, absorbed dose per voxel and statistical uncertainty per voxel from all sub-simulations. Besides, I developed a MATLAB code for convolution of the VSVs with the patient's time-integrated activity maps for the unweighted VSV methods, VSV^{soft} and $VSV^{soft+bone}$ respectively. I extended this code to load the patient's CT and voxel-wise convert HU values to density values and to export a density map. In a next step, I used the average densities per bone lesion for $TSV_{weighted}$ to weight the average tumor absorbed dose estimates, which I've obtained with the TSV method using the total time-integrated activity per bone lesion and the related TSV. The beforehand described MATLAB code was further extended by me to include voxel-wise density weighting of the 3D absorbed dose maps from the VSV^{soft} and $VSV^{soft+bone}$ methods, yielding $VSV_{weighted}^{soft}$ and $VSV_{weighted}^{soft+bone}$. Lastly, I calculated percentage differences per bone lesion for the TSV method against the MC average lesion absorbed dose estimate and assessed the percentage difference on a voxel level for all 3D dosimetry methods. Furthermore, I included Bland-Altman plots into the analyses of absorbed dose estimates. My results and my interpretation of these findings were critically reflected with PD Dr. Guido Böning, Prof. Dr. Sibylle Ziegler, Dr. Anna Celler, Dr. Carlos Uribe and Dr. Astrid Gosewisch.

Chapter 5

Discussion

The demand for routine clinical dosimetry increases with the steadily increasing number of nuclear medicine therapies per year. A better understanding of patient- and lesion-individual therapy response using patient-individual 3D image based dosimetry would enable adjustments in therapy activity and thus personalized therapy. In addition, dosimetry offers the potential to gain insight to organ at risk absorbed dose tolerance. As a consequence, routine dosimetry would allow to improve therapy outcome and to move the field towards personalized medicine based on the estimated absorbed doses [73]. Thus, dosimetry is not only necessary in a retrospective setting but rather required to actively plan radionuclide therapies and subsequent therapy cycles.

To allow for routine clinical dosimetry, it is essential to investigate all steps within the general dosimetry workflow (see figure 2.7, p. 12): from quantitative post-therapeutic imaging of the radionuclide distribution, processing and generation of time-integrated activity on an image or volume of interest level and subsequent dosimetry estimation. Each of these steps is exhibiting uncertainties of a certain degree. Hence, an understanding of the associated difficulties of the dosimetry workflow per radionuclide therapy is indispensable to meet the noble goal of a certain standardization. This could be obtained by extensive studies of image quantification, bio-kinetic behaviour and absorbed dose estimation with complex absorbed dose estimation techniques. It is clear, that the most individual dosimetry approach of a full patient MC simulation might currently not be feasible in clinical routine, moreover this might not necessarily be required [42] [71] [74]. Furthermore, the gain of accuracy which is obtained by using MC absorbed dose simulation is limited if the underlying activity imaging data present with a large range of uncertainties. Therefore, the second step is to explore possible simplifications within the dosimetry workflow per therapy to enable an implementation into clinical routine. It is emphasized that this second step should furthermore address the comparability of outcome and effort of the investigated dosimetry workflows.

As briefly mentioned above, the choice of dosimetry method and processing of image data for 3D image based dosimetry is crucial. The absorbed dose estimates from different nuclear medicine therapy centres could potentially vary to a large extent in dependence of the underlying dosimetry workflow. Consequently, it may be advisable to transparently report the methods being involved for dose estimation using standard nomenclature according to MIRD [75]. In addition, instead of reporting a single dose value, which suggests a certain accuracy of the dose estimation procedure, it may be beneficial to report dose ranges which reflect the uncertainties of dosimetry. This could facilitate the interpretation of reported absorbed dose estimates as well as the derivation of dose-response

relationships. The presented work investigated the absorbed dose estimate dependence on the underlying imaging method for ^{90}Y SIRT of patients with HCC and on the chosen dosimetry method for the special case of bone lesion absorbed dose estimates in ^{177}Lu -PSMA therapy of patients suffering from mCRPC.

1): Quantitative activity measurement

Although ^{90}Y SIRT has been performed for years, no post-therapeutic dosimetry has been introduced into the clinical therapy workflow yet. The major reason hindering the dosimetry estimation is the difficulty of quantitative ^{90}Y imaging. The ^{90}Y phantom measurements in this work thus were necessary to assess the image acquisition and reconstruction parameters of ^{90}Y BRS SPECT/CT imaging and to establish ^{90}Y PET/CT imaging in our institution. By investigating different sphere-to-background activity concentration ratios in the NEMA IEC Body Phantom SetTM, and different acquisition and reconstruction parameters, it was possible to implement a ^{90}Y PET/CT acquisition protocol with appropriate reconstruction parameters. This further enabled an adjustment of the ^{90}Y BRS SPECT/CT reconstruction to improve both, image quality (signal-to-noise-ratio) and quantification accuracy (recovery coefficient). An increase of image noise was observed for increasing number of iterations during reconstruction though the recovery coefficients increased too. The choice of image updates was therefore carefully made to find a trade-off between image noise and increase in recovery coefficient. However, taking into account image 3.9 (p. 35), it is obvious that ^{90}Y PET/CT is superior to ^{90}Y BRS SPECT/CT. Further investigations are required to improve ^{90}Y BRS SPECT/CT imaging and could possibly include appropriate MC based modelling of the ^{90}Y bremsstrahlung implemented into the SPECT reconstruction as described by Dewaraja et al. [76].

Quantitative ^{177}Lu imaging was already implemented into the routine clinical therapy workflow in our institution, however, there are ongoing attempts worldwide regarding single time point dosimetry for different ^{177}Lu therapies [77] [78]. This is highly controversial and requires extensive future investigations, since most kinetics of OARs and tumors as well as the kinetic behaviour over different therapy cycles, e.g. in ^{177}Lu -PSMA therapy, yet remain unknown.

2): Identification of tumors and organs

Since tumor uptake and size might vary over time as a response to the treatment, it remains open for subsequent investigations if the herein used k-means based cluster segmentation for lesion VOI definition is applicable over multiple therapy cycles with the same parameters. For tumor segmentation in ^{90}Y SIRT, it depends on the capability of the MR imaging to allow for proper delineation of the tumor borders.

3): Fit of model function to data points

The ^{90}Y microspheres are not subject to pharmacokinetics. Therefore, single time point activity imaging is assumed to be sufficient and the fitting as well as time-integration of activity is facilitated compared to other internal radionuclide therapies. However, although the formula 3.1 (p. 26) for the generation of a 3D voxel time-integrated activity map in ^{90}Y SIRT is in theory simple, its applicability highly depends on the accurate quantitative imaging of $A(t)$. Since ^{90}Y PET/CT shows improved quantification capabilities compared to ^{90}Y BRS SPECT/CT [79] [80], it is clearly favorable as a basis for absorbed dose estimation. In concordance with Kafrouni et al. [81], it is possible to use the distribution information from the pre-therapeutic $^{99\text{m}}\text{Tc}$ -MAA SPECT/CT as a surrogate for the ^{90}Y microsphere distribution. The subsequent voxel-wise scaling with the administered ^{90}Y therapy activity allows to use this scaled $^{99\text{m}}\text{Tc}/^{90}\text{Y}$ SPECT/CT approach for dosimetry.

Three quantitative ^{177}Lu SPECT/CTs (24 h, 48 h, 72 h p.i.) are regularly acquired in our institution to assess the pharmacokinetic behaviour of ^{177}Lu -PSMA. Different fit functions and combinations thereof are available. In this work, a mono-exponential fit function was used as described by Gosewisch et al. [66]. In contrast, for example Jackson et al. [82] use multiphase models for description of the time-activity curve of ^{177}Lu -PSMA. However, the creation of a 3D voxel time-integrated activity map is in general more challenging for ^{177}Lu -PSMA therapy than for the permanently implanted ^{90}Y microspheres. Since voxel-wise fitting and subsequent time-integration is highly dependent on accurate co-registration and possibly impacted by image artifacts in individual voxels, we herein investigated a hybrid VOI-/voxel-wise approach for fitting and time-integration. Making use of formula 3.4 (p. 42), we assume to be more robust to possibly misaligned voxels.

4): Conversion to dose

A voxel S value convolution approach revealing a 3D dose map with possible subsequent density weighting has been identified as a dosimetry approach with appropriate accuracy and ease to use for clinical routine for both therapies. Though, this could introduce further blurring of the absorbed dose image for ^{90}Y . The possible reasons are the blur in ^{90}Y BRS SPECT caused by the β^- range before bremsstrahlung production and the blur in ^{90}Y PET caused by the positron range before annihilation.

Taking into account the promising results of this work (see section 3.2, and publication I, [60]) and the patient example in figure 5.1 (p. 52), this suggests a comprehensive analysis of existing ^{90}Y SIRT patient data without ^{90}Y PET/CT imaging. The application of the scaled $^{99\text{m}}\text{Tc}/^{90}\text{Y}$ SPECT/CT dosimetry approach facilitates the derivation of a healthy liver parenchyma absorbed doses tolerance to prevent from radiation induced liver disease. Furthermore, a tumor absorbed dose-response relationship may be achieved. The proposed dosimetry approach based on the scaled $^{99\text{m}}\text{Tc}/^{90}\text{Y}$ SPECT is

restricted to patients with comparable ^{99m}Tc -MAA and ^{90}Y microsphere distributions. Hence, it would be desirable to investigate a quantitative measure to define this comparability. An extension of the investigations to tumor entities different from HCC is clinically requested.

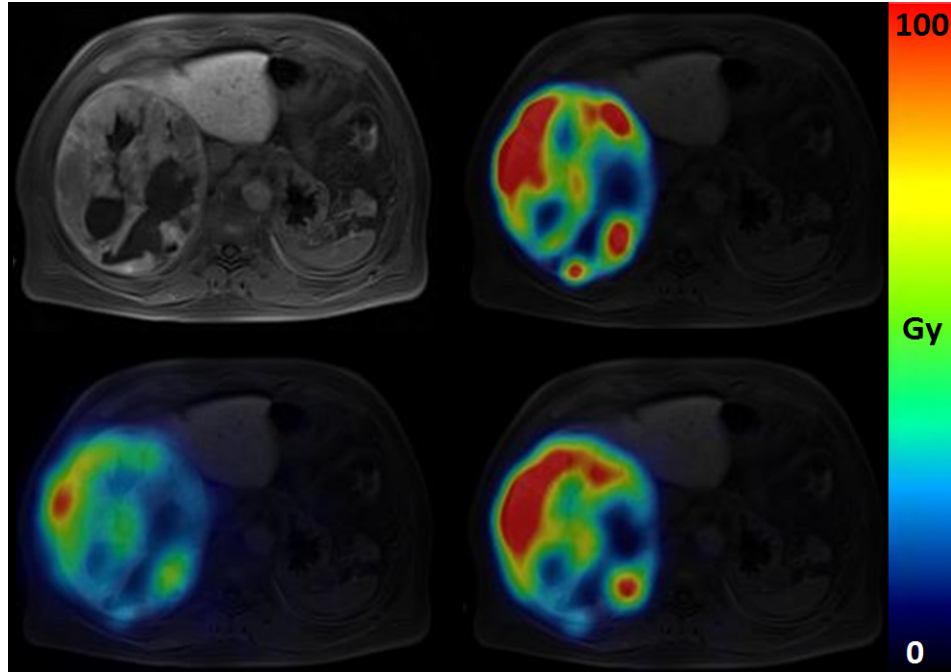


Figure 5.1: Pre-therapeutic MR image of a patient suffering from HCC and transversal slices of the 3D absorbed dose maps for ^{90}Y SIRT. Top right: scaled $^{99m}\text{Tc}/^{90}\text{Y}$ SPECT/CT based; bottom left: ^{90}Y BRS SPECT/CT based; bottom right: ^{90}Y PET/CT based.

But how to understand a heterogeneous therapy response of a patient including responding and non-responding metastases despite receiving multiple cycles of ^{177}Lu -PSMA therapy? Would another cycle of ^{177}Lu -PSMA therapy be justified in this situation? In an attempt to address these questions it is initially required to obtain a better understanding of target absorbed dose-response relationships. Tumor absorbed dose estimation becomes even more important when OAR absorbed dose thresholds are not yet met and it might be an option to increase the therapy activity aiming at increased tumor absorbed doses. However, tumor absorbed dose alone might not be sufficient to answer the questions above but also radiopharmaceutical accumulation and distribution within the tumor is of importance.

As a first step towards answering these questions, this work focussed on an improved absorbed dose estimation for bone lesions in mCRPC patients receiving ^{177}Lu -PSMA therapy. So far, the dosimetry methods reported in the literature have limited capabilities to address the heterogeneous density and mass distributions of bone lesions. With our analyses, we aimed at providing a robust basis for tumor absorbed dose estimation in ^{177}Lu -PSMA therapy. For this purpose, we compared different dosimetry approaches with varying complexity against full patient-individual MC absorbed dose simulation.

The Bland-Altman analysis of the different 3D voxel-wise dosimetry methods compared for D75 against the reference method of MC absorbed dose simulation is shown in figure 5.2 (p. 53). The smallest differences were found for the voxel S value approaches with subsequent density weighting. This observation supports its implementation into the ^{177}Lu -PSMA therapy workflow.

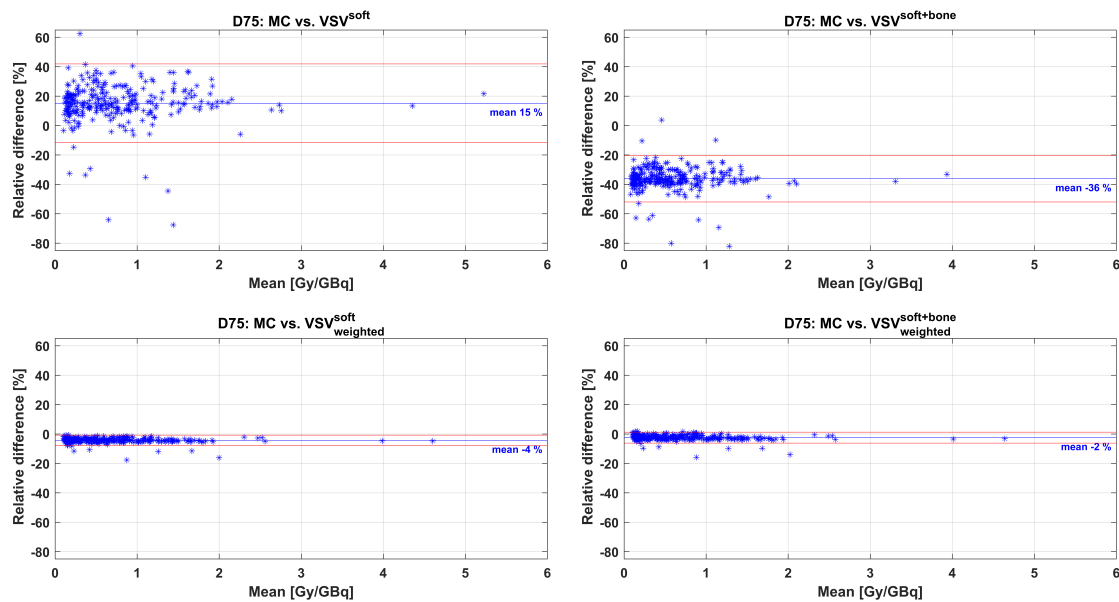


Figure 5.2: Bland-Altman plot for the minimum absorbed dose to 75 % of the bone lesion VOI volume (D75) compared for the 3D voxel-wise dosimetry methods against MC.

Dosimetry on a voxel level is limited by the voxel's uncertainty related to image artifacts, noise and co-registration as discussed by Bardiès and Chiesa [83]. However, especially in the field of ^{90}Y SIRT there is added benefit of voxel-wise dosimetry compared against average lesion absorbed dose estimation. Here, the combination of 3D absorbed dose maps and dose volume histograms (DVH) can assist the analysis of therapy response by providing information of the dose distribution within a lesion. For the herein investigated 3D dosimetry methods for ^{177}Lu -PSMA therapy, the 3D absorbed dose map may provide additional information in view of therapy response analysis of individual lesions. With the additional voxel-wise density weighting a comparable absorbed dose distribution like the full MC simulation was achieved as highlighted by the patient example in figure 5.3 (p. 54) and the DVH of an exemplary bone lesion in figure 5.4 (p. 54).

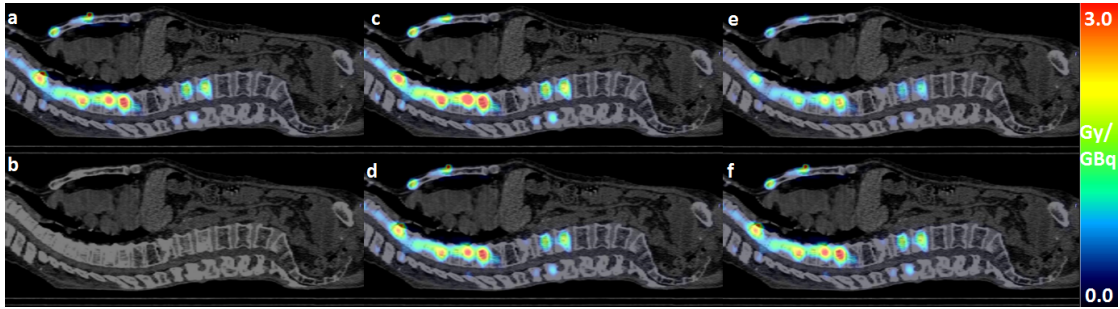


Figure 5.3: Sagittal slices of 3D absorbed dose maps fused with the CT image (b) of a mCRPC patient receiving ^{177}Lu -PSMA therapy; (a) shows the result of the full MC simulation; (c) displays the result of the application of voxel S values for soft tissue, weighted with voxel-wise density in (d); (e) stands for the use of voxel S values for soft tissue and cortical bone, and with subsequent voxel-wise density weighting in (f).

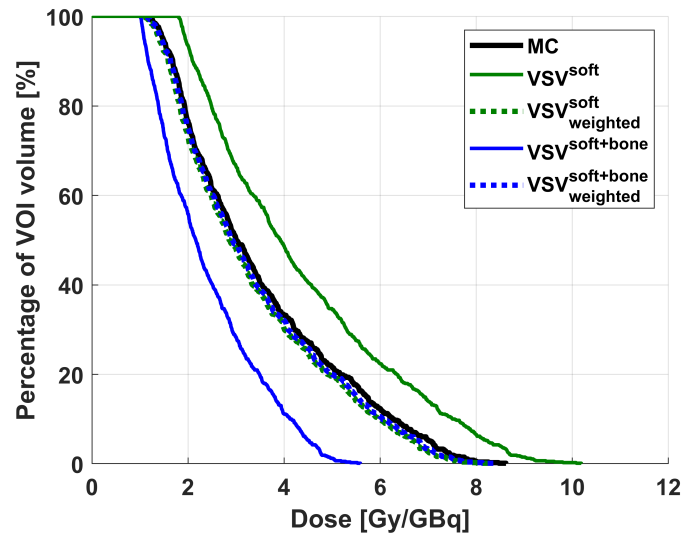


Figure 5.4: DVH of an exemplary bone lesion of a mCRPC patient receiving ^{177}Lu -PSMA therapy.

To summarize, pre- and post-therapeutic dosimetry is indispensable to actively plan individualized internal radionuclide therapies with appropriately tailored therapy activities. To allow for such personalized internal radionuclide therapies, a profound knowledge of the dose-response relationship is mandatory. However, the required correlation between absorbed dose estimates and therapeutic effect may not be observed, if the uncertainties of all involved processing steps of the dosimetry workflow (figure 2.7, p. 12) can not be reduced. The herein investigated 3D image based dosimetry approaches for ^{90}Y SIRT and ^{177}Lu -PSMA offer reduced uncertainties and thus support improved assessment of therapy response. Consequently, this work might assist ongoing research towards personalized internal radionuclide therapies.

Chapter 6

Conclusion

This work investigated the full dosimetry workflow for ^{90}Y SIRT of the liver and ^{177}Lu -PSMA therapy of prostate cancer. Although the therapy concept and related challenges differ for both therapies, the feasibility of patient-individual, 3D image based post-therapeutic absorbed dose estimation was demonstrated.

The described scaled $^{99\text{m}}\text{Tc}/^{90}\text{Y}$ SPECT/CT based dosimetry approach showed good agreement to ^{90}Y PET/CT based absorbed dose estimates for HCC patients. Subsequent investigations should include an increased number of patients as well as analyses of different tumor entities. A combination with therapy outcome data can assist to retrieve dose-response relationships for ^{90}Y SIRT of the liver.

For bone lesion dosimetry of mCRPC patients receiving ^{177}Lu -PSMA therapy, 3D voxel-wise dosimetry using voxel S values with subsequent voxel-wise density correction compared well with computationally-demanding full MC absorbed dose simulation. Further, the evidence to account for density differences during absorbed dose estimation for bone lesions was emphasized.

To conclude, the future of nuclear medicine therapies should feature patient-individual absorbed dose estimation for all kinds of internal radionuclide therapies and the investigation of therapy outcome prediction based on pre-therapeutic data.

Chapter 7

Publication I



Original paper

3D image-based dosimetry for Yttrium-90 radioembolization of hepatocellular carcinoma: Impact of imaging method on absorbed dose estimates

Julia Brosch^{a,*}, Astrid Gosewisch^a, Lena Kaiser^a, Max Seidensticker^b, Jens Ricke^b, Johannes Zellmer^a, Peter Bartenstein^a, Sibylle Ziegler^a, Harun Ilhan^a, Andrei Todica^a, Guido Böning^{a,*}

^a Department of Nuclear Medicine, University Hospital, Ludwig-Maximilians-University Munich, Munich, Germany

^b Department of Radiology, University Hospital, Ludwig-Maximilians-University Munich, Munich, Germany

ARTICLE INFO

Keywords:

Radioembolization
SIRT
Yttrium-90
Dosimetry
Yttrium-90 PET
Bremsstrahlung SPECT

ABSTRACT

Background: To improve therapy outcome of Yttrium-90 selective internal radiation therapy (⁹⁰Y SIRT), patient-specific post-therapeutic dosimetry is required. For this purpose, various dosimetric approaches based on different available imaging data have been reported. The aim of this work was to compare post-therapeutic 3D absorbed dose images using Technetium-99m (^{99m}Tc) MAA SPECT/CT, Yttrium-90 (⁹⁰Y) bremsstrahlung (BRS) SPECT/CT, and ⁹⁰Y PET/CT.

Methods: Ten SIRTs of nine patients with unresectable hepatocellular carcinoma (HCC) were investigated. The ^{99m}Tc SPECT/CT data, obtained from ^{99m}Tc-MAA-based treatment simulation prior to ⁹⁰Y SIRT, were scaled with the administered ⁹⁰Y therapy activity. 3D absorbed dose images were generated by dose kernel convolution with scaled ^{99m}Tc/⁹⁰Y SPECT/CT, ⁹⁰Y BRS SPECT/CT, and ⁹⁰Y PET/CT data of each patient. Absorbed dose estimates in tumor and healthy liver tissue obtained using the two SPECT/CT methods were compared against ⁹⁰Y PET/CT.

Results: The percentage deviation of tumor absorbed dose estimates from ⁹⁰Y PET/CT values was on average $-2 \pm 18\%$ for scaled ^{99m}Tc/⁹⁰Y SPECT/CT, whereas estimates from ⁹⁰Y BRS SPECT/CT differed on average by $-50 \pm 13\%$. For healthy liver absorbed dose estimates, all three imaging methods revealed comparable values.

Conclusion: The quantification capabilities of the imaging data influence ⁹⁰Y SIRT tumor dosimetry, while healthy liver absorbed dose values were comparable for all investigated imaging data. When no ⁹⁰Y PET/CT image data are available, the proposed scaled ^{99m}Tc/⁹⁰Y SPECT/CT dosimetry method was found to be more appropriate for HCC tumor dosimetry than ⁹⁰Y BRS SPECT/CT based dosimetry.

1. Background

Yttrium-90 selective internal radiation therapy (SIRT) became an established treatment option for hepatocellular carcinoma (HCC) and many other liver tumor entities [1]. To ensure safe delivery of the ⁹⁰Y microspheres with limited shunt to the lung and extra-hepatic regions, a treatment simulation with Technetium-99m-labeled macroaggregated

albumin (^{99m}Tc-MAA) followed by a planar gamma camera image and a SPECT/CT scan is performed prior to therapy [2]. Patient-individual planning of absorbed dose for ⁹⁰Y SIRT is performed in a majority of centers [3]. But although the European council directive 2013/59/Euratom emphasizes the need of patient-individual absorbed dose verification [4], post-therapeutic ⁹⁰Y dosimetry is not yet part of the clinical routine [5].

Abbreviations: ⁹⁰Y, Yttrium-90; SIRT, Selective internal radiation therapy; HCC, Hepatocellular carcinoma; ^{99m}Tc, Technetium-99m; MAA, Macroaggregated albumin; SPECT, Single photon emission computed tomography; BRS, Bremsstrahlung; PET, Positron Emission Tomography; CT, Computed Tomography; PM, Partition model; MIRL, Medical internal radiation dosimetry; mBSA, Modified body surface area; LSF, Lung shunt fraction; FOV, Field of view; VOI, Volume of interest; TOF, Time of flight; CF, Calibration factor; MAP, Maximum a posteriori; DK, Dose kernel; ICRP, Internal commission on radiological protection; RC, Recovery coefficient; SNR, Signal-to-noise ratio.

* Corresponding authors at: Department of Nuclear Medicine, University Hospital, LMU Munich, Marchioninistrasse 15, 81377 Munich, Germany.

E-mail address: Julia.Brosch@med.uni-muenchen.de (J. Brosch).

<https://doi.org/10.1016/j.ejmp.2020.11.016>

Received 20 May 2020; Received in revised form 9 November 2020; Accepted 11 November 2020

1120-1797/© 2020 Associazione Italiana di Fisica Medica. Published by Elsevier Ltd. This is an open access article under the CC BY-NC-ND license

(<http://creativecommons.org/licenses/by-nc-nd/4.0/>).

For patient individualized therapy with improved therapy outcome as well as for a safe administration of further treatment cycles, an individualized dosimetry for tumor and healthy liver parenchyma after ^{90}Y SIRT is advisable [6].

In this regard, ^{90}Y bremsstrahlung (BRS) SPECT/CT imaging has been the method of choice for visual post-therapeutic treatment verification. While ^{90}Y PET/CT imaging gained increasing importance over the past few years [7], this method is still less established and available in clinical routine. Although ^{90}Y PET imaging is affected by the low branching ratio of ^{90}Y for internal pair production of $(31.86 \pm 0.47) \times 10^{-6}$ [8], several phantom studies addressing the optimal ^{90}Y PET imaging and reconstruction parameters have shown the feasibility of ^{90}Y PET [9,10]. Others investigated the optimal ^{90}Y BRS imaging parameter choice and reconstruction methods [11,12], and deduced that ^{90}Y BRS SPECT imaging is still less capable of correctly quantifying activity distributions due to the significantly large electron range, the continuous nature of the bremsstrahlung spectrum and the lack of a discrete photopeak suitable for imaging. Yue et al. and Elschot et al. further investigated the quantification accuracies of ^{90}Y BRS SPECT/CT and ^{90}Y PET/CT for dosimetry purposes using phantom measurements [13,14] and concluded that the quantification accuracy of ^{90}Y PET is superior to ^{90}Y BRS SPECT. However, up to now no standardized clinical scan protocol, neither for ^{90}Y PET/CT nor ^{90}Y BRS SPECT/CT, has been defined. Therefore, inter-center comparability of image based ^{90}Y dosimetry is limited, independent of the various existing dosimetric calculation methods [15].

Pre-therapeutic absorbed dose estimation in ^{90}Y SIRT is often performed based on $^{99\text{m}}\text{Tc}$ -MAA SPECT/CT imaging, relying either on the partition model (PM) or on the tumor and organ S-value based dosimetry as described by the medical internal radiation dosimetry (MIRD) formalism [16–21]. A drawback of these methods is the related assumption of a homogeneously distributed activity within the liver, which neglects the patient-individual ^{90}Y microsphere distribution. These approaches consequently show a limited applicability in SIRT dosimetry, only being suitable for estimating an overall mean absorbed dose for either tumorous or healthy liver parenchyma. A few studies have already addressed alternative methods for 3D dosimetry for ^{90}Y SIRT based on $^{99\text{m}}\text{Tc}$ -MAA SPECT/CT [22–24]. However, Ulrich et al., Wondergem et al., and Knešaurek et al. were critical about the comparability of uptake patterns from pre-therapeutic $^{99\text{m}}\text{Tc}$ -MAA SPECT/CT and post-therapeutic ^{90}Y microsphere imaging [25–27]. Additionally, several groups investigated post-therapeutic 3D dosimetry methods using ^{90}Y BRS SPECT/CT or ^{90}Y PET/CT [9,28–30].

It can be summarized that each of the different processing strategies and associated imaging methods for ^{90}Y SIRT dosimetry has its individual limitations. Consequently, no standard methodology for ^{90}Y SIRT related imaging and image processing has been established so far [15]. The aim of this study was therefore to assess the comparability of the absorbed dose estimates of tumorous and healthy liver tissue and to quantify differences in dependence of the available imaging method, namely $^{99\text{m}}\text{Tc}$ -MAA SPECT/CT and ^{90}Y BRS SPECT/CT in comparison to ^{90}Y PET/CT.

2. Material and methods

2.1. Phantom measurements

To enable a better interpretation of the absorbed dose estimates obtained from $^{99\text{m}}\text{Tc}$ -MAA SPECT/CT, ^{90}Y BRS SPECT/CT and ^{90}Y PET/CT, the capability to quantify known activity concentrations of each imaging procedure was determined by phantom measurements. For this purpose, a NEMA IEC Body PhantomTM with six fillable spheres (inner diameters: 10 mm, 13 mm, 17 mm, 22 mm, 28 mm, 37 mm) was filled with a sphere to background activity concentration ratio of 8:1. The total $^{99\text{m}}\text{Tc}$ phantom activity was 495.6 MBq and was defined such that the activity concentration in the phantom background corresponds to an

average activity concentration in the liver of exemplary patients receiving $^{99\text{m}}\text{Tc}$ -MAA. The total ^{90}Y phantom activity was 1.88 GBq of ^{90}Y chloride with added DTPA to avoid sticking to the phantom walls and to mimic typical maximum ^{90}Y SIRT activities in our institution. The $^{99\text{m}}\text{Tc}$ SPECT/CT, ^{90}Y BRS SPECT/CT and ^{90}Y PET/CT acquisition and reconstruction parameters were in concordance with the corresponding routine clinical patient protocols, which are described in the following sections. Spherical volumes of interest (VOIs) with a diameter according to the phantom specifications were placed on the accompanying CT image, and a box-shaped VOI with 1700 ml volume was placed in the phantom background. The recovery coefficients (RC) for spheres and the phantom background were determined according to equation (1) by dividing the average activity concentrations of the spheres and background in the corresponding image by the known activity concentration,

$$\text{RC} = \frac{C_{\text{image}}}{C_{\text{known}}} \cdot 100 \quad (1)$$

with RC being the recovery coefficient, C_{image} the activity concentration in Bq/ml obtained from the reconstructed image, and C_{known} the known activity concentration in Bq/ml in the phantom. The signal-to-noise ratios (SNR) of the images were calculated by dividing the difference of the activity concentrations in the sphere VOIs and the background VOI by the standard deviation in the background VOI, as given by equation (2) [31],

$$\text{SNR} = \frac{C_{\text{sphere}} - C_{\text{background}}}{\sigma_{\text{background}}} \quad (2)$$

with SNR being the signal-to-noise ratio, C_{sphere} the activity concentration in Bq/ml per sphere VOI, $C_{\text{background}}$ the activity concentration in Bq/ml in the background VOI, and $\sigma_{\text{background}}$ the standard deviation of the background VOI in Bq/ml.

2.2. Patient selection, therapy procedure and image acquisition

2.2.1. Patient selection

This study was conducted retrospectively on anonymized data from ten SIR-therapies of nine patients suffering from hepatocellular carcinoma (HCC). The study protocol was approved by the local ethics committee. Written informed consent was obtained from all patients. Patients underwent radioembolization with Yttrium-90-labeled resin microspheres (SIR-Spheres, Sirtex Medical Ltd., Australia) as a lobar or sequential lobar treatment under fluoroscopic guidance. MR-imaging with a liver specific contrast agent was performed before therapy and treatment simulation. All patients received a treatment simulation with $^{99\text{m}}\text{Tc}$ -MAA followed by planar scintigraphy of the thorax and the abdomen to quantify the liver to lung shunt fraction (LSF) and a SPECT/CT of the abdominal area to exclude extra-hepatic tracer accumulation. The ^{90}Y therapy activity was either determined using the modified body surface area (mBSA) method or the partition model (PM) with the aim to deliver at least 120 Gy to the tumor while keeping the absorbed dose to the healthy liver tissue considerably low between 40 and 60 Gy depending on the patient's liver function [2,16]. Patient characteristics and corresponding therapy activities are summarized in table 1. For post-therapeutic treatment verification, a ^{90}Y BRS SPECT/CT scan and a ^{90}Y PET/CT scan were acquired.

2.2.2. Image acquisition and reconstruction

2.2.2.1. $^{99\text{m}}\text{Tc}$ -MAA-SPECT/CT. Within 1.5 h post injection of $^{99\text{m}}\text{Tc}$ -MAA into the (right and/or left) hepatic artery according to the planned catheter position for radioembolization, the patients were examined on a dual-head Symbia T2 SPECT/CT (Siemens Healthcare, Germany) with a low-energy-high-resolution collimator. SPECT projections were acquired with an energy window centered at the $^{99\text{m}}\text{Tc}$ photopeak of 140 keV ($\pm 7.5\%$) and with an additional scatter window at 115 keV ($\pm 10\%$)

Table 1

Patient characteristics including the administered ^{99m}Tc activity, lung shunt fraction (LSF), SIRT activity calculation method and the ^{90}Y activity derived by the activity in the FOV of the ^{90}Y PET image. One lesion was evaluated per SIR-therapy.

Patient no.	Age	Sex [m/f]	^{99m}Tc activity [MBq]	LSF [%]	^{90}Y SIRT activity calculation	^{90}Y activity [MBq]	Treated liver volume [ml]	Tumor volume [ml]
1	71	m	99	9.6	mBSA	1266	2135	1162
2	79	m	91	7.7	PM	2431	2093	1760
3	65	m	62	4.1	PM	1110	687	514
4	77	m	88	5.0	mBSA	1224	820	55
5	64	m	94	4.8	mBSA	1046	232	129
6	36	f	74	4.3	PM	1807	922	389
7	48	f	94	2.4	mBSA	718	533	37
8 - SIRT 1	65	m	105	5.3	PM	735	692	50
8 - SIRT 2					PM	547	197	16
9	81	f	87	3.8	PM	1295	2135	400

in a 128x128 matrix with 32 angular steps per head with 25 s per step [2]. Quantitative SPECT reconstruction was performed (5 MAP iterations, 16 subsets, penalty of 0.001, collimator-specific depth-dependent detector response, voxel size (4.7952 mm³) [32] using the corresponding low dose CT (voxel size 0.9766 × 0.9766 × 5.0 mm³) for attenuation correction and the dual energy window method for scatter correction. A previously determined nuclide-, collimator- and camera-specific calibration factor, derived from a cylindrical phantom, was used for converting the measured counts per second per voxel to Becquerel per milliliter.

2.2.2.2. ^{90}Y BRS SPECT/CT. The ^{90}Y BRS SPECT/CT data were acquired within 24 h post SIR-therapy using the same camera as has been utilized for the ^{99m}Tc -MAA SPECT/CT, equipped with a medium-energy-low-penetration collimator. As proposed by Siman et al. [33], a primary energy window was set at 108 keV (±20%) and a background energy window at 360 keV (±15%). Projections were recorded in a 128x128 matrix with 32 angular steps per head with a duration of 40 s per step. SPECT reconstruction (15 MAP iterations, 16 subsets, penalty of 0.01, voxel size (4.7952 mm³) used the low dose CT (voxel size 0.9766 × 0.9766 × 5.0 mm³) to account for attenuation in the primary energy window and included the background compensation method proposed by Siman et al. [33] using the background energy window. This approach was considered as a good compromise for semi-quantitative ^{90}Y BRS imaging, since appropriate modelling of electron transport and bremsstrahlung production as well as detector and collimator response for bremsstrahlung radiation in ^{90}Y BRS SPECT/CT image reconstruction is not yet available. Consequently, we observed a space-variant and object-dependent relation between reconstructed counts per second per voxel and true activity. Based on the assumptions that the majority of the administered activity remained stationary in the liver and that the entire liver was contained within the field of view (FOV) of the ^{90}Y BRS SPECT/CT volume, we performed a self-calibration of each reconstructed ^{90}Y BRS SPECT/CT study. The individual calibration factor (CF) was obtained by dividing the decay corrected ^{90}Y therapy activity obtained from ^{90}Y PET FOV by the sum of reconstructed counts per second in the entire ^{90}Y BRS SPECT/CT FOV volume and by the related voxel volume to obtain Becquerel per milliliter [34].

2.2.2.3. ^{90}Y PET/CT. All patients received a ^{90}Y time-of-flight (TOF) PET/CT acquisition (Biograph mCT flow, VG60A, Siemens Healthcare, Germany) of the liver within 24 h post SIR-therapy in flow mode using a table scan speed of 0.2 mm/s [35] and a low dose CT (voxel size 1.5234 × 1.5234 × 3.0 mm³). The radioisotope ^{90}Y was selected for acquisition and Siemens TrueX TOF image reconstruction was performed with 2 iterations and 21 subsets in a 128x128 matrix (voxel size 6.3638 × 6.3638 × 3.0 mm³) with a 10 mm FWHM post-reconstruction Gaussian filter.

2.2.2.4. Image processing. The ^{90}Y BRS SPECT/CT, ^{90}Y PET/CT and corresponding MR image were all co-registered with a rigid registration

method and sampled to the CT voxel size of 0.9766 × 0.9766 × 5.0 mm³ of the ^{99m}Tc -MAA SPECT/CT scan with PMOD (v4.003; PMOD Technologies LLC). The total administered ^{99m}Tc activity was derived by calculating the sum of activity values over all voxels over the entire SPECT FOV from the calibrated ^{99m}Tc -MAA SPECT/CT. Similarly, the administered ^{90}Y activity was obtained from the decay corrected sum of the activity values per voxel over all voxels in the entire PET FOV. We decided to use this approach to provide a similar basic procedure for all investigated patients, because for the radioembolization procedure in our institution it is possible that occasionally not the full amount of prescribed ^{90}Y -SIR-Spheres is administered for patient safety reasons and to prevent flow stasis [5,15]. Moreover, with the dose calibrator response being very sensitive to changes in the volume [36] and geometry [37] for ^{90}Y , it becomes difficult to accurately measure the ^{90}Y residual activity in the vial and tubes of the application system in the dose calibrator. In contrast, the reproducibility of the estimated ^{90}Y therapy activity by the total FOV activity of the PET/CT device has been shown by Carlier et al. [38] with a proportionality coefficient of 1.04 ± 0.02.

2.3. Dosimetry calculation

2.3.1. Generation of absorbed dose images

Based on the assumptions that the ^{90}Y SIR-Spheres are trapped in the liver tissue and that due to the embolization effect no sphere migration occurs during SIRT and post-therapeutic imaging [5], a single image at one time point was considered to be sufficient for dosimetric estimations in SIRT. In our institution, the treatment simulation with ^{99m}Tc -MAA is performed in a single procedure with application of ^{99m}Tc -MAA according to the planned catheter position or positions of the subsequent SIRTs in a lobar or sequential setting. Thus, the actual treated volume in each SIRT had to be detected. For each of the sequential SIRTs, this treated liver volume was determined by applying a 10% iso-contour VOI on the corresponding post-therapeutic ^{90}Y BRS SPECT volume. This threshold was determined with the ^{90}Y BRS SPECT/CT phantom image and provided a reproducible delineation of the treated liver volume at ^{90}Y SIRT. It was in good agreement with the treated liver lobe or liver segment, when displayed with the corresponding CT and MR images as verified by an experienced nuclear medicine physician. The quantitative whole liver ^{99m}Tc -MAA SPECT/CT was divided by the total administered ^{99m}Tc activity and then scaled with the total administered ^{90}Y therapy activity within the treated liver volume VOI using an in-house developed MATLAB code (R2018b; The MathWorks, Inc. Natick, MA), similar to the normalization approach by Kafrouni et al. [39]. Outside the VOI of the treated liver volume, the image contents were set to zero. The resulting scaled $^{99m}\text{Tc}/^{90}\text{Y}$ activity image consequently represented the pre-therapeutic distribution pattern of ^{99m}Tc -MAA as well as the total administered therapeutic ^{90}Y activity and was considered as a surrogate for the local ^{90}Y distribution. Assuming no redistribution of activity after administration, the time-integrated activity images were obtained by dividing each of the three activity images – scaled

$^{99m}\text{Tc}/^{90}\text{Y}$ SPECT/CT based, ^{90}Y BRS SPECT/CT based and ^{90}Y PET/CT based – by the decay constant of ^{90}Y [40]. 3D absorbed dose images were generated by convolving these time-integrated activity images with a 3D ^{90}Y absorbed dose kernel which was derived by Monte Carlo simulations (FLUKA Monte Carlo code [41]) for ICRP soft tissue.

2.3.2. Tumor and healthy liver mean absorbed doses

The tumor was manually delineated on the pre-therapeutic MR image using PMOD (v4.003; PMOD Technologies LLC). This tumor VOI was then copied to the scaled $^{99m}\text{Tc}/^{90}\text{Y}$ SPECT/CT based, ^{90}Y BRS SPECT/CT based, and ^{90}Y PET/CT based absorbed dose images to determine the corresponding estimates of mean tumor absorbed doses. To allow the assessment of the absorbed dose estimates to the healthy liver tissue, a healthy liver VOI was derived by subtracting the tumor VOI from the treated liver VOI. The mean absorbed dose to the healthy liver tissue was then determined by applying the healthy liver VOI to the scaled $^{99m}\text{Tc}/^{90}\text{Y}$ SPECT/CT based, ^{90}Y BRS SPECT/CT based, and ^{90}Y PET/CT based absorbed dose images. Additionally, the relative percentage deviations with respect to ^{90}Y PET/CT were calculated for the tumor and liver absorbed dose estimates for the scaled $^{99m}\text{Tc}/^{90}\text{Y}$ SPECT/CT and ^{90}Y BRS SPECT/CT. Pearson's correlation and *t*-test for paired samples were conducted with MATLAB and Bland-Altman analysis [42] was performed to compare the obtained absorbed dose estimates.

2.3.3. 3D absorbed dose distributions

The 3D absorbed dose images based on scaled $^{99m}\text{Tc}/^{90}\text{Y}$ SPECT/CT, ^{90}Y BRS SPECT/CT, and ^{90}Y PET/CT were analyzed quantitatively by assessment of the minimum absorbed doses to 25%, 50% and 75% (hereafter referred to as D25, D50, D75) of the tumor VOI and healthy liver tissue VOI. D25, D50, and D75 consequently represent the absorbed doses that are at least received in 25%, 50%, and 75% of the VOI volume.

3. Results

3.1. Phantom measurements

To visualize the difference between the three imaging methods, a transversal slice of the phantom is displayed in Fig. 1 for ^{90}Y BRS SPECT/CT, ^{99m}Tc SPECT/CT and ^{90}Y PET/CT, each scaled to 80% of its maximum. The RC and SNR determined by the phantom measurements are shown in Fig. 2 for the four largest sphere diameters. With the investigated imaging methods ^{90}Y BRS SPECT/CT, ^{99m}Tc SPECT/CT and ^{90}Y PET/CT, recovery coefficients of 37%, 75% and 83% were achieved for the largest sphere (37 mm diameter, 26 ml), while the corresponding RCs for the background VOI were 101%, 95% and 96%.

3.2. Mean tumor and healthy liver absorbed dose

3.2.1. Mean tumor absorbed dose

The estimated mean tumor absorbed dose for all patients was $81 \pm$

57 Gy for scaled $^{99m}\text{Tc}/^{90}\text{Y}$ SPECT/CT and 88 ± 50 Gy for ^{90}Y PET/CT, whereas an overall smaller mean tumor absorbed dose estimate of 41 ± 19 Gy was obtained from ^{90}Y BRS SPECT/CT. The tumor absorbed dose estimates per patient are given in table 2. This observation is illustrated in Fig. 3 a. The mean percentage difference of tumor absorbed dose estimates compared to ^{90}Y PET/CT was $-2 \pm 18\%$ (min: -37% , max: $+23\%$) for scaled $^{99m}\text{Tc}/^{90}\text{Y}$ SPECT/CT and $-50 \pm 13\%$ (min: -66% , max: -16%) for ^{90}Y BRS SPECT/CT. Fig. 3 b shows both SPECT/CT based tumor absorbed dose estimates plotted against those of the ^{90}Y PET/CT for each patient. A strong correlation was found between scaled $^{99m}\text{Tc}/^{90}\text{Y}$ SPECT/CT and ^{90}Y PET/CT ($r = 0.88$, $p = 0.29$), and between ^{90}Y BRS SPECT/CT and ^{90}Y PET/CT based absorbed dose values ($r = 0.94$, $p \ll 0.01$). The Bland-Altman plots of tumor absorbed dose estimates from scaled $^{99m}\text{Tc}/^{90}\text{Y}$ SPECT/CT and ^{90}Y BRS SPECT/CT compared to ^{90}Y PET/CT are given in Fig. 4 a and b. Smaller differences in tumor absorbed dose estimates were found for scaled $^{99m}\text{Tc}/^{90}\text{Y}$ SPECT/CT (95% confidence interval: -32.9 Gy to 47.3 Gy, mean difference: 7.2 Gy) than for ^{90}Y BRS SPECT/CT (95% confidence interval: -4.6 Gy to 98.8 Gy, mean difference: 47.1 Gy) compared to ^{90}Y PET/CT based absorbed dose estimates.

3.2.2. Mean healthy liver absorbed dose

The mean absorbed dose to the healthy liver tissue was determined to 19 ± 23 Gy, 18 ± 7 Gy and 22 ± 16 Gy for scaled $^{99m}\text{Tc}/^{90}\text{Y}$ SPECT/CT, ^{90}Y BRS SPECT/CT and ^{90}Y PET/CT based absorbed dose images, respectively. Hence, the mean percentage difference of estimated absorbed dose to healthy liver tissue compared to ^{90}Y PET/CT was $-10 \pm 8\%$ (min: -21% , max: $+5\%$) for scaled $^{99m}\text{Tc}/^{90}\text{Y}$ SPECT/CT and $-12 \pm 10\%$ (min: -31% , max: $+6\%$) for ^{90}Y BRS SPECT/CT. Table 2 shows healthy liver absorbed dose estimates per patient. In concordance with the observation made for the tumors in the previous section, a strong correlation was found between ^{90}Y BRS SPECT/CT and ^{90}Y PET/CT based absorbed dose values ($r = 0.94$, $p \ll 0.01$), and between scaled $^{99m}\text{Tc}/^{90}\text{Y}$ SPECT/CT and ^{90}Y PET/CT based absorbed dose values ($r = 0.98$, $p \ll 0.01$). The absorbed dose to healthy liver and the correlation of the two SPECT/CT based methods compared to ^{90}Y PET/CT are illustrated in Fig. 5. In Fig. 6, Bland-Altman plots of healthy liver absorbed dose estimates are shown. The absorbed dose differences for healthy liver for scaled $^{99m}\text{Tc}/^{90}\text{Y}$ SPECT/CT (95% confidence interval: -1.2 Gy to 5.5 Gy, mean difference: 2.1 Gy) and for ^{90}Y BRS SPECT/CT (95% confidence interval: -2.7 Gy to 8.9 Gy, mean difference: 3.1 Gy), each compared with ^{90}Y PET/CT based absorbed dose estimates, showed similar ranges and mean differences.

3.3. 3D absorbed dose distributions

Fig. 7 documents exemplarily the 3D absorbed dose images of patient 2 for all three imaging methods, superimposed onto the pre-therapeutic MR image. This Fig. 7 illustrates the overall smaller absorbed dose estimates in ^{90}Y BRS SPECT/CT based absorbed dose images compared to the scaled $^{99m}\text{Tc}/^{90}\text{Y}$ SPECT/CT and ^{90}Y PET/CT based absorbed dose images, which both express comparable intensities in the same

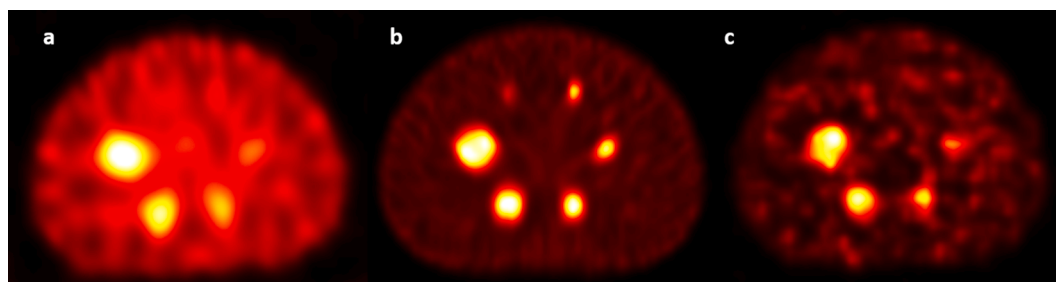


Fig. 1. Transversal slices of the phantom, each scaled to 80% of its maximum value for better visual comparability for a ^{90}Y BRS SPECT/CT, b ^{99m}Tc SPECT/CT and c ^{90}Y PET/CT.

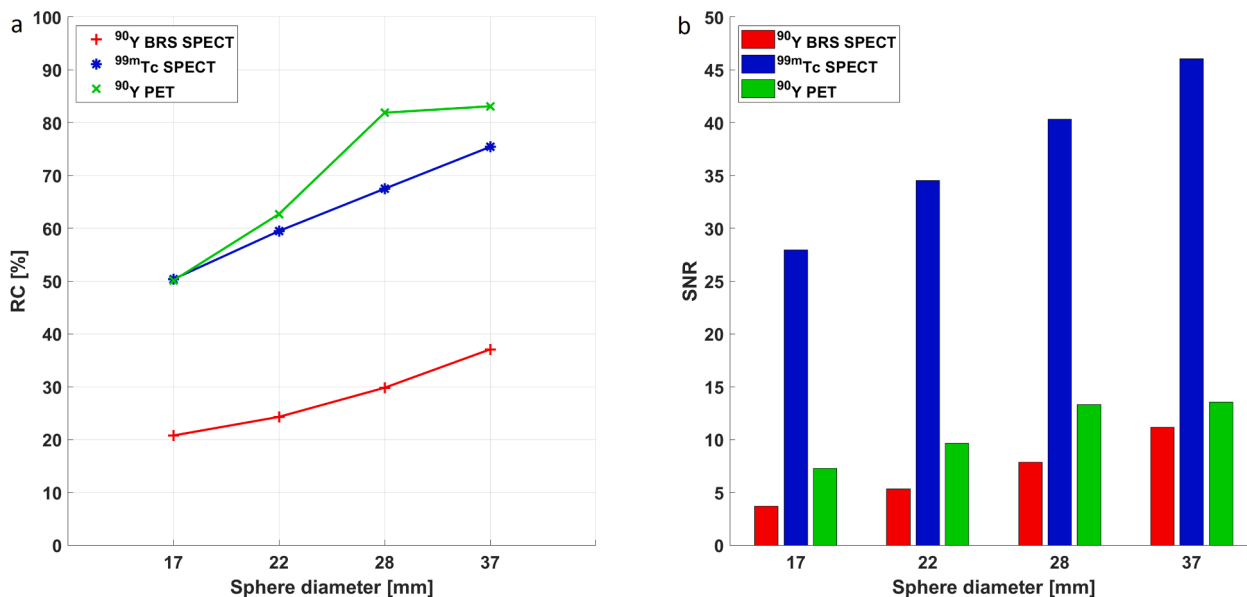


Fig. 2. a Recovery coefficients (RC) and b signal-to-noise ratios (SNR) for the four largest spheres for ^{99m}Tc SPECT/CT and ⁹⁰Y BRS SPECT/CT and ⁹⁰Y PET/CT phantom measurements.

Table 2

Mean tumor and mean healthy liver absorbed dose estimates per patient from scaled ^{99m}Tc/⁹⁰Y SPECT/CT, ⁹⁰Y BRS SPECT/CT and ⁹⁰Y PET/CT.

Patient no.	Tumor absorbed dose [Gy]			Healthy liver absorbed dose [Gy]		
	scaled ^{99m} Tc/ ⁹⁰ Y SPECT/CT	⁹⁰ Y BRS SPECT/CT	⁹⁰ Y PET/CT	scaled ^{99m} Tc/ ⁹⁰ Y SPECT/CT	⁹⁰ Y BRS SPECT/CT	⁹⁰ Y PET/CT
1	24	16	19	4	5	4
2	54	29	52	15	15	16
3	63	30	58	29	22	30
4	81	27	80	18	19	22
5	123	67	165	29	30	30
6	71	59	113	27	27	32
7	107	52	122	26	19	27
8 - SIRT 1	119	49	106	15	16	18
8 - SIRT 2	82	28	69	14	15	17
9	85	52	97	17	17	21

structures. The minimum absorbed dose that is at least received by 25%, 50%, and 75% of the tumor and healthy liver VOI volume is given by D25, D50, and D75 in Gy for scaled ^{99m}Tc/⁹⁰Y SPECT/CT, ⁹⁰Y BRS SPECT/CT, and ⁹⁰Y PET/CT in Fig. 6 a and b for tumor and liver respectively, averaged over the 10 investigated patient data sets.

4. Discussion

The availability of post-therapeutic ⁹⁰Y SIRT dosimetry and the understanding of its strengths and limitations is advantageous to optimize treatment success by maximizing the absorbed dose delivered to the tumor while sparing healthy liver parenchyma. In combination with the retrospective analysis of existing patient data, post-therapeutic ⁹⁰Y SIRT dosimetry could become a valuable and substantial tool to further improve individual therapy outcome, especially if multiple therapy cycles are scheduled for the same patient. However, image based post-therapeutic ⁹⁰Y SIRT dosimetry is rarely implemented into clinical routine workflows, not least due to the differences in available imaging modalities in each center and a lack of consensus on standardized ⁹⁰Y SIRT dosimetry workflows. In the present work, we compared absorbed dose estimates for ten SIR-therapies in nine patients in dependence of the imaging modalities being involved, to mimic different technical

equipment being available in SIRT-performing centers. We namely investigated post-therapeutic dose estimation by making use of the post-therapeutic ⁹⁰Y BRS SPECT/CT, of a combination of pre-therapeutic ^{99m}Tc-MAA SPECT/CT and post-therapeutic ⁹⁰Y BRS SPECT/CT, and of the post-therapeutic ⁹⁰Y PET/CT. The differences in absorbed doses in tumor and healthy liver based on the two SPECT/CT based methods were compared against those being derived from ⁹⁰Y PET/CT. Phantom measurements were included into this work in order to relate the observed absorbed dose estimation in patients to the quantification capabilities and limitations of the three imaging methods based on the patient imaging settings and reconstruction parameters used in this study.

When comparing the mean absorbed doses to healthy liver tissue, the ⁹⁰Y BRS SPECT/CT and the scaled ^{99m}Tc/⁹⁰Y SPECT/CT based dosimetry showed only small deviations from ⁹⁰Y PET/CT dosimetry. A noticeable large overlap of absorbed doses estimated by the three methods was found, as documented in Fig. 5. This is underlined by similar mean differences and ranges in both Bland-Altman plots in Fig. 6. This finding is further confirmed by the observed high quantitative recovery of the large phantom background, which was 101% for ⁹⁰Y BRS SPECT/CT, 95% for ^{99m}Tc SPECT/CT, and 96% for ⁹⁰Y PET/CT. However, regarding the minimal absorbed dose to 25%, 50%, 75% of the respective VOI volume (given by D25, D50, D75, Fig. 8 b), variations were found between the three methods. With respect to the discriminative recovery coefficients and noise characteristics, as assessed by the phantom measurements (see Fig. 2), these variations were likely caused by the differences in spatial resolution and quantification capability of the imaging methods.

Regarding the estimated absorbed doses to the tumors, a close agreement of $-2 \pm 18\%$ averaged over all patients was observed between scaled ^{99m}Tc/⁹⁰Y SPECT/CT and ⁹⁰Y PET/CT. Likewise, the D25, D50, and D75 for tumor absorbed doses in Fig. 8 a show a small deviation between scaled ^{99m}Tc/⁹⁰Y SPECT/CT and ⁹⁰Y PET/CT. These findings have already been indicated by others, see Gnesin et al. [43] and Jadoul et al. [44] using a local deposition dosimetric approach, and Kafrouni et al. [35] and Richetta et al. [45] using a dose kernel approach, who all found a good comparability of ^{99m}Tc-MAA SPECT/CT based and ⁹⁰Y PET/CT based dosimetry in HCC. In addition to their approaches, we further included ⁹⁰Y BRS SPECT/CT based dosimetry to the comparison and observed a notable large underestimation of the tumor absorbed dose estimates of $-50 \pm 13\%$ by ⁹⁰Y BRS SPECT/CT,

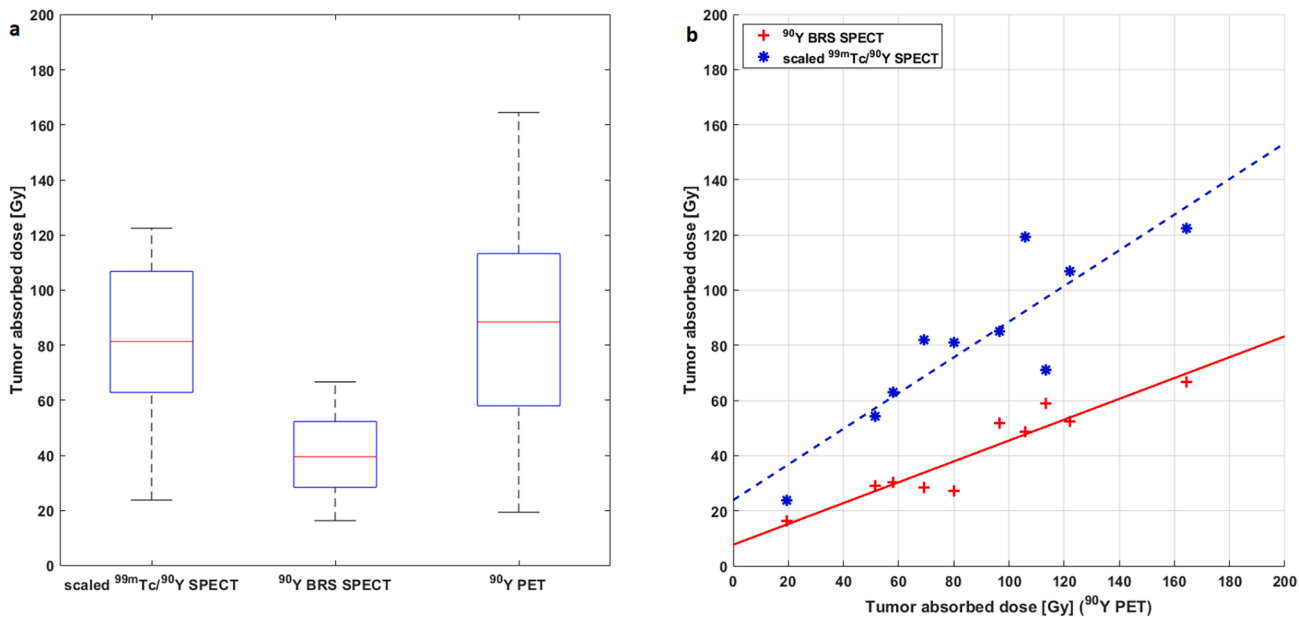


Fig. 3. a) Boxplot of mean tumor absorbed doses obtained by scaled ^{99m}Tc/⁹⁰Y SPECT/CT, ⁹⁰Y BRS SPECT/CT and ⁹⁰Y PET/CT, and b) correlation plot of mean tumor absorbed doses of the two SPECT/CT based methods compared to ⁹⁰Y PET/CT.

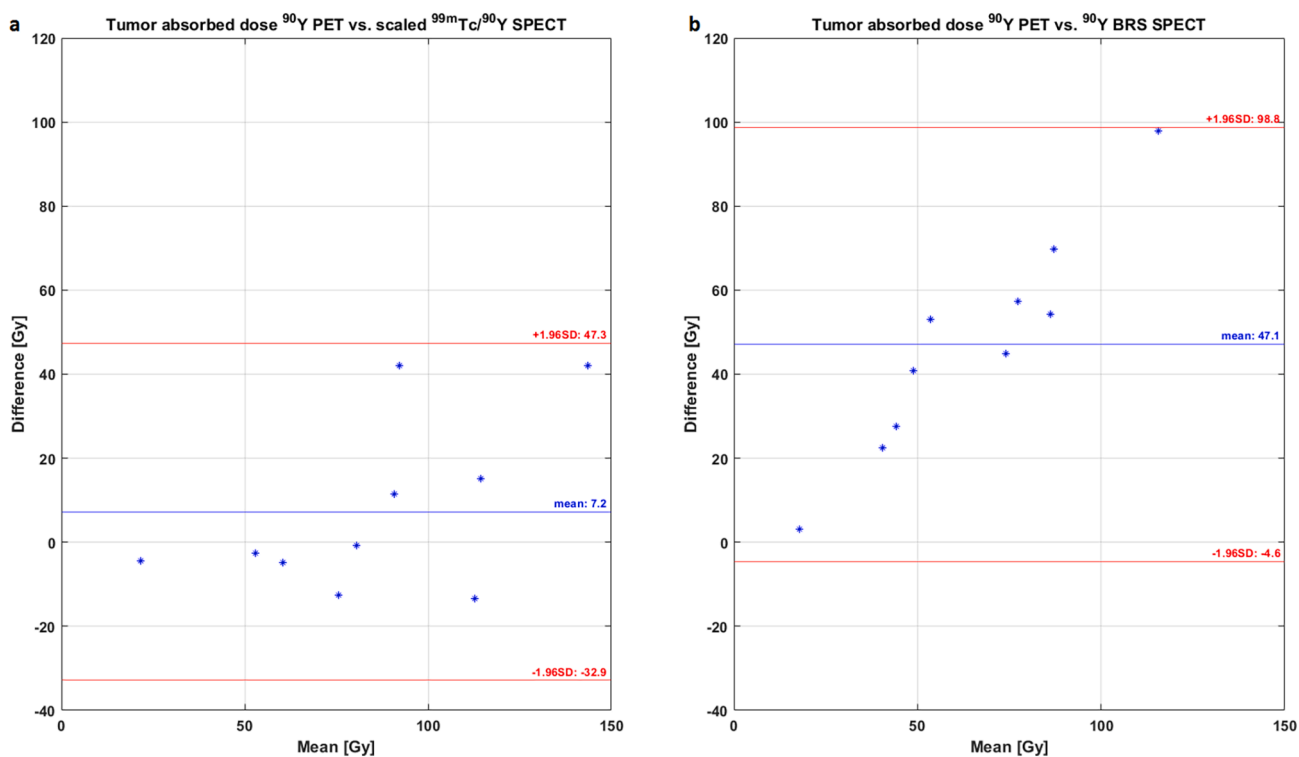


Fig. 4. Bland-Altman plots for tumor absorbed dose for a scaled ^{99m}Tc/⁹⁰Y SPECT/CT compared to ⁹⁰Y PET/CT, and b) ⁹⁰Y BRS SPECT/CT compared to ⁹⁰Y PET/CT.

when compared to ⁹⁰Y PET/CT. This observation is further documented by the significantly reduced values for D25, D50 and D75 in Fig. 8 a, confirming the tendency found with the percentage deviations. The Bland-Altman analysis, shown in Fig. 4, revealed larger mean differences and a larger range of differences for the ⁹⁰Y BRS SPECT/CT dosimetry method compared to ⁹⁰Y PET/CT based dosimetry than for the scaled ^{99m}Tc/⁹⁰Y SPECT/CT dosimetry approach compared to ⁹⁰Y PET/CT.

The exemplary patient absorbed dose images provided in Fig. 7

illustrate the good comparability of scaled ^{99m}Tc/⁹⁰Y SPECT/CT (Fig. 7 b) and ⁹⁰Y PET/CT (Fig. 7 c), while the ⁹⁰Y BRS SPECT/CT (Fig. 7 a) based absorbed dose image expresses overall lower absorbed dose estimates. This observation can be explained by the highly limited capability of accurate activity quantification of ⁹⁰Y bremsstrahlung SPECT, as documented by the overall lower recovery coefficients in the spheres in Fig. 2 a. ^{99m}Tc SPECT/CT and ⁹⁰Y PET/CT, in contrast, presented comparable quantification capabilities in our phantom measurements. It has to be considered, that the quantification capabilities (RCs and SNRs,

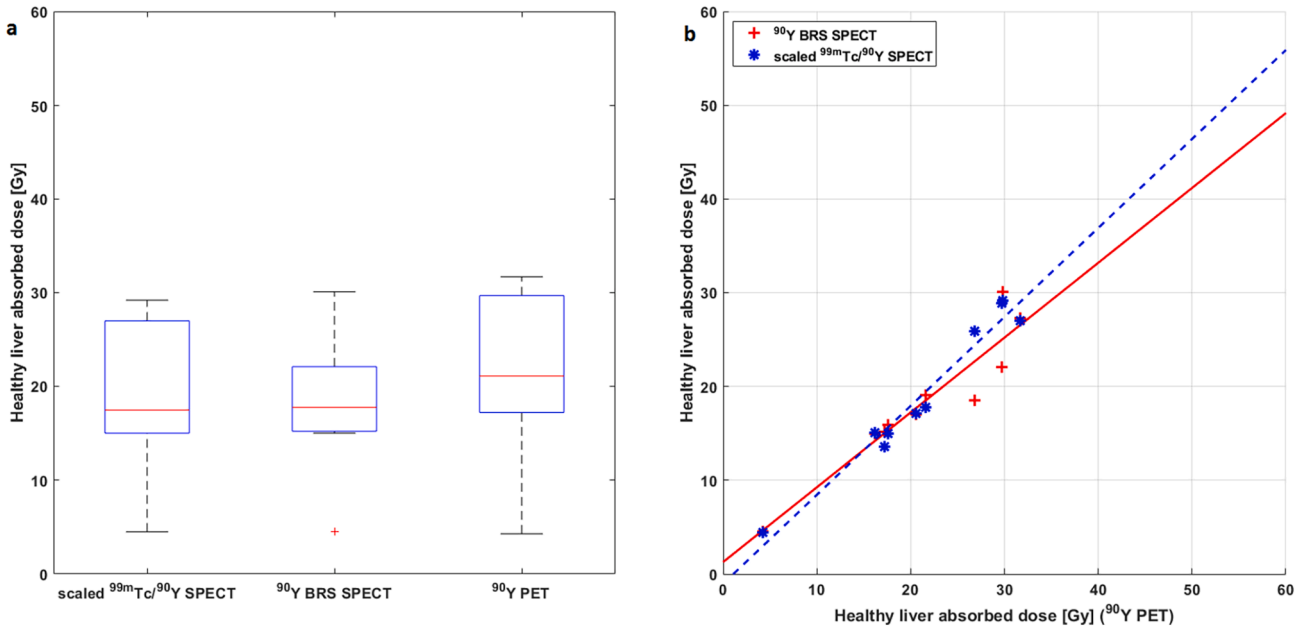


Fig. 5. a) Boxplot of mean absorbed doses to the healthy liver volume obtained by scaled $^{99m}\text{Tc}/^{90}\text{Y}$ SPECT/CT, ^{90}Y BRS SPECT/CT and ^{90}Y PET/CT, and b) correlation plot of mean absorbed doses to the healthy liver tissue of the two SPECT/CT based methods compared to ^{90}Y PET/CT.

see Fig. 2) of the three SIRT-related imaging methods presented in this study were derived from image data which were generated using the standard clinical routine imaging protocols and reconstruction parameters of our institution, without optimization for technical performance evaluations. Previously published studies analyzed ^{90}Y BRS SPECT/CT imaging protocols as well as ^{90}Y BRS SPECT/CT reconstruction [12,33,46–49] and provided recommendations for improved imaging and reconstruction parameters, which could have an impact on the

results presented here. However, the quantification capability of ^{90}Y BRS SPECT/CT is highly object-dependent and still below that of ^{90}Y PET/CT. Evidently, this is confirmed by the underestimation of all presented ^{90}Y BRS SPECT/CT based recovery coefficients and tumor absorbed dose estimates. Since ^{90}Y BRS SPECT/CT quantification capabilities are highly dependent on the image acquisition and reconstruction protocol and therefore may vary between individual treatment centers, this further complicates the comparability of absorbed dose

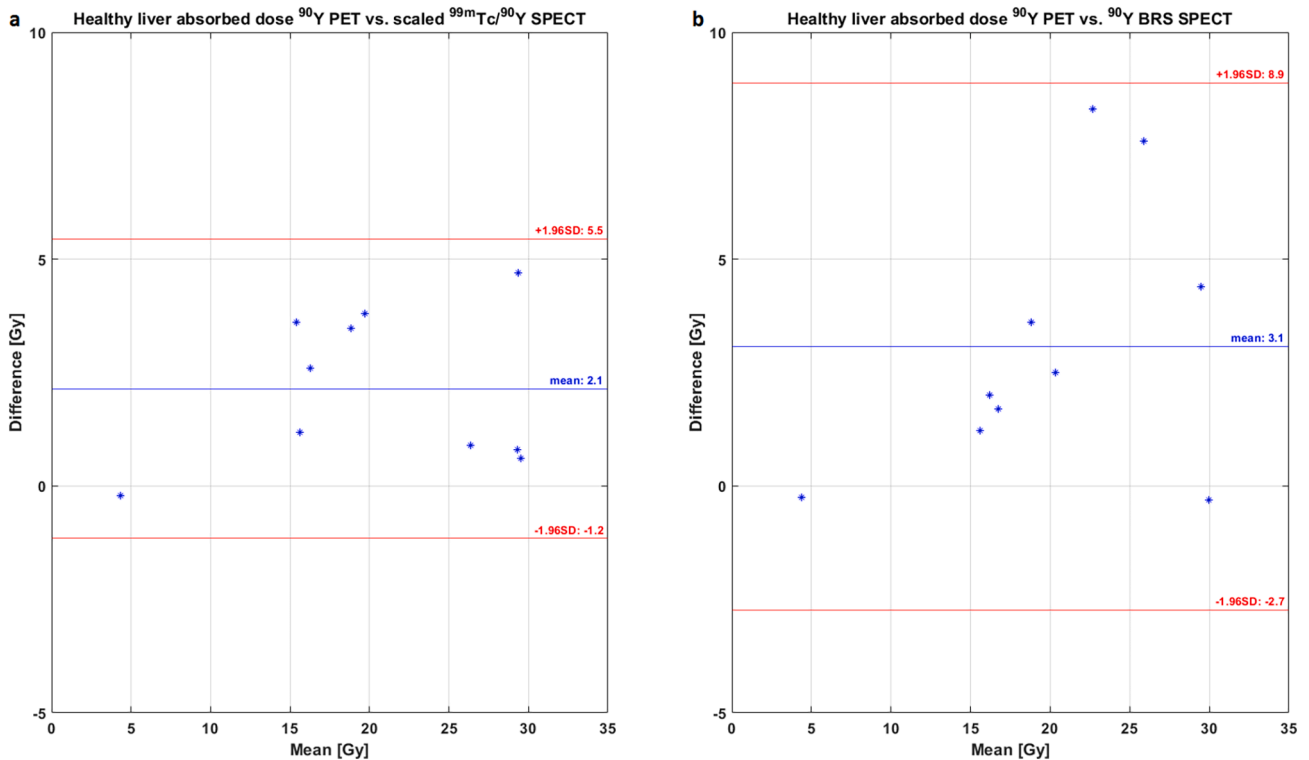


Fig. 6. Bland-Altman plots for healthy liver absorbed dose for a scaled $^{99m}\text{Tc}/^{90}\text{Y}$ SPECT/CT compared to ^{90}Y PET/CT, and b) ^{90}Y BRS SPECT/CT compared to ^{90}Y PET/CT.

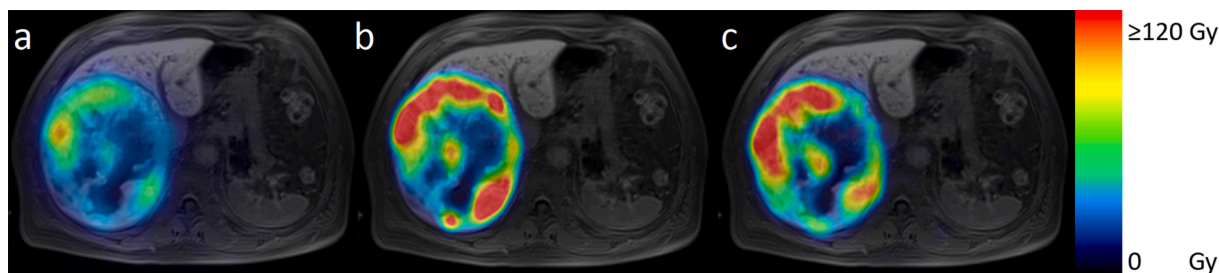


Fig. 7. Absorbed dose images of a ^{90}Y BRS SPECT/CT, b scaled $^{99\text{m}}\text{Tc}/^{90}\text{Y}$ SPECT/CT, c ^{90}Y PET/CT for patient 2.

estimates obtained from ^{90}Y BRS SPECT/CT. On the other hand, the feasibility of ^{90}Y PET/CT based dosimetry, despite the inherent problem of a low count rate when imaging ^{90}Y with PET, has been proven by several studies [9,50,51]. Concordantly, we deduce that ^{90}Y SIRT dosimetry based on post-therapeutic ^{90}Y PET/CT is preferable, as indicated by Gates et al. [52] and Kao et al. [53], due to its superior quantification capabilities. In cases, where ^{90}Y PET/CT is clinically unavailable, and under the assumption that the pre- and post-therapeutic uptake patterns have a high degree of similarity, the use of the scaled $^{99\text{m}}\text{Tc}/^{90}\text{Y}$ SPECT/CT could be a possible alternative for post-therapeutic absorbed dose estimation.

$^{99\text{m}}\text{Tc}$ -MAA SPECT/CT based dosimetry is clearly restricted by the assumption that the distributions of pre-therapeutic $^{99\text{m}}\text{Tc}$ -MAA and therapeutic ^{90}Y microspheres are similar. However, there are differences in particle sizes, the amount of injected particles and the flow characteristics between $^{99\text{m}}\text{Tc}$ -MAA and ^{90}Y microspheres. Furthermore, the uptake of $^{99\text{m}}\text{Tc}$ -MAA depends on the tumor entity [54] and tumor vascularization. In this context, it is important to note that HCC, on which this study is focused, is a hypervascularized tumor. Thus, the results and conclusions do not necessarily apply to hypovascularized tumor entities. The use of $^{99\text{m}}\text{Tc}$ -MAA SPECT/CT for dosimetry for different tumor entities is a highly controversial topic with publications demonstrating or disproving a comparability of $^{99\text{m}}\text{Tc}$ -MAA and ^{90}Y

microsphere distribution for either glass [55–58], or resin microspheres [25–27]. Consequently, post-therapeutic dosimetry should be performed cautiously when being based on a pre-therapeutic $^{99\text{m}}\text{Tc}$ -MAA SPECT/CT. Yet, for the small number of evaluated patient cases included in our study, we observed a good concordance of pre- and post-therapeutic uptake patterns.

Recently, commercially available software including dose kernel dosimetry approaches similar to the one used in our investigations have been tested by Kafrouni et al. [35] and validated by Maughan et al. [59] for ^{90}Y SIRT with ^{90}Y PET/CT. This enables a broader application in clinical routine. However, the large deviations in absorbed dose values observed in our investigation suggest that not only the selected dosimetric concept [28], but also the choice of imaging method needs to be considered to facilitate reliable and comparable dosimetry.

Due to the fact, that this work is a retrospective patient study, the number of available patient data is limited. The acquisition of two post-therapeutic images (^{90}Y BRS SPECT/CT and ^{90}Y PET/CT) is outside of clinical routine. This procedure leads to significantly increased patient discomfort and was therefore only performed if deemed valuable by the treating physician. Nonetheless, this investigation aimed in comparing post-therapeutic 3D absorbed dose images and absorbed dose estimates for tumors and healthy liver tissue using $^{99\text{m}}\text{Tc}$ -MAA SPECT/CT and ^{90}Y BRS SPECT/CT in comparison to ^{90}Y PET/CT. For this purpose, patients

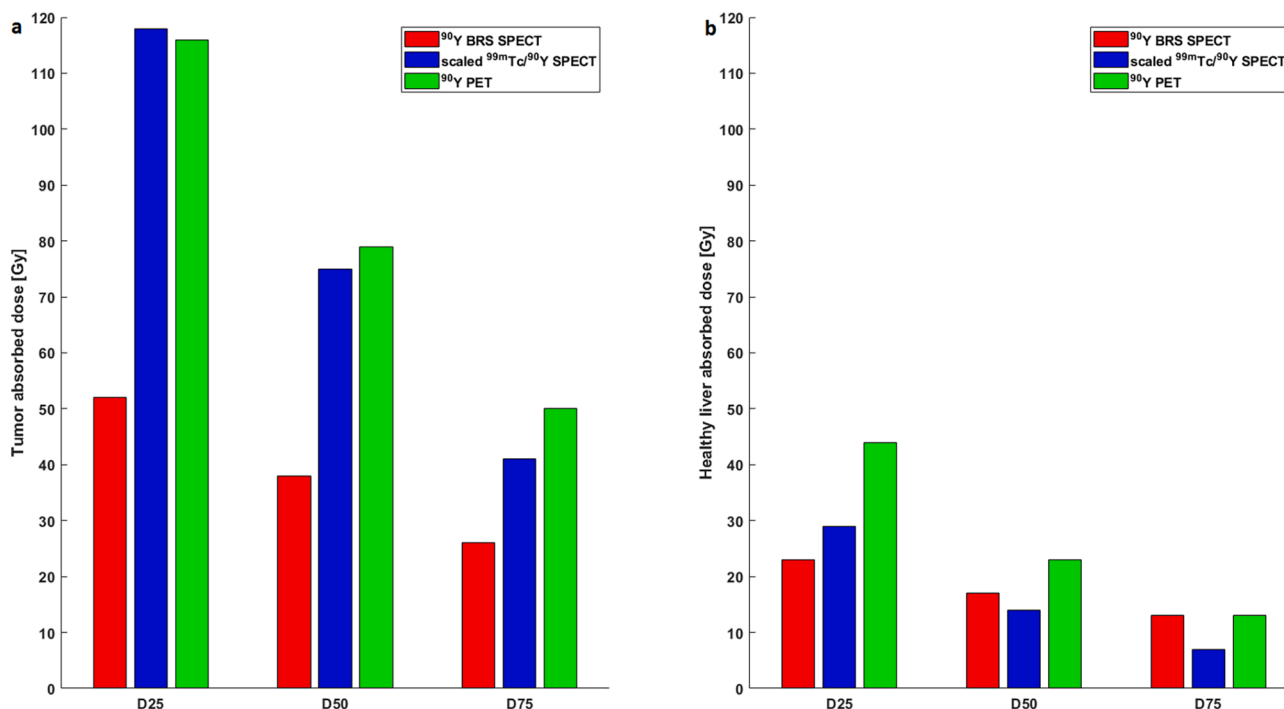


Fig. 8. Minimum absorbed doses to 25%, 50%, and 75% (given by D25, D50, D75) of a the tumor volume and b the healthy liver volume for scaled $^{99\text{m}}\text{Tc}/^{90}\text{Y}$ SPECT/CT, ^{90}Y BRS SPECT/CT and ^{90}Y PET/CT, averaged over all 10 patient data sets. D25, D50, and D75 represent the absorbed doses that are at least received in 25%, 50%, and 75% of the related VOI volume.

suffering from HCC receiving SIRT were retrospectively analyzed with the inclusion criteria of having both, post-therapeutic ^{90}Y BRS SPECT/CT and ^{90}Y PET/CT. Consequently, the comparison of absorbed dose estimates as shown in the present work necessitate additional investigation in a larger cohort. However, this work was able to provide an initial analysis of absorbed dose estimates for a homogeneous set of HCC patients and is unique in combining post-therapeutic absorbed dose estimation based on scaled $^{99\text{m}}\text{Tc}/^{90}\text{Y}$ SPECT/CT, ^{90}Y BRS SPECT/CT and ^{90}Y PET/CT in the same patient. The accompanying phantom studies further support our results, and enable comprehensible conclusions. Nevertheless, it is highly desirable to pursue this investigation with larger patient cohorts and to possibly further include other liver tumors than HCC.

5. Conclusion

For the post-therapeutic assessment of ^{90}Y SIRT dose estimates, the proposed scaled $^{99\text{m}}\text{Tc}/^{90}\text{Y}$ SPECT/CT dosimetric approach showed the potential to reliably provide tumor absorbed dose estimates when compared to absorbed dose estimates obtained from ^{90}Y PET/CT, for given equivalence of tumor uptake pattern of $^{99\text{m}}\text{Tc}$ -MAA and ^{90}Y microspheres on SPECT/CT images. If this requirement is fulfilled, scaled $^{99\text{m}}\text{Tc}/^{90}\text{Y}$ SPECT/CT SIRT dosimetry could be of particular benefit for retrospective analysis of therapy outcome based on absorbed dose estimates. This may help to further correlate absorbed dose estimates with overall survival and tumor response for ^{90}Y SIRT of existing patient data with no ^{90}Y PET/CT. Tumor absorbed dose estimates from ^{90}Y BRS SPECT/CT exhibited large dose underestimations when compared to ^{90}Y PET/CT. For healthy liver tissue, all three imaging methods provided comparable absorbed dose estimates. This initial comparison of post-therapeutic absorbed dose estimates in dependence of the imaging method based on ten SIRTs of patients suffering from HCC together with phantom measurements may support subsequent investigations with larger patient cohorts and multiple centers.

6. Declaration

6.1. Ethics approval and consent to participate

This study is based on retrospective and anonymised data, which was acquired for clinical dosimetry (Ethics Committee of LMU Munich).

6.2. Consent for publication

Not applicable.

6.3. Availability of data and material

Please contact author for data requests.

Funding

This work was partly funded by the German Research Foundation (DFG) within the Research Training Group GRK 2274, and partly supported by the funding program “Medizintechnik Bayern” of “Bayerisches Ministerium für Wirtschaft” for the DosePlan project, MED-1703–0005.

8. Authors' contributions

JB, AG, LK, MS, JR, JZ, PB, SZ, HI, AT and GB designed the concept of the study. JB, AG, AT and HI reviewed the clinical data for dosimetry. JB, AG, AT, HI and GB carried out all data analysis. All authors contributed to the drafting of the manuscript, and all authors read and approved the manuscript.

Declaration of Competing Interest

The authors declare that they have no known competing financial interests or personal relationships that could have appeared to influence the work reported in this paper.

Acknowledgements

Not applicable.

References

- [1] Braat AJ, Smits ML, Braat MN, van den Hoven AF, Prince JF, de Jong HW, et al. (0)Y Hepatic Radioembolization: An Update on Current Practice and Recent Developments. *J Nucl Med.* 2015;56(7):1079–87.
- [2] Kennedy A, Nag S, Salem R, Murthy R, McEwan AJ, Nutting C, et al. Recommendations for radioembolization of hepatic malignancies using yttrium-90 microsphere brachytherapy: a consensus panel report from the radioembolization brachytherapy oncology consortium. *Int J Radiat Oncol Biol Phys.* 2007;68(1):13–23.
- [3] Gleisner KS, Spezi E, Solny P, Gabina PM, Cicone F, Stokke C, et al. Variations in the practice of molecular radiotherapy and implementation of dosimetry: results from a European survey. *EJNMMI physics.* 2017;4(1):28.
- [4] European Commission. Council Directive 2013/59/Euratom of 5 December 2013 laying down basic safety standards for protection against the dangers arising from exposure to ionising radiation, and repealing Directives 89/618/Euratom, 90/641/Euratom, 96/29/Euratom, 97/43/Euratom and 2003/122/Euratom. *Official Journal of the European Union.* 2014.
- [5] Dezarn WA, Cessna JT, DeWerd LA, Feng W, Gates VL, Halama J, et al. Recommendations of the American Association of Physicists in Medicine on dosimetry, imaging, and quality assurance procedures for ^{90}Y microsphere brachytherapy in the treatment of hepatic malignancies. 2011;38(8):4824–45.
- [6] Levillain H, Derijkere ID, Marin G, Guiot T, Vouche M, Reynaert N, et al. ^{90}Y -PET/CT-based dosimetry after selective internal radiation therapy predicts outcome in patients with liver metastases from colorectal cancer. 2018;8(1):60.
- [7] O'Doherty JJ. A review of 3D image-based dosimetry, technical considerations and emerging perspectives in ^{90}Y microsphere therapy. 2015;2(2):1.
- [8] Selwyn RG, Nickles RJ, Thomadsen BR, DeWerd LA, Micka JA. A new internal pair production branching ratio of ^{90}Y : the development of a non-destructive assay for ^{90}Y and ^{90}Sr . *Appl Radiat Isot.* 2007;65(3):318–27.
- [9] Lhomme R, van Elmbt L, Goffette P, Van den Eynde M, Jamar F, Pauwels S, et al. Feasibility of ^{90}Y TOF PET-based dosimetry in liver metastasis therapy using SIR-Spheres. *Eur J Nucl Med Mol Imaging.* 2010;37(9):1654–62.
- [10] Willowson KP, Tapner M, Team QL, Bailey DL. A multicentre comparison of quantitative ^{90}Y PET/CT for dosimetric purposes after radioembolization with resin microspheres: The QUEST Phantom Study. *Eur J Nucl Med Mol Imaging.* 2015;42(8):1202–22.
- [11] Rong X, Du Y, Ljungberg M, Rault E, Vandenbergh S, Frey EC. Development and evaluation of an improved quantitative ^{90}Y bremsstrahlung SPECT method. *Med Phys.* 2012;39(5):2346–58.
- [12] Elschot M, Lam MG, van den Bosch MA, Viergever MA, de Jong HW. Quantitative Monte Carlo-based ^{90}Y SPECT reconstruction. *J Nucl Med.* 2013;54(9):1557–63.
- [13] Yue J, Mauxion T, Reyes DK, Lodge MA, Hobbs RF, Rong X, et al. Comparison of quantitative Y-90 SPECT and non-time-of-flight PET imaging in post-therapy radioembolization of liver cancer. *Med Phys.* 2016;43(10):5779.
- [14] Elschot M, Vermolen BJ, Lam MG, de Keizer B, van den Bosch MA, de Jong HW. Quantitative comparison of PET and Bremsstrahlung SPECT for imaging the in vivo yttrium-90 microsphere distribution after liver radioembolization. *PLoS ONE* 2013; 8(2):e55742.
- [15] Kim SP, Cohalan C, Koepke N, Enger SA. A guide to ^{90}Y radioembolization and its dosimetry. *Physica Med* 2019;68:132–45.
- [16] Ho S, Lau WY, Leung TW, Chan M, Ngar YK, Johnson PJ, et al. Partition model for estimating radiation doses from yttrium-90 microspheres in treating hepatic tumours. *Eur J Nucl Med.* 1996;23(8):947–52.
- [17] Kao YH, Tan EH, Ng CE, Goh SW. Clinical implications of the body surface area method versus partition model dosimetry for yttrium-90 radioembolization using resin microspheres: a technical review. *Ann Nucl Med.* 2011;25(7):455–61.
- [18] Kao YH, Hock Tan AE, Burgmans MC, Irani FG, Khoo LS, Gong Lo RH, et al. Image-guided personalized dosimetry by artery-specific SPECT/CT partition modeling for safe and effective ^{90}Y radioembolization. *J Nucl Med.* 2012;53(4):559–66.
- [19] S.A. Gulec G. Mesoloras Stabin MJ. Dosimetric techniques in ^{90}Y -microsphere therapy of liver cancer: the MIRD equations for dose calculations. 2006;47(7):1209.
- [20] Flamen P, Vanderlinden B, Delatte P, Ghanem G, Amey L, Van Den Eynde M, et al. Multimodality imaging can predict the metabolic response of unresectable colorectal liver metastases to radioembolization therapy with Yttrium-90 labeled resin microspheres. *Phys Med Biol.* 2008;53(22):6591–603.
- [21] Snyder W, Ford M, Warner G, Watson S. MIRD pamphlet no. 11. The Society of Nuclear Medicine, New York. 1975:92-3.

- [22] Sarfaraz M, Kennedy AS, Lodge MA, Li XA, Wu X, Yu CX. Radiation absorbed dose distribution in a patient treated with yttrium-90 microspheres for hepatocellular carcinoma. *Med Phys*. 2004;31(9):2449–53.
- [23] Dieudonne A, Garin E, Laffont S, Rolland Y, Lebtahi R, Leguludec D, et al. Clinical feasibility of fast 3-dimensional dosimetry of the liver for treatment planning of hepatocellular carcinoma with 90Y-microspheres. *J Nucl Med*. 2011;52(12):1930–7.
- [24] Kennedy A, Dezarn W, Weiss AJJNMRT. Patient specific 3D image-based radiation dose estimates for 90Y microsphere hepatic radioembolization in metastatic tumors. 2011;2(111):1-8.
- [25] Ulrich G, Dudeck O, Furth C, Ruf J, Grosser OS, Adolf D, et al. Predictive value of intratumoral 99mTc-macroaggregated albumin uptake in patients with colorectal liver metastases scheduled for radioembolization with 90Y-microspheres. *J Nucl Med*. 2013;54(4):516–22.
- [26] Wondergem M, Smits ML, Elschot M, de Jong HW, Verkooijen HM, van den Bosch MA, et al. 99mTc-macroaggregated albumin poorly predicts the intrahepatic distribution of 90Y resin microspheres in hepatic radioembolization. *J Nucl Med*. 2013;54(8):1294–301.
- [27] Knesaurek K, Machac J, Muzinic M, DaCosta M, Zhang Z, Heiba SJTicr, et al. Quantitative comparison of yttrium-90 (90 Y)-microspheres and technetium-99m (99m Tc)-macroaggregated albumin SPECT images for planning 90 Y therapy of liver cancer. 2010;9(3):253-61.
- [28] Mikell JK, Mahvash A, Siman W, Mourtada F, Kappadath SC. Comparing voxel-based absorbed dosimetry methods in tumors, liver, lung, and at the liver-lung interface for (90)Y microsphere selective internal radiation therapy. *EJNMMI Phys*. 2015;2(1):16.
- [29] Fourkal E, Veltchev I, Lin M, Koren S, Meyer J, Doss M, et al. 3D inpatient dose reconstruction from the PET-CT imaging of 90Y microspheres for metastatic cancer to the liver: feasibility study. *Med Phys*. 2013;40(8):081702.
- [30] Pasciak AS, Bourgeois AC, Bradley YC. A Comparison of Techniques for (90)Y PET/CT Image-Based Dosimetry Following Radioembolization with Resin Microspheres. *Front Oncol*. 2014;4:121.
- [31] Lassmann M, Preylowski V, Schlögl S, Schoenahl F, Jörg G, Samnick S, et al. Is the Image Quality of I-124-PET Impaired by an Automatic Correction of Prompt Gammas? 2013.
- [32] Delker A, Fendler WP, Kratochwil C, Brunegraf A, Gosewisch A, Gildehaus FJ, et al. Dosimetry for 177 Lu-DKFZ-PSMA-617: a new radiopharmaceutical for the treatment of metastatic prostate cancer. *Eur J Nucl Med Mol Imaging* 2016;43(1):42–51.
- [33] Siman W, Mikell J, Kappadath S. Practical reconstruction protocol for quantitative 90Y bremsstrahlung SPECT/CT. *Med Phys* 2016;43(9):5093–103.
- [34] Balagopal A, Kappadath SCJMp. Characterization of 90Y-SPECT/CT self-calibration approaches on the quantification of voxel-level absorbed doses following 90Y-microsphere selective internal radiation therapy. 2018;45(2):875-83.
- [35] Kafrouni M, Allimant C, Fourcade M, Vauclin S, Guiù B, Mariano-Goulart D, et al. Analysis of differences between 99m Tc-MAA SPECT-and 90 Y-microsphere PET-based dosimetry for hepatocellular carcinoma selective internal radiation therapy. 2019;9(1):62.
- [36] Forwood N, Willowson KP, Tapner M, Bailey DL. Assessment of the relative contribution of volume and concentration changes in Yttrium-90 labeled resin microspheres on ionization chamber measurements. *Australas Phys Eng Sci Med* 2017;40(4):943–8.
- [37] Kossert K, Bokeloh K, Ehlers M, Nähle O, Scheibe O, Schwarz U, et al. Comparison of 90Y activity measurements in nuclear medicine in Germany. 2016;109:247-9.
- [38] Carlier T, Willowson KP, Fourkal E, Bailey DL, Doss M, Conti MJMp. 90Y-PET imaging: Exploring limitations and accuracy under conditions of low counts and high random fraction. 2015;42(7):4295-309.
- [39] Kafrouni M, Allimant C, Fourcade M, Vauclin S, Delicque J, Ilonca A-D, et al. Retrospective voxel-based dosimetry for assessing the ability of the body-surface-area model to predict delivered dose and radioembolization outcome. *J Nucl Med* 2018;59(8):1289–95.
- [40] Gallio E, Richetta E, Finessi M, Stasi M, Pellerito RE, Bisi G, et al. Calculation of tumour and normal tissue biological effective dose in 90Y liver radioembolization with different dosimetric methods. *Physica Med* 2016;32(12):1738–44.
- [41] Botta F, Mairani A, Battistoni G, Cremonesi M, Di Dia A, Fasso A, et al. Calculation of electron and isotopes dose point kernels with FLUKA Monte Carlo code for dosimetry in nuclear medicine therapy. *Med Phys*. 2011;38(7):3944–54.
- [42] Bland JM, Altman D. Statistical methods for assessing agreement between two methods of clinical measurement. *The Lancet*. 1986;327(8476):307–10.
- [43] Gnesin S, Canetti L, Adib S, Cherbuin N, Silva Monteiro M, Bize P, et al. Partition Model-Based 99mTc-MAA SPECT/CT Predictive Dosimetry Compared with 90Y TOF PET/CT Posttreatment Dosimetry in Radioembolization of Hepatocellular Carcinoma: A Quantitative Agreement Comparison. *J Nucl Med*. 2016;57(11):1672–8.
- [44] Jadoul A, Bernard C, Lovinfosse P, Gérard L, Lilet H, Cornet O, et al. Comparative dosimetry between 99m Tc-MAA SPECT/CT and 90 Y PET/CT in primary and metastatic liver tumors. 2019:1-10.
- [45] Richetta E, Pasquino M, Poli M, Cutaià C, Valero C, Tabone M, et al. PET-CT post therapy dosimetry in radioembolization with resin 90Y microspheres: Comparison with pre-treatment SPECT-CT 99mTc-MAA results. *Physica Med* 2019;64:16–23.
- [46] Rong X, Du Y, Frey EC. A method for energy window optimization for quantitative tasks that includes the effects of model-mismatch on bias: application to Y-90 bremsstrahlung SPECT imaging. *Phys Med Biol*. 2012;57(12):3711–25.
- [47] Rong X, Frey EC. A collimator optimization method for quantitative imaging: application to Y-90 bremsstrahlung SPECT. *Med Phys*. 2013;40(8):082504.
- [48] Uribe CF, Esquinas PL, Gonzalez M, Celler A. Characteristics of Bremsstrahlung emissions of (177)Lu, (188)Re, and (90)Y for SPECT/CT quantification in radionuclide therapy. *Phys Med*. 2016;32(5):691–700.
- [49] Pacilio M, Ferrari M, Chiesa C, Lorenzon L, Mira M, Botta F, et al. Impact of SPECT corrections on 3D-dosimetry for liver transarterial radioembolization using the patient relative calibration methodology. *Med Phys*. 2016;43(7):4053.
- [50] D'Arienzo M, Chiaramida P, Chiacchiararelli L, Coniglio A, Cianni R, Salvatori R, et al. 90Y PET-based dosimetry after selective internal radiotherapy treatments. *Nucl Med Commun*. 2012;33(6):633–40.
- [51] D'Arienzo M, Filippi L, Chiaramida P, Chiacchiararelli L, Cianni R, Salvatori R, et al. Absorbed dose to lesion and clinical outcome after liver radioembolization with 90Y microspheres: a case report of PET-based dosimetry. *Ann Nucl Med*. 2013;27(7):676–80.
- [52] Gates VL, Esmail AA, Marshall K, Spies S, Salem R. Internal pair production of 90Y permits hepatic localization of microspheres using routine PET: proof of concept. *J Nucl Med*. 2011;52(1):72–6.
- [53] Kao Y-H, Steinberg JD, Tay Y-S, Lim GK, Yan J, Townsend DW, et al. Post-radioembolization yttrium-90 PET/CT-part 1: diagnostic reporting. *EJNMMI research*. 2013;3(1):56.
- [54] Ilhan H, Goritschan A, Paprottka P, Jakobs TF, Fendler WP, Bartenstein P, et al. Systematic evaluation of tumoral 99mTc-MAA uptake using SPECT and SPECT/CT in 502 patients before 90Y radioembolization. *J Nucl Med*. 2015;56(3):333–8.
- [55] Chiesa C, Mira M, Maccauro M, Romito R, Spreafico C, Sposito C, et al. A dosimetric treatment planning strategy in radioembolization of hepatocarcinoma with 90Y glass microspheres. *Q J Nucl Med Mol Imaging*. 2012;56(6):503–8.
- [56] Chiesa C, Mira M, Maccauro M, Spreafico C, Romito R, Morosi C, et al. Radioembolization of hepatocarcinoma with (90)Y glass microspheres: development of an individualized treatment planning strategy based on dosimetry and radiobiology. *Eur J Nucl Med Mol Imaging*. 2015;42(11):1718–38.
- [57] Chiesa C, Lambert B, Maccauro M, Ezziddin S, Ahmadzadehfar H, Dieudonne A, et al. Pretreatment Dosimetry in HCC Radioembolization with (90)Y Glass Microspheres Cannot Be Invalidated with a Bare Visual Evaluation of (99m)Tc-MAA Uptake of Colorectal Metastases Treated with Resin Microspheres. *J Nucl Med*. 2014;55(7):1215–6.
- [58] Garin E, Lenoir L, Rolland Y, Edeline J, Mesbah H, Laffont S, et al. Dosimetry based on 99mTc-macroaggregated albumin SPECT/CT accurately predicts tumor response and survival in hepatocellular carcinoma patients treated with 90Y-loaded glass microspheres: preliminary results. *J Nucl Med*. 2012;53(2):255–63.
- [59] Maughan NM, Garcia-Ramirez J, Arpidone M, Swallen A, Laforest R, Goddu SM, et al. Validation of post-treatment PET-based dosimetry software for hepatic radioembolization of Yttrium-90 microspheres. *Med Phys* 2019;46(5):2394–402.

Chapter 8

Publication II

ORIGINAL RESEARCH

Open Access



Influence of dosimetry method on bone lesion absorbed dose estimates in PSMA therapy: application to mCRPC patients receiving Lu-177-PSMA-I&T

Julia Brosch-Lenz^{1*} , Carlos Uribe^{2,3}, Astrid Gosewisch¹, Lena Kaiser¹, Andrei Todica¹, Harun Ilhan¹, Franz Josef Gildehaus¹, Peter Bartenstein¹, Arman Rahmim^{2,3,4}, Anna Celler³, Sibylle Ziegler¹ and Guido Böning¹

* Correspondence: Julia.Brosch-Lenz@med.uni-muenchen.de

¹Department of Nuclear Medicine, University Hospital, LMU Munich, Marchioninistrasse 15, 81377 Munich, Germany

Full list of author information is available at the end of the article

Abstract

Background: Patients with metastatic, castration-resistant prostate cancer (mCRPC) present with an increased tumor burden in the skeleton. For these patients, Lutetium-177 (Lu-177) radioligand therapy targeting the prostate-specific membrane antigen (PSMA) has gained increasing interest with promising outcome data. Patient-individualized dosimetry enables improvement of therapy success with the aim of minimizing absorbed dose to organs at risk while maximizing absorbed dose to tumors. Different dosimetric approaches with varying complexity and accuracy exist for this purpose. The Medical Internal Radiation Dose (MIRD) formalism applied to tumors assumes a homogeneous activity distribution in a sphere with unit density for derivation of tumor S values (TSV). Voxel S value (VSV) approaches can account for heterogeneous activities but are simulated for a specific tissue. Full patient-individual Monte Carlo (MC) absorbed dose simulation addresses both, heterogeneous activity and density distributions. Subsequent CT-based density weighting has the potential to overcome the assumption of homogeneous density in the MIRD formalism with TSV and VSV methods, which could be a major limitation for the application in bone metastases with heterogeneous density. The aim of this investigation is a comparison of these methods for bone lesion dosimetry in mCRPC patients receiving Lu-177-PSMA therapy.

Results: In total, 289 bone lesions in 15 mCRPC patients were analyzed. Percentage difference (PD) of average absorbed dose per lesion compared to MC, averaged over all lesions, was $+14 \pm 10\%$ (min: -21% ; max: $+56\%$) for TSVs. With lesion-individual density weighting using Hounsfield Unit (HU)-to-density conversion on the patient's CT image, PD was reduced to $-8 \pm 1\%$ (min: -10% ; max: -3%). PD on a voxel level for three-dimensional (3D) voxel-wise dosimetry methods, averaged per lesion, revealed large PDs of $+18 \pm 11\%$ (min: -27% ; max: $+58\%$) for a soft tissue VSV approach compared to MC; after voxel-wise density correction, this was reduced to $-5 \pm 1\%$ (min: -12% ; max: -2%).

(Continued on next page)

(Continued from previous page)

Conclusion: Patient-individual MC absorbed dose simulation is capable to account for heterogeneous densities in bone lesions. Since the computational effort prevents its routine clinical application, TSV or VSV dosimetry approaches are used. This study showed the necessity of lesion-individual density weighting for TSV or VSV in Lu-177-PSMA therapy bone lesion dosimetry.

Keywords: Radioligand therapy, mCRPC, PSMA, Lutetium-177, 3D dosimetry, Tumor dosimetry, OLINDA/EXM[®], Voxel S value, Monte Carlo simulation

Background

The incidence of prostate cancer has been steadily increasing over the past decades in western populations [1, 2]. Patients with castration-resistant prostate cancer (mCRPC) typically present a large metastatic tumor burden in the bones [3]. Radioligand therapies (RLT) targeting the prostate-specific membrane antigen (PSMA) such as Lutetium-177-PSMA (Lu-177-PSMA) and Actinium-225-PSMA have shown promising results in patients ineligible for other therapies or have shown progress after receiving other systemic treatment options [4]. The clinical value of personalized dosimetry in RLT lies in a possible increase of the therapeutic window by limiting absorbed dose to organs at risk while maximizing absorbed dose to tumors. Thus, personalized dosimetry is indispensable for correlation with therapy response and patient outcome, enabling adjustments for subsequent therapy cycles. The first Lu-177-DKFZ-PSMA-617 absorbed dose estimates were published in 2015 [5]. Nonetheless, up to now, there are still few publications addressing the absorbed doses delivered to tumors after Lu-177-PSMA therapy [5–11]. While there is a clear definition of absorbed dose D as “the quotient of $d\bar{\epsilon}$ by dm , where $d\bar{\epsilon}$ is the mean energy imparted by ionizing radiation to matter of mass dm ” in Report 85 of the International Commission on Radiation Units and Measurements (ICRU) [12], there are, however, different approaches for estimation of absorbed dose for internal radionuclide therapies, each with varying complexity and accuracy.

The use of pre-calculated organ-specific S values according to the Medical Internal Radiation Dose (MIRD) Committee formalism [13] has become more prevalent using the OLINDA/EXM[®] 2.0 software (HERMES Medical Solutions, Sweden) [14]. However, for the particular situation of tumor absorbed dose estimation, this approach relies on the unit density sphere model for calculation of tumor S values (TSV) that assumes homogeneous activity distribution within the spherical tumor and a tumor density of 1 g/cm^3 (i.e., soft tissue). Thus, this fast and simple approach has limited applicability to bone lesions with higher densities and non-uniform activity distributions. Mass scaling of TSVs has been applied to include patient-specific density variations [15, 16], though the lesion-individual density in mCRPC patients may still limit the value of mass scaling of TSV. A three-dimensional (3D) voxel-wise dosimetry approach includes radionuclide-specific absorbed dose kernels or voxel S values (VSVs), which are pre-simulated for a specific tissue type and voxel size [17]. The use of VSVs accounts for heterogeneous activity distributions under the assumption of a homogeneous material and density [17]. Monte Carlo (MC) absorbed dose simulations based on SPECT/CT data include patient-individual, heterogeneous density, and activity distributions, yielding 3D voxel-wise absorbed dose estimations.

The aim of this work is to investigate various dosimetry techniques for accurate bone lesion absorbed dose estimation in Lu-177-PSMA therapy of mCRPC. The unit density sphere model for TSVs for volume of interest (VOI)-based dosimetry, and VSVs for different tissue types for 3D voxel-based dosimetry, without and with a tissue-specific density weighting were compared to patient-individual dosimetry by Monte Carlo simulations.

Methods

Patients

The study was conducted retrospectively on anonymized data and was approved by the local ethics committee of our institution. Fifteen patients with metastatic, castration-resistant prostate cancer (mCRPC) and pronounced metastases in the skeleton were included in this study. Table 1 presents the detailed patient characteristics. Patients received a first cycle of radioligand therapy using Lu-177-PSMA-I&T with activities of 7.4 GBq (10 patients) and 9.0 GBq (5 patients). The higher initial therapy activities were used in case of severe burden of bone metastases and/or presence of visceral metastases.

Image acquisition and reconstruction

Following the standard clinical routine imaging protocol of our institution, patients underwent quantitative Lu-177 SPECT/CT imaging (Symbia IntevoTM T16 SPECT/CT, 3/8" crystal, medium-energy low-penetration collimator, Siemens Healthcare, Germany) at 24 h, 48 h, and 72 h post injection (p.i.). At least two SPECT bed positions were

Table 1 Summary of patients being included. Previous treatment (1: yes; 0: no): OP surgery, RTx radiotherapy, AHT anti-hormonal therapy (including second line AHT with bicalutamide, enzalutamide, abiraterone acetate), CTx chemotherapy (docetaxel, cabazitaxel), Ra-223 radium-223 dichloride

Patient	Age	Activity (GBq)	PSA (ng/ml) prior to therapy	Gleason score	Previous treatment				
					OP	RTx	AHT	CTx	Ra-223
1	61	7.44	25.9	9	0	1	1	1	0
2	75	7.46	38.4	9	1	0	1	1	0
3	75	7.44	1070	8	1	1	1	1	1
4	78	9.04	570	9	0	0	1	1	0
5	62	7.47	848	-	0	1	1	0	0
6	59	7.47	5.38	7b	0	1	1	1	0
7	74	9.19	1696	-	1	1	1	0	0
8	63	7.46	149	8	0	1	1	1	0
9	82	7.44	20.2	9	1	1	1	0	0
10	70	7.42	127	9	1	1	1	1	1
11	75	9.05	436	9	0	1	1	1	0
12	49	9.00	121	9	1	1	1	1	1
13	64	7.47	1268	8	0	1	1	1	0
14	79	7.46	72.7	7b	0	0	1	0	0
15	73	9.04	19.6	9	1	0	1	1	0

acquired in auto-contour mode followed by a low-dose CT. Image acquisition parameters included a 128×128 matrix with 64 angular steps and a duration of 5 s per step. These parameters were chosen as a compromise between covering the extended axial field of view (FOV) and patient comfort. The imaging energy window was centered at the energy of the upper photo peak of Lu-177 at 208 keV (width 15%). Quantitative SPECT reconstruction was performed with the clinically established Hermes Hybrid Recon v.2.1.1 reconstruction, which represents an ordered-subset ordinary-Poisson maximum a priori expectation maximization (OS-MAP-EM) reconstruction algorithm with a one-step late weighted quadratic penalty function and collimator-specific depth-dependent detector response modelling (16 MAP iterations, 8 subsets, Bayesian weight 0.01, HERMES Medical Solutions, Sweden) [18, 19]. CT-based attenuation correction and model-based scatter estimation as described by Sohlberg et al. [18] were used. The SPECT images were calibrated with a system-specific calibration factor, which was obtained using the same SPECT image acquisition and reconstruction parameters for a cylinder phantom (20 cm diameter), homogeneously filled with a known Lu-177 activity concentration [5, 20, 21].

Image processing

All images were processed with PMOD (v4.005; PMOD Technologies LLC). Rigid co-registration of all CT and SPECT volumes was performed onto the SPECT/CT image data at 24 h p.i., which served as reference. An individual bone map and a whole-body VOI were derived from the reference CT by threshold-based segmentation (Hounsfield Unit (HU) threshold of 200 for bone map [3], HU threshold -200 to -100 for the whole body), and kidney VOIs were defined by manual delineation. To further segment individual bone lesions within the skeletal bone map, the semi-automatic k-means cluster segmentation of PMOD 3D tool was used on the 24-h SPECT [3]. All VOIs were copied to the co-registered SPECT data sets. Since image artifacts and noise impact voxel-wise fitting, time-activity curves were fitted in pre-defined VOIs to determine VOI-wise effective half-lives. VOI activities for the kidneys, tumor lesions, and remainder of the body (whole-body minus the kidneys and tumor lesions) were fitted using a mono-exponential fit model. A hybrid VOI/voxel-wise approach was used for generation of time-integrated activity images to partially maintain the voxel-wise activity distribution information. The time-integrated activity images per patient were generated with MATLAB (R2019b, The MathWorks, Inc. Natick, MA) based on the reference SPECT at 24 h p.i. and the individual VOI map:

$$\tilde{A}^{voxel} = \frac{A_{t=0}^{voxel}}{\lambda_{VOI}} \quad (1)$$

where \tilde{A}^{voxel} denotes the time-integrated activity per voxel, $A_{t=0}^{voxel}$ is the activity at time point zero in a voxel, and $\lambda_{VOI} = \ln 2 / t_{1/2}$ uses the effective half-life obtained from mono-exponential fitting in the related VOI. $A_{t=0}^{voxel}$ was computed as:

$$A_{t=0}^{voxel} = A_t^{voxel} \cdot e^{\lambda_{VOI} \cdot t} \quad (2)$$

with the time t being the exact time point of the individual 24 h p.i. SPECT acquisition.

Dosimetry calculations

We investigated 7 different dosimetry approaches by utilizing the aforementioned time-integrated activity images and the reference CT of each patient.

MC method: Patient-specific Monte Carlo (MC) absorbed dose simulation

Patient-specific MC absorbed dose simulation accounts for the patient's anatomy by using the geometry and density information from the patient's CT image [22]. The radioactive decay, the interactions of the ionizing radiation with matter, and consequently the absorbed dose are simulated based on the patient-individual time-integrated activity distribution. Hence, MC absorbed dose simulations contain the highest level of complexity for modelling of radiation transport and interactions of ionizing radiation with matter with associated energy deposition among all other applied methods in this study. In concordance with inter alia Dieudonné et al. [23] and Grimes et al. [24], we considered MC dosimetry as the reference method assessing the other methods for bone lesion dosimetry. MC simulations in this study were performed using the GATE MC code version 8.2, based on GEANT4 version 10.5.1. This code has previously been validated for use in nuclear medicine therapies [25–27]. The radionuclide data were based on the Nuclear Data Sheets of Kondev et al. [28] and are the same as in OLINDA/EXM[®] [29]. A CT scan of a Gammex tissue characterization phantom (Gammex 467; Gammex Inc., Middleton, WI) using the same imaging parameters from the patient scans was performed, which confirmed the HU-to-density relationship of our CT device with that implemented in GATE. GATE converts HU-to-density values with internal tables based on Schneider et al. [22]. The time-integrated activity image of each patient was normalized with its total number of decays and used as the input for the simulations. The total number of 10^9 primary decays per patient simulation was divided into 20 sub-simulations for parallel execution on separate CPUs to increase simulation speed (dual CPU system with 2 INTEL XEON 4114 CPUs, 10 cores each, 2.2 GHz, 192 GB RAM, running on Linux). The relative statistical uncertainty in the absorbed dose per voxel was calculated as described by Chetty et al. [30]. The voxel size of the simulation was $(4.7952 \text{ mm})^3$ corresponding to the voxel sizes of the SPECT acquisitions. All particle range thresholds were set to 0.1 mm.

TSV method: Tumor S values (TSV) according to the unit density sphere model

The tumor S values from the uniform and unit density sphere model of OLINDA/EXM[®] 2.0 (HERMES Medical Solutions, Sweden) were used. This method represents the model with the lowest level of complexity and can be considered as the most simple and applicable method, yet clinically available. Since the total time-integrated activity per lesion and the lesion volume were known from the processing steps described above, the average lesion absorbed dose was calculated following the MIRD formalism [13] by multiplication of the tumor S value for the selected tumor volume with the tumor time-integrated activity. This approach is assuming that the lesion mass is comparable to the lesion volume at a tissue density of 1 g/cm^3 . TSVs are available for a

limited number of sphere volumes/masses. Hence, the TSV per lesion was obtained by fitting the available TSVs within OLINDA/EXM®, and subsequent calculation of the TSV for the lesion mass m with the fit parameters ($TSV(m) = 2.19 \cdot 10^{-5} \cdot m^{-0.99}$). This method includes solely the tumor self-dose [31] and is further based on the assumption that lesions were all of spherical shape with unit density and uniform activity distribution [32].

TSV_{weighted} method: TSV according to the unit density sphere model with additional lesion-individual density weighting

A simple method aiming to improve this absorbed dose estimate and to account for the tissue-specific tumor density is to convert the patient CT-image voxel-wise to densities using the HU-to-density conversion table, followed by the extraction of average lesion-individual density using the lesion VOI. The absorbed dose estimate is subsequently adjusted by weighting the lesion absorbed dose value D^{lesion} with the ratio of unit density and the average lesion-individual density $\bar{\rho}_{lesion}$, being equivalent to the mass scaling of S values [16]. This method takes into account the actual average lesion density $\bar{\rho}_{lesion}$ rather than assuming a fixed density for all lesions.

$$D_{weighted}^{lesion} = D^{lesion} \cdot \frac{1 \text{ g/cm}^3}{\bar{\rho}_{lesion}}. \quad (3)$$

VSV^{soft} method: Absorbed dose convolution model using voxel S values (VSVs) based on International Commission On Radiological Protection (ICRP) soft tissue

To account for the non-uniform activity distribution in 3D voxel-wise dosimetry, the use of VSVs for dosimetry has gained increasing interest [17]. For this purpose, GATE MC code was used for the simulation of Lu-177 VSVs using the voxel size of the time-integrated activity images, namely $(4.7952 \text{ mm})^3$. The simulation used the soft tissue composition according to the ICRP [33, 34]. The central voxel of the ICRP soft tissue medium in a $51 \times 51 \times 51$ matrix was set as Lu-177 source voxel, and 10^8 primaries were simulated. The VSVs represent the absorbed dose distribution per decay such that when convolved with the time-integrated activity image this results in a patient-specific 3D voxel-wise absorbed dose map.

VSV_{weighted}^{soft} method: Absorbed dose convolution model using VSVs based on ICRP soft tissue with additional density weighting

A limitation of the VSV^{soft} method was that the VSVs were simulated exclusively for soft tissue, and hence, the applicability for bone lesion dosimetry is hindered. Similar to the density weighting presented in the TSV_{weighted} method, it is possible to adjust for the different densities of the patient-individual anatomy and the density of the simulated VSVs. For this, the HUs of the patients' CT were voxel-wise converted into density values. Consequently, the 3D voxel-wise absorbed dose map from the VSV^{soft} method is voxel-wise weighted with the ratio of the VSV density of ICRP soft tissue ρ_{ICRP} to the actual voxel density ρ_{voxel} [23]:

$$D_{weighted}^{voxel} = D^{voxel} \cdot \frac{\rho_{ICRP}}{\rho_{voxel}} \tag{4}$$

VSV^{soft+bone} method: Absorbed dose convolution model using VSVs based on ICRP soft tissue and VSVs based on ICRP cortical bone

We extended the VSV^{soft} method by simulation of cortical bone VSVs using a standard ICRP cortical bone composition [33, 34] with the same simulation setup as for the ICRP soft tissue VSVs in the VSV^{soft} method. Similar to Lee et al. [35] who used multiple VSVs for regions with different tissues and densities, the combination of VSV^{soft} and VSV^{bone} was tested. For this, the patient’s bone map was used to distinguish between regions containing bone or soft tissue. The corresponding tissue-specific VSVs were applied in their respective regions. Subsequently, to obtain a total 3D voxel-wise absorbed dose map, the soft tissue 3D voxel-wise absorbed dose map (in soft tissue regions) and the cortical bone 3D voxel-wise absorbed dose map (in bone regions) are combined into a single image.

VSV^{soft+bone weighted} method: Absorbed dose convolution model using VSVs based on ICRP soft tissue and VSVs based on ICRP cortical bone with additional density weighting

The skeleton itself is not merely composed of the cortical bone and shows a heterogeneous composition of tissues with varying densities. Therefore, to further account for the variations in bone composition, beyond the above-mentioned standard cortical model, a similar voxel-wise density weighting as in Eq. (4) is applied to the combined 3D voxel-wise absorbed dose map obtained from the VSV^{soft+bone} method in order to correct for differences in density per voxel.

Comparisons

The TSV and TSV_{weighted} yield average lesion absorbed doses in agreement with the definition of average absorbed dose D^{av} in a chosen region of a specific tissue with total mass m_t as defined by Eq. 6.3 in the ICRU Report 86 [36]. To enable a comparison of this average absorbed dose per lesion D^{av} for the TSV approaches with the 3D MC voxel-wise absorbed dose maps, the average was formed accordingly, yielding D_{MC}^{av} . The percentage difference PD^{av} was calculated:

$$PD^{av} = \frac{D_{method}^{av} - D_{MC}^{av}}{D_{MC}^{av}} \cdot 100 \tag{7}$$

To evaluate the 3D voxel-wise absorbed dose maps obtained from MC, VSV^{soft}, VSV_{weighted}^{soft}, VSV^{soft+bone}, and VSV_{weighted}^{soft+bone}, the minimum absorbed dose within 25%, 50%, and 75% of the VOI volume per lesion was calculated, giving D25, D50, and D75.

For the assessment of the agreement of the different investigated 3D voxel-wise absorbed dose estimation methods, PD^{vox} was calculated on a voxel level for VSV^{soft}, VSV_{weighted}^{soft}, VSV^{soft+bone}, and VSV_{weighted}^{soft+bone} compared with MC:

$$PD^{vox} = \frac{D_{method}^{vox} - D_{MC}^{vox}}{D_{MC}^{vox}} \cdot 100 \tag{9}$$

Bland-Altman plots [37, 38] were used to compare the absorbed dose estimation methods.

Results

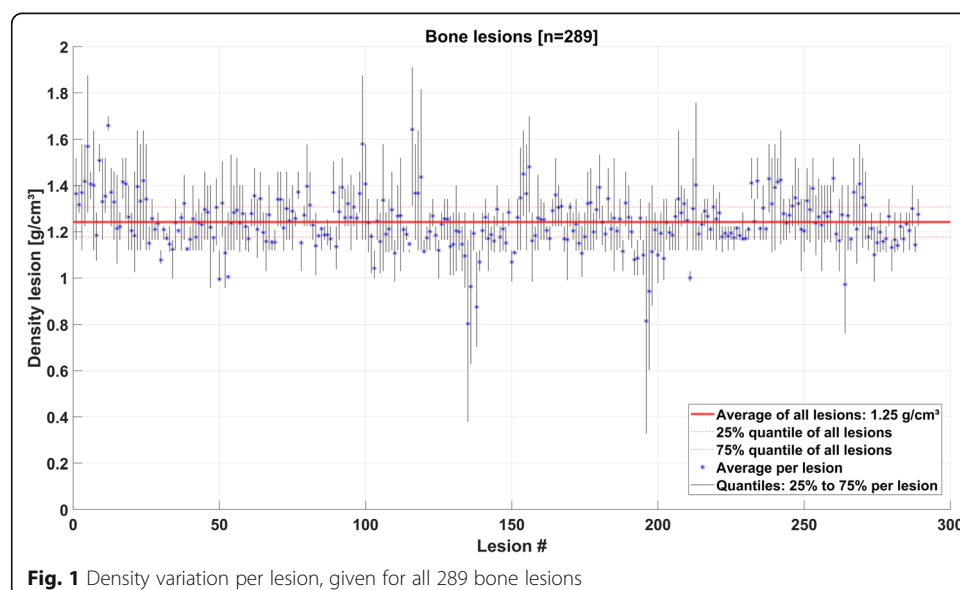
In total, 289 bone lesions in the 15 mCRPC patients were evaluated. The segmented lesion volumes were on average 19.1 ml (range: 1.1 to 453.2 ml). The bone lesions were distributed within the whole skeleton. The majority of lesions were situated in the vertebrae (106), followed by the ribs (68), the extremities (64), and the pelvis (51). The average lesion density was $1.25 \pm 0.11 \text{ g/cm}^3$ (min: 0.80 g/cm^3 ; max: 1.66 g/cm^3), averaged over all 289 bone lesions. The density variation within each bone lesion is displayed for all lesions in Fig. 1.

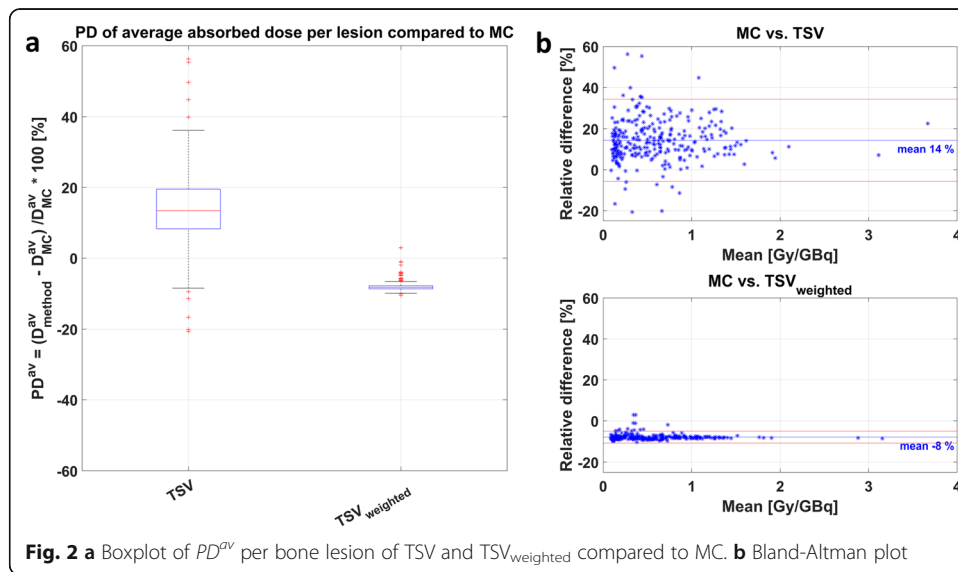
MC simulations

The overall simulation time per patient for the MC method was less than 4.5 h. The maximum relative statistical uncertainty in absorbed dose simulations was below 2.4 % for all voxels in all lesions and below 0.9 % on average over all lesion voxels. The maximum statistical uncertainty in the absorbed dose for the target region of ICRP soft tissue and ICRP cortical bone VSVs of the VSV^{soft} , $VSV_{\text{weighted}}^{\text{soft}}$, $VSV^{\text{soft+bone}}$, and $VSV_{\text{weighted}}^{\text{soft+bone}}$ methods was below 3.2%. This was for the most distant voxel from the source voxel. The average over all target voxels was below 2.0%.

Comparison of dosimetry methods

The percentage difference PD^{av} of average lesion absorbed dose estimates for the unaltered TSV was $+14 \pm 10\%$ (min: -21% ; max: $+56\%$) compared to MC, averaged over all lesions. The lesion-individual density weighting reduced the PD^{av} of TSV_{weighted} to $-8 \pm 1\%$ (min: -10% ; max: -3%). Figure 2a illustrates the decrease in range of PD^{av} for TSV_{weighted} compared to TSV, further supported by the Bland-Altman plot in Fig. 2b, showing the mean value of both methods compared to their relative difference.





The percentage difference (PD) of D25, D50, and D75 of VSV^{soft} , $VSV^{soft}_{weighted}$, $VSV^{soft+bone}$, and $VSV^{soft+bone}_{weighted}$ methods compared to MC are given in Table 2, averaged over all lesions. The density weighting of VSV reduced the PD compared to the unweighted methods. The smallest PD of - 2% for D25, D50, and D75 was found for $VSV^{soft+bone}_{weighted}$. The evaluation on a voxel level revealed PD^{vox} of $+ 18 \pm 11\%$ (min: - 27%; max: + 58%) for VSV^{soft} , averaged per VOI and over all lesions. This was reduced to $- 5 \pm 1\%$ (min: - 12 %; max: - 2%) after voxel-wise density weighting for $VSV^{soft}_{weighted}$. $VSV^{soft+bone}$ showed PD^{vox} of $- 34 \pm 6\%$ (min: - 60%; max: + 5%). $VSV^{soft+bone}_{weighted}$ showed the smallest PD^{vox} of $- 2 \pm 1\%$ (min: - 9%; max: 0%). These observations are summarized in Fig. 3. The additional density weighting of $VSV^{soft}_{weighted}$, and $VSV^{soft+bone}_{weighted}$, led to an overall smaller range of percentage differences than the associated method without weighting.

Figure 4 shows low bias for D50 compared to MC for the bone lesion absorbed dose estimates achieved with the density weighted $VSV^{soft}_{weighted}$ (Fig. 4c) and $VSV^{soft+bone}_{weighted}$ (Fig. 4d). Furthermore, their corresponding limits of agreement and mean relative difference were the smallest with fewest outliers of all investigated 3D voxel-wise dosimetry methods. The Bland-Altman plots in Fig. 4a and b demonstrate the larger variations in lesion absorbed doses of the unweighted dosimetry methods compared to MC dosimetry.

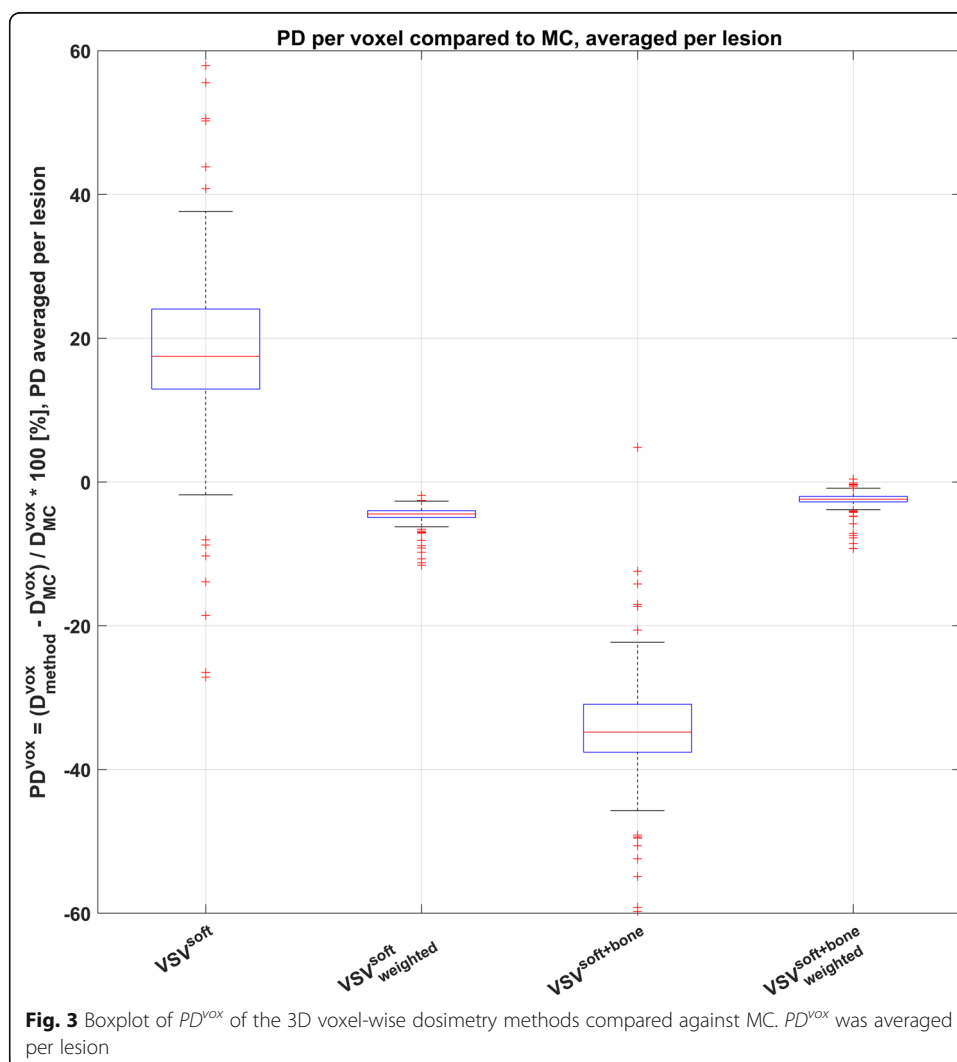
Figure 5 visualizes a patient example showing the same transversal slice of 3D voxel absorbed dose maps from the 3D voxel-wise dosimetry methods fused with the corresponding slice of the patient's CT (Fig. 5a). The 3D absorbed dose maps for the displayed bone lesion obtained from MC (Fig. 5b), $VSV^{soft}_{weighted}$ (Fig. 5d), and $VSV^{soft+bone}_{weighted}$ (Fig. 5f) are comparable. The 3D absorbed dose map of VSV^{soft} (Fig. 5c) generally overestimates and $VSV^{soft+bone}$ (Fig. 5e) underestimates the 3D absorbed dose map obtained from MC (Fig. 5b).

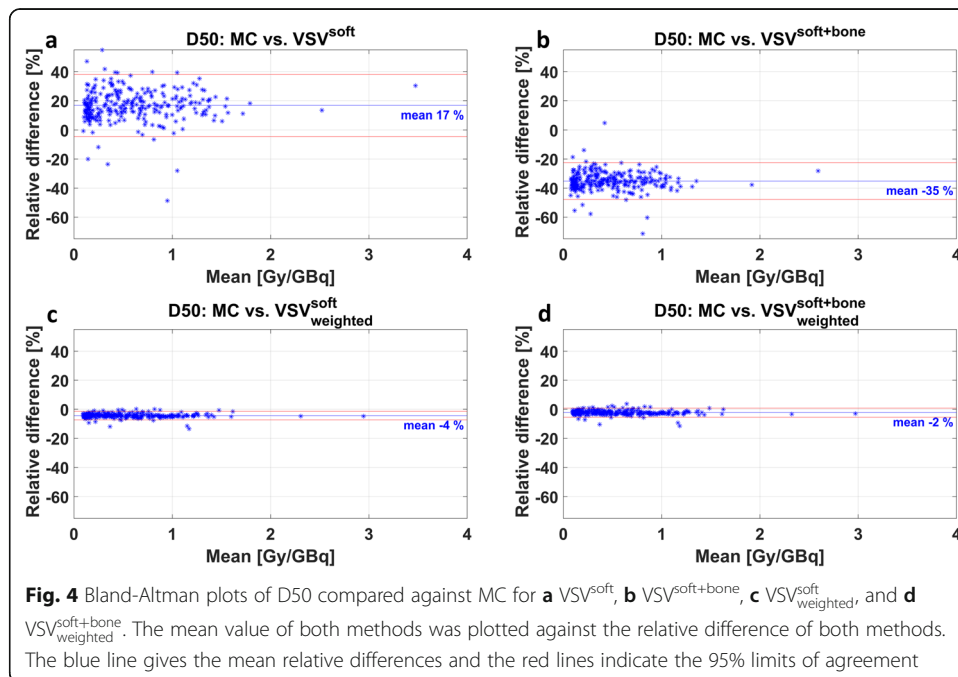
Table 2 PD in minimum absorbed doses to 25%, 50%, and 75% (D25, D50, D75) of the lesion VOI volume compared against MC. The PD was formed per lesion and then averaged over all lesion giving the presented value

Method	VSV ^{soft} Mean ± SD	VSV ^{soft} _{weighted} Mean ± SD	VSV ^{soft+bone} Mean ± SD	VSV ^{soft+bone} _{weighted} Mean ± SD
PD of D25 [%]	15 ± 14	- 4 ± 2	- 36 ± 8	- 2 ± 2
PD of D50 [%]	17 ± 11	- 4 ± 2	- 35 ± 6	- 2 ± 2
PD of D75 [%]	18 ± 10	- 5 ± 1	- 34 ± 6	- 2 ± 1

Discussion

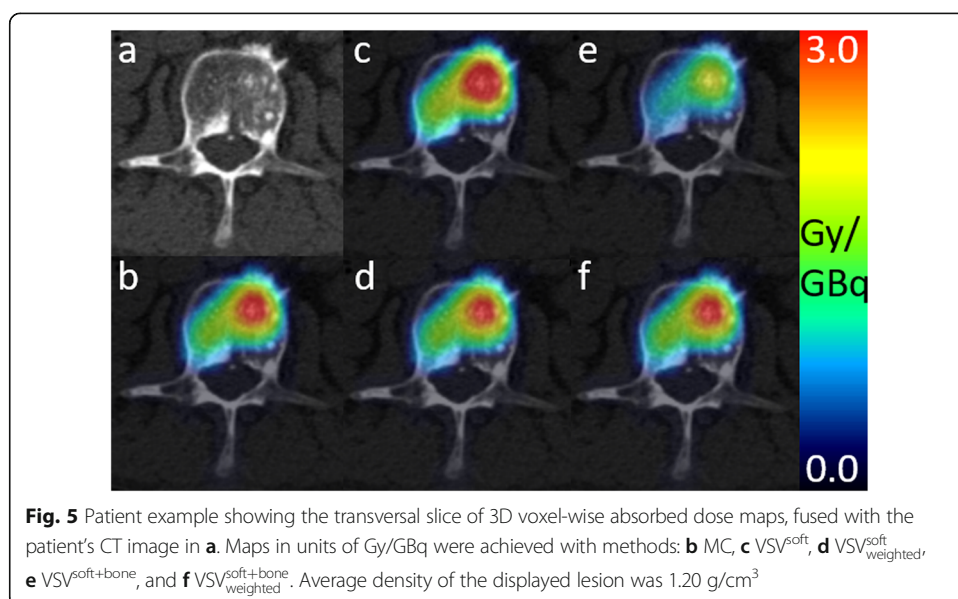
Patients with advanced mCRPC present with a considerably high tumor burden in the bone. Furthermore, osteosclerotic bone metastases can develop an increased number of osteoblasts leading to an elevated bone mass and increased density in the bone lesions [39]. Consequently, bone lesion absorbed dose estimates in Lu-177-PSMA therapy are affected by regional variations in bone tissue density, as observed in our investigations (Fig. 1). The absorbed dose estimates may depend on the strategy to account for these





local changes. In this study, different techniques for VOI-wise and 3D voxel-wise dosimetry with varying complexity were compared. Simplified methods were tested against absorbed dose estimation by full Monte Carlo simulation. For this purpose, dosimetry results of 289 bone lesions of 15 mCRPC patients receiving their first cycle of Lu-177-PSMA-I&T therapy were assessed. To our knowledge, this study is the first to analyze and compare different dosimetric approaches for absorbed dose estimation in a high number of bone lesions in Lu-177-PSMA therapy.

The first method was based on the application of OLINDA/EXM[®], which is widely clinically available and has been commonly used for dosimetry estimations in Lu-177-PSMA therapies [5–7, 9–11]. The percentage difference PD^{av} of average lesion



absorbed doses compared to the MC average absorbed dose D_{MC}^{av} ranged from an underestimation of -21% to an overestimation by $+56\%$, yielding an averaged overestimation of $+14 \pm 10\%$ in all lesions. The broad spread of relative differences can partly be explained by the different assumptions made within this approach, i.e., spherical shape, uniform activity distribution, and unit density of the tumor. The latter may have the greatest impact for bone lesions with increased density. Using the VOI-based method $TSV_{weighted}$, we hence attempted to correct for the different density of bone lesions compared to the unit density sphere model of TSVs by using the average lesion-individual density obtained from the patient's CT scan. The mass scaling of the TSV with the lesion-individual average density addresses this assumption, yielding a reduced PD^{av} compared to MC as highlighted in Fig. 2. The spread of the PD^{av} of average lesion absorbed dose estimates was reduced to -10 to -3% with an average absorbed dose underestimation of $-8 \pm 1\%$. This remaining difference may be associated to the assumptions that the tumor has only contributions of self-dose and is having a spherical shape in the TSV methods. Previous studies assessed the accuracy of absorbed dose estimation in soft tissue lesion against MC. Howard et al. [40] compared lesion absorbed dose estimates from the unit density sphere model of OLINDA/EXM[®] against MC simulation for Iodine-131 (I-131) radioimmunotherapy of lymphoma patients and concluded that the lesion shape has a minor impact when comparing the self-dose component. Their investigations revealed an absorbed dose underestimation compared to MC absorbed dose with a range of -2 to -31% PD, with average $-15 \pm 8\%$. Grimes et al. [24] found good agreement of neuroendocrine tumor absorbed doses for Lu-177 from the unit density sphere model of OLINDA/EXM[®] and MC simulations with average percentage differences of $-3.8\% \pm 5.2\%$. Similar results with differences of -5% were found by Divoli et al. [41], comparing absorbed doses of OLINDA/EXM[®] and MC for artificial spherical tumors in liver and lung. Our work assessed bone lesion absorbed dose estimation and the mass scaling of $TSV_{weighted}$ with lesion-individual average density as described herein revealed PD^{av} compared to MC in the range of those reported in the literature [24, 40–42]. Pacilio et al. [43] investigated absorbed dose estimates for bone metastases of patients receiving Radium-223 (Ra-223) dichloride therapy. This publication used a fixed density of 1.4 g/cm^3 for density weighting of the unit density sphere model of OLINDA/EXM[®]. If no lesion-individual density can be obtained using the patient CT image, this approach may result in more realistic values. However, the average lesion density for all 289 bone lesions investigated in this study was $1.25 \pm 0.11 \text{ g/cm}^3$, being lower than the proposed density of the skeleton of 1.4 g/cm^3 [44]. The inter-lesion density variation displayed in Fig. 1 further supports the use of lesion-individual densities for mass scaling of TSV.

So far, 3D voxel-wise dosimetry calculations using VSVs were mainly applied in settings with heterogeneous activity distributions in homogeneous density distributions. For these implementations, a high agreement for tumor absorbed doses obtained from VSVs for soft tissue and MC simulation for soft tissue lesions was reported. Grimes et al. [24] reported only $-1.5\% \pm 4.6\%$ difference for Lu-177, and Dieudonné et al. [45] stated -0.33% difference for Yttrium-90 (Y-90) and -0.15% difference for I-131 for a hepatic tumor phantom. In general, VSV dosimetry calculations can account for heterogeneous activity distributions but not for density differences since they were simulated for a single homogeneous medium. For the

majority of organs and lesions in the abdomen, only small density variations are assumed and a VSV^{soft} approach can therefore be safely used in the clinical setting. However, the assumption mentioned above has to be questioned in situations with large local tissue density changes. Thus, an adapted absorbed dose estimation approach becomes necessary for bone lesions in mCRPC patients. Based on our results for 3D voxel-wise absorbed dose calculations, we observed that both approaches, the utilization of single soft tissue VSVs (VSV^{soft}) and of separate VSVs for soft tissue and bone ($VSV^{\text{soft+bone}}$), reveal limitations in estimation of absorbed dose in bone lesions. Investigating the PD^{vox} revealed on average a strong overestimation by $+ 18 \pm 11\%$ (min: $- 27\%$; max: $+ 58\%$) for VSV^{soft} . $VSV^{\text{soft+bone}}$ on the other hand still showed limited capability of adequately estimating the absorbed dose per bone lesion; it exhibited a large underestimation of absorbed dose by $- 34 \pm 6\%$ (min: $- 60\%$; max: $+ 5\%$). These observations may be explained by the underestimated tissue density, which is an inherent characteristic of the soft tissue voxel absorbed dose kernel VSV^{soft} , compared to the actual bone lesion density. Therefore, this underestimation of voxel density results in an underestimation of the voxel's mass and consequently in an overestimation of the absorbed dose per voxel. On the other hand, $VSV^{\text{soft+bone}}$ relies on the assumption that bone lesions consist merely out of the cortical bone, although a bone lesion can have different components and densities [46]. In this case, a larger mass than the actual lesion mass is assumed, and consequently, the observed absorbed dose is artificially smaller.

The VSV dosimetry methods with subsequent density weighting, as investigated in our study, seem to better address voxel-wise density changes and may therefore yield improved comparability with MC simulation. The proposed methods $VSV_{\text{weighted}}^{\text{soft}}$ and $VSV_{\text{weighted}}^{\text{soft+bone}}$ led to significantly reduced PD^{vox} compared to Monte Carlo simulation, with an underestimation of on average $- 5 \pm 1\%$ (min: $- 12\%$; max: $- 2\%$) and $- 2 \pm 1\%$ (min: $- 9\%$; max: 0%), respectively. These findings are supported by the Bland-Altman plots for D50 in Fig. 4c and d, obeying the smallest spread of data points and smallest mean relative difference compared to the MC method. Further, the majority of data points is within the 95% limits of agreement, given by the red lines. This observation is in concordance with Dieudonné et al. [23], who reported improved absorbed dose agreement for a density corrected VSV approach compared to full MC 3D voxel-wise dosimetry for three clinical cases with focus on soft tissue. Dieudonné et al. observed a lesion absorbed dose difference for a I-131-Tositumomab case of $- 3.1\%$, an organ absorbed dose difference of maximum $- 1.1\%$ for a Lu-177-peptide case, and an organ absorbed dose difference of maximum $+ 0.8\%$ for a Y-90-microspheres case. Besides, Lee et al. [36] noted an overall improvement of whole-body absorbed dose estimates when introducing multiple tissue-specific VSVs, when compared to the utilization of a single tissue VSV. However, our results for bone lesion dosimetry indicate that the effect of additional density weighting onto a single VSV ($VSV_{\text{weighted}}^{\text{soft}}$ compared to VSV^{soft}) outperformed the effect of adding multiple VSVs for various tissues without density weighting ($VSV^{\text{soft+bone}}$ compared to VSV^{soft}). In this work, VSVs were derived for a homogenous tissue. Hence, the application of absorbed dose kernel convolution approaches has limitations if neighboring voxels consist of different tissues. Due to the small maximum range of the β^- particles of Lu-177 in soft tissue of 2 mm [15], and given the voxel size of $(4.7952 \text{ mm})^3$ in this investigation,

we expected this effect to be small when compared to the other effects investigated herein. In our study, we attempted to compensate for tissue differences with the proposed voxel-wise density weighting. Nevertheless, the magnitude of absorbed dose variations related to particle transport across tissue borders with respect to VSV methods requires further investigation.

3D voxel-wise dosimetry offers the visualization of regional variations in lesion absorbed dose estimates on a voxel level. The drawback of 3D voxel-wise dosimetry methods is that individual voxels can be influenced by image artifacts and noise. Further, the limited resolution of SPECT imaging leads to a spill-over of reconstructed activity between structures. Thus, the reconstructed 3D activity distribution does not fully represent a purely physiological activity distribution pattern and has to be interpreted with care. The development and potential amelioration to handle intra-skeletal partial-volume and spill-over compensation techniques should therefore be subject for future investigations. Within this work, we aimed at reducing the impact of the aforementioned effects by using quantitative SPECT reconstruction including distant-dependent point spread function of the detector and a hybrid VOI/voxel-wise approach to reduce the impact of noise and image artifacts on the determination of the time-integrated activity images which serve as an input for the 3D voxel-wise dosimetry methods. The applicability of density weighting is further limited to the CT resolution, and is thus not capable to account for heterogeneities on the sub-millimeter scale. In addition, co-registration of the 24 h, 48 h, and 72 h SPECT and CT images could potentially influence the absorbed dose estimates. This becomes relevant with regard to the outliers with small average lesion densities in Fig. 1, which represent lesions located in the ribs, with challenging co-registration due to breathing, patient's motion, and less reproducible patient positioning between the image acquisitions from day to day. The different steps required for dosimetry include quantitative patient imaging, co-registration, segmentation, fitting, and time-integrated activity assessment, before any absorbed dose estimation can be made [47]. This work concentrated solely on this last step of absorbed dose estimation. The pre-processing was the same for all herein presented dosimetry methods, and thus, possible mistakes in the pre-processing would impact all methods equally.

Conclusions

In our study of 289 bone lesions in mCRPC patients receiving Lu-177-PSMA-I&T therapy, the proposed voxel S value dosimetry approach with subsequent voxel-wise density weighting was associated with comparable absorbed dose estimates for bone lesions as obtained with full patient-individual Monte Carlo absorbed dose simulation. It therefore has the potential to enable routine patient-individual 3D voxel-wise dosimetry evaluations. Further, TSV approaches using lesion-individual average density for mass scaling provide fast and accurate average bone lesion absorbed dose estimates.

Abbreviations

mCRPC: Metastatic, castration-resistant prostate carcinoma; PSMA: Prostate-specific membrane antigen; Lu-177: Lutetium-177; TSV: Tumor S value; VSV: Voxel S value; 3D: Three-dimensional; MC: Monte Carlo; p.i.: Post injection; FOV: Field of view; VOI: Volume of interest; HU: Hounsfield Unit; MIRD: Medical Internal Radiation Dose; ICRP: International Commission On Radiological Protection; PD: Percentage difference; I-131: Iodine-131; Y-90: Yttrium-90; Ra-223: Radium-223; D25: Minimum absorbed dose to 25 % of lesion VOI volume; D50: Minimum absorbed dose to 50 % of lesion VOI volume; D75: Minimum absorbed dose to 75 % of lesion VOI volume

Acknowledgements

We would like to thank Dr. François Bénard for facilitating the collaboration between LMU and BC Cancer (Vancouver, Canada). Special thanks to all technologists at the Department of Nuclear Medicine, University Hospital, LMU Munich for their participation in data collection. This is in memoriam of Dr. Anna Celler who sadly passed away during finalization of this publication. She was a pioneer in quantitative and dynamic SPECT imaging and further was considered as a leading expert in dosimetry. She was not only an outstanding researcher in her field; she was also an excellent teacher and took incomparable care of those whom she supervised. By personally caring for her students, she had and will continuously have great impact on their personal and professional lives.

Authors' contributions

JB, CU, AG, LK, AT, HI, PB, AR, AC, SZ, and GB designed the concept of the study. FG was responsible for the radiopharmaceutical production. JB, AG, AT, HI, and GB reviewed the clinical data for dosimetry. All data analysis was carried out by JB, CU, AG, and GB. All authors contributed to the drafting of the manuscript, and all authors read and approved the final manuscript.

Funding

This work was partly funded by the German Research Foundation (DFG) within the Research Training Group GRK 2274. Open Access funding enabled and organized by Projekt DEAL.

Availability of data and materials

Please contact author for data requests.

Declarations

Ethics approval and consent to participate

This study is based on retrospective and anonymized data, which was acquired for routine clinical dosimetry (Ethics Committee of LMU Munich 20-520).

Consent for publication

Not applicable.

Competing interests

The authors declare that they have no competing interest.

Author details

¹Department of Nuclear Medicine, University Hospital, LMU Munich, Marchioninistrasse 15, 81377 Munich, Germany. ²PET Functional Imaging, BC Cancer, 600 West 10th Avenue, Vancouver, BC V5Z 4E6, Canada. ³Department of Radiology, University of British Columbia, 2775 Laurel Street, Vancouver, BC V5Z 1M9, Canada. ⁴Department of Integrative Oncology, BC Cancer Research Centre, 675 West 10th Avenue, Vancouver, BC V5Z 1L3, Canada.

Received: 23 October 2020 Accepted: 23 February 2021

Published online: 12 March 2021

References

1. Torre LA, Siegel RL, Ward EM, Jemal A. Global cancer incidence and mortality rates and trends—an update. *Cancer Epidemiol Prevent Biomark*. 2016;25(1):16–27.
2. Zhou CK, Check DP, Lortet-Tieulent J, Laversanne M, Jemal A, Ferlay J, et al. Prostate cancer incidence in 43 populations worldwide: an analysis of time trends overall and by age group. *Int J Cancer*. 2016;138(6):1388–400.
3. Gosewisch A, Ilhan H, Tattenberg S, Mairani A, Parodi K, Brosch J, et al. 3D Monte Carlo bone marrow dosimetry for Lu-177-PSMA therapy with guidance of non-invasive 3D localization of active bone marrow via Tc-99m-anti-granulocyte antibody SPECT/CT. *EJNMMI Res*. 2019;9(1):76.
4. Kratochwil C, Fendler WP, Eiber M, Baum R, Bozkurt MF, Czernin J, et al. EANM procedure guidelines for radionuclide therapy with 177 Lu-labelled PSMA-ligands (177 Lu-PSMA-RLT). *Eur J Nuclear Med Mol Imaging*. 2019;46(12):2536–44.
5. Delker A, Fendler WP, Kratochwil C, Brunegrab A, Gosewisch A, Gildehaus FJ, et al. Dosimetry for 177 Lu-DKFZ-PSMA-617: a new radiopharmaceutical for the treatment of metastatic prostate cancer. *Eur J Nuclear Med Mol Imaging*. 2016;43(1):42–51.
6. Okamoto S, Thieme A, Allmann J, D'Alessandria C, Maurer T, Retz M, et al. Radiation dosimetry for 177Lu-PSMA I&T in metastatic castration-resistant prostate cancer: absorbed dose in normal organs and tumor lesions. *J Nuclear Med*. 2017;58(3):445–50.
7. Fendler WP, Reinhardt S, Ilhan H, Delker A, Böning G, Gildehaus FJ, et al. Preliminary experience with dosimetry, response and patient reported outcome after 177Lu-PSMA-617 therapy for metastatic castration-resistant prostate cancer. *Oncotarget*. 2017;8(2):3581.
8. Violet J, Jackson P, Ferdinandus J, Sandhu S, Akhurst T, Iravani A, et al. Dosimetry of 177Lu-PSMA-617 in metastatic castration-resistant prostate cancer: correlations between pretherapeutic imaging and whole-body tumor dosimetry with treatment outcomes. *J Nuclear Med*. 2019;60(4):517–23.
9. Baum RP, Kulkarni HR, Schuchardt C, Singh A, Wirtz M, Wiessalla S, et al. Lutetium-177 PSMA radioligand therapy of metastatic castration-resistant prostate cancer: safety and efficacy. *J Nuclear Med*. 2016;115:168443.
10. Kratochwil C, Giesel FL, Stefanova M, Benešová M, Bronzel M, Afshar-Oromieh A, et al. PSMA-targeted radionuclide therapy of metastatic castration-resistant prostate cancer with 177Lu-labeled PSMA-617. *J Nuclear Med*. 2016;57(8):1170–6.

11. Yadav MP, Ballal S, Tripathi M, Damle NA, Sahoo RK, Seth A, et al. Post-therapeutic dosimetry of ¹⁷⁷Lu-DKFZ-PSMA-617 in the treatment of patients with metastatic castration-resistant prostate cancer. *Nuclear Med Commun*. 2017;38(1):91–8.
12. Seltzer S, Bartlett D, Burns D, Dietze G, Menzel H, Paretzke H, et al. ICRU report 85 fundamental quantities and units for ionizing radiation. *J ICRU*. 2011;11(1):1–31.
13. Snyder W, Ford M, Warner G, Watson S. MIRD pamphlet no. 11. The Society of Nuclear Medicine, New York; 1975. p. 92–3.
14. Stabin MG, Siegel JA. RADAR dose estimate report: a compendium of radiopharmaceutical dose estimates based on OLINDA/EXM version 2.0. *J Nuclear Med*. 2018;59(1):154–60.
15. Cremonesi M, Ferrari M, Bodei L, Tosi G, Paganelli G. Dosimetry in peptide radionuclide receptor therapy: a review. *J Nuclear Med*. 2006;47(9):1467–75.
16. Howell RW, Wessels BW, Loevinger R, Committee M. The MIRD perspective 1999. *J Nuclear Med*. 1999;40(1):35–105.
17. Bolch WE, Bouchet LG, Robertson JS, Wessels BW, Siegel JA, Howell RW, et al. MIRD pamphlet no. 17: the dosimetry of nonuniform activity distributions—radionuclide S values at the voxel level. *J Nuclear Med*. 1999; 40(1):115–365.
18. Sohlberg A, Watabe H, Iida H. Acceleration of Monte Carlo-based scatter compensation for cardiac SPECT. *Phys Med Biol*. 2008;53(14):N277.
19. Kangasmaa T, Sohlberg A, Kuikka JT. Reduction of collimator correction artefacts with bayesian reconstruction in spect. *Int J Mol Imaging*. 2011;2011(Article ID 630813):6. <https://doi.org/10.1155/2011/630813>.
20. Ljungberg M, Celler A, Konijnenberg MW, Eckerman KF, Dewaraja YK, Sjögreen-Gleisner K. MIRD pamphlet no. 26: joint EANM/MIRD guidelines for quantitative ¹⁷⁷Lu SPECT applied for dosimetry of radiopharmaceutical therapy. *J Nuclear Med*. 2016;57(1):151–62.
21. Dewaraja YK, Frey EC, Sgouros G, Brill AB, Roberson P, Zanzonico PB, et al. MIRD pamphlet no. 23: quantitative SPECT for patient-specific 3-dimensional dosimetry in internal radionuclide therapy. *J Nuclear Med*. 2012;53(8):1310–25.
22. Schneider W, Bortfeld T, Schlegel W. Correlation between CT numbers and tissue parameters needed for Monte Carlo simulations of clinical dose distributions. *Phys Med Biol*. 2000;45(2):459.
23. Dieudonné A, Hobbs RF, Lebtahi R, Maurel F, Baechler S, Wahl RL, et al. Study of the impact of tissue density heterogeneities on 3-dimensional abdominal dosimetry: comparison between dose kernel convolution and direct Monte Carlo methods. *J Nuclear Med*. 2013;54(2):236–43.
24. Grimes J, Celler A. Comparison of internal dose estimates obtained using organ-level, voxel S value, and Monte Carlo techniques. *Med Phys*. 2014;41(9):092501.
25. Papadimitroulas P. Dosimetry applications in GATE Monte Carlo toolkit. *Phys Med*. 2017;41:136–40.
26. Papadimitroulas P, Loudos G, Nikiforidis GC, Kagadis GC. A dose point kernel database using GATE Monte Carlo simulation toolkit for nuclear medicine applications: Comparison with other Monte Carlo codes. *Med Phys*. 2012;39(8):5238–47.
27. Sarrut D, Bardiès M, Bousson N, Freud N, Jan S, Létang JM, et al. A review of the use and potential of the GATE Monte Carlo simulation code for radiation therapy and dosimetry applications. *Med Phys*. 2014;41(6Part1):064031.
28. Kondev F. Nuclear Data Sheets for A= 177. *Nuclear Data Sheets*. 2019;159:1–412.
29. Stabin MG, da Luz LC. Decay data for internal and external dose assessment. *Health Phys*. 2002;83(4):471–5.
30. Chetty IJ, Rosu M, Kessler ML, Fraass BA, Ten Haken RK, McShan DL. Reporting and analyzing statistical uncertainties in Monte Carlo-based treatment planning. *Int J Radiation Oncol Biol Phys*. 2006;65(4):1249–59.
31. Lassmann M, Chiesa C, Flux G, Bardiès M. EANM Dosimetry Committee guidance document: good practice of clinical dosimetry reporting. *Eur J Nuclear Med Mol Imaging*. 2011;38(1):192–200.
32. Stabin MG, Sparks RB, Crowe E. OLINDA/EXM: the second-generation personal computer software for internal dose assessment in nuclear medicine. *J Nuclear Med*. 2005;46(6):1023–7.
33. NIST National Institute of Standards and Technology. <https://physics.nist.gov/cgi-bin/Star/compos.pl>. Accessed 30 Mar 2020
34. McConnell RJ, Gesh CJ, Pagh RT, Rucker RA, Williams R III. Compendium of material composition data for radiation transport modeling. Richland: Pacific Northwest National Lab.(PNNL); 2011.
35. Lee MS, Kim JH, Paeng JC, Kang KW, Jeong JM, Lee DS, et al. Whole-body voxel-based personalized dosimetry: the multiple voxel S-value approach for heterogeneous media with nonuniform activity distributions. *J Nuclear Med*. 2018;59(7):1133–9.
36. International Commission on Radiation Units and Measurements. Quantification and Reporting of Low-dose and Other Heterogeneous Exposures. Oxford: Oxford University Press; 2011;11(2011):1–77.
37. Bland JM, Altman DG. Statistical methods for assessing agreement between two methods of clinical measurement. *Int J Nurs Stud*. 2010;47(8):931–6.
38. Bland JM, Altman DG. Measuring agreement in method comparison studies. *Stat Methods Med Res*. 1999;8(2):135–60.
39. Ibrahim T, Flamini E, Mercatali L, Sacanna E, Serra P, Amadori D. Pathogenesis of osteoblastic bone metastases from prostate cancer. *Cancer*. 2010;116(6):1406–18.
40. Howard DM, Kearfott KJ, Wilderman SJ, Dewaraja YK. Comparison of I-131 radioimmunotherapy tumor dosimetry: unit density sphere model versus patient-specific Monte Carlo calculations. *Cancer Biother Radiopharm*. 2011;26(5):615–21.
41. Divoli A, Chiavassa S, Ferrer L, Barbet J, Flux GD, Bardiès M. Effect of patient morphology on dosimetric calculations for internal irradiation as assessed by comparisons of Monte Carlo versus conventional methodologies. *J Nuclear Med*. 2009;50(2):316–23.
42. Amato E, Cicone F, Auditore L, Baldari S, Prior JO, Gnesin S. A Monte Carlo model for the internal dosimetry of choroid plexuses in nuclear medicine procedures. *Phys Med*. 2018;49:52–7.
43. Pacilio M, Ventroni G, De Vincentis G, Cassano B, Pellegrini R, Di Castro E, et al. Dosimetry of bone metastases in targeted radionuclide therapy with alpha-emitting ²²³Ra-dichloride. *Eur J Nuclear Med Mol Imaging*. 2016;43(1):21–33.
44. Cristy M, Eckerman K. Specific Absorbed fractions of energy at various ages from internal photon sources: 1, Methods. TN (USA): Oak Ridge National Lab; 1987.

45. Dieudonné A, Hobbs RF, Bolch WE, Sgouros G, Gardin I. Fine-resolution voxel S values for constructing absorbed dose distributions at variable voxel size. *J Nuclear Med.* 2010;51(10):1600–7.
46. Hough M, Johnson P, Rajon D, Jokisch D, Lee C, Bolch W. An image-based skeletal dosimetry model for the ICRP reference adult male—internal electron sources. *Phys Med Biol.* 2011;56(8):2309.
47. Mora-Ramirez E, Santoro L, Cassol E, Ocampo-Ramos JC, Clayton N, Kayal G, et al. Comparison of commercial dosimetric software platforms in patients treated with ¹⁷⁷Lu-DOTATATE for peptide receptor radionuclide therapy. *Med Phys.* 2020; 47(9):4602–15.

Publisher's Note

Springer Nature remains neutral with regard to jurisdictional claims in published maps and institutional affiliations.

Submit your manuscript to a SpringerOpen[®] journal and benefit from:

- ▶ Convenient online submission
- ▶ Rigorous peer review
- ▶ Open access: articles freely available online
- ▶ High visibility within the field
- ▶ Retaining the copyright to your article

Submit your next manuscript at ▶ [springeropen.com](https://www.springeropen.com)

Bibliography

- [1] B. Barnes, K. Kraywinkel, E. Nowossadeck *et al.* “Bericht zum Krebsgeschehen in Deutschland 2016” (2016).
- [2] S. Hermann and K. Kraywinkel. “Epidemiologie des Prostatakarzinoms in Deutschland”. *Der Onkologe* 25, 294–303 (2019).
- [3] I. Schönfeld and K. Kraywinkel. “Epidemiologie des hepatozellulären Karzinoms in Deutschland”. *Der Onkologe* 24, 653–658 (2018).
- [4] D. V. Becker and C. T. Sawin. “Radioiodine and thyroid disease: the beginning”. In *Seminars in nuclear medicine*, vol. 26, 155–164 (Elsevier, 1996).
- [5] D. Hellwig, J. Marienhagen, K. Menhart and J. Grosse. “Nuklearmedizin in Deutschland”. *Nuklearmedizin* 56, 55–68 (2017).
- [6] K. S. Gleisner, E. Spezi, P. Solny *et al.* “Variations in the practice of molecular radiotherapy and implementation of dosimetry: results from a European survey”. *EJNMMI physics* 4, 28 (2017).
- [7] H. Ahmadzadehfar, K. Rahbar, S. Kürpig *et al.* “Early side effects and first results of radioligand therapy with ¹⁷⁷Lu-DKFZ-617 PSMA of castrate-resistant metastatic prostate cancer: a two-centre study”. *EJNMMI research* 5, 36 (2015).
- [8] A. Kennedy. “Radioembolization of hepatic tumors”. *Journal of gastrointestinal oncology* 5, 178 (2014).
- [9] D. Hörsch, S. Ezziddin, A. Haug *et al.* “Effectiveness and side-effects of peptide receptor radionuclide therapy for neuroendocrine neoplasms in Germany: a multi-institutional registry study with prospective follow-up”. *European Journal of Cancer* 58, 41–51 (2016).
- [10] R. P. Baum, H. R. Kulkarni, C. Schuchardt *et al.* “Lutetium-177 PSMA radioligand therapy of metastatic castration-resistant prostate cancer: safety and efficacy”. *Journal of Nuclear Medicine* jnumed–115 (2016).
- [11] E. Commission. “Council Directive 2013/59/Euratom of 5 December 2013 laying down basic safety standards for protection against the dangers arising from exposure to ionising radiation, and repealing Directives 89/618/Euratom, 90/641/Euratom, 96/29/Euratom, 97/43/Euratom and 2003/122/Euratom”. *Official Journal of the European Union* (2014).
- [12] M. C. Joiner and A. J. van der Kogel. *Basic clinical radiobiology* (CRC press, 2018).

- [13] J. E. Turner. *Atoms, radiation, and radiation protection* (John Wiley & Sons, 2008).
- [14] R. Mori, Y. Matsuya, Y. Yoshii and H. Date. “Estimation of the radiation-induced DNA double-strand breaks number by considering cell cycle and absorbed dose per cell nucleus”. *Journal of radiation research* 59, 253–260 (2018).
- [15] M. Lomax, L. Folkes and P. O’neill. “Biological consequences of radiation-induced DNA damage: relevance to radiotherapy”. *Clinical oncology* 25, 578–585 (2013).
- [16] M. Cremonesi, M. Ferrari, L. Bodei, G. Tosi and G. Paganelli. “Dosimetry in peptide radionuclide receptor therapy: a review”. *Journal of nuclear medicine* 47, 1467–1475 (2006).
- [17] C. F. Perry, P. Zhang, F. B. Nunes *et al.* “Ionization Energy of Liquid Water Revisited”. *The Journal of Physical Chemistry Letters* 11, 1789–1794 (2020).
- [18] H. Krieger. *Grundlagen der Strahlungsphysik und des Strahlenschutzes*, vol. 2 (Springer, 2007).
- [19] S. S. Kelkar and T. M. Reineke. “Theranostics: combining imaging and therapy”. *Bioconjugate chemistry* 22, 1879–1903 (2011).
- [20] F. Giammarile, L. Bodei, C. Chiesa *et al.* “EANM procedure guideline for the treatment of liver cancer and liver metastases with intra-arterial radioactive compounds”. *European journal of nuclear medicine and molecular imaging* 38, 1393 (2011).
- [21] C. Kratochwil, W. P. Fendler, M. Eiber *et al.* “EANM procedure guidelines for radionuclide therapy with ^{177}Lu -labelled PSMA-ligands (^{177}Lu -PSMA-RLT)”. *European Journal of Nuclear Medicine and Molecular Imaging* 46, 2536–2544 (2019).
- [22] A. Saini, A. Wallace, S. Alzubaidi *et al.* “History and evolution of Yttrium-90 radioembolization for hepatocellular carcinoma”. *Journal of Clinical Medicine* 8, 55 (2019).
- [23] M. Raval, D. Bande, A. K. Pillai *et al.* “Yttrium-90 radioembolization of hepatic metastases from colorectal cancer”. *Frontiers in oncology* 4, 120 (2014).
- [24] D. D’Avola, M. Lnarrairaegui, J. I. Bilbao *et al.* “A retrospective comparative analysis of the effect of Y90-radioembolization on the survival of patients with unresectable hepatocellular carcinoma.”. *Hepato-gastroenterology* 56, 1683–1688 (2009).
- [25] S. A. Gulec, G. Mesoloras, W. A. Dezarn, P. McNeillie and A. S. Kennedy. “Safety and efficacy of Y-90 microsphere treatment in patients with primary and metastatic liver cancer: the tumor selectivity of the treatment as a function of tumor to liver flow ratio”. *Journal of translational medicine* 5, 15 (2007).
- [26] A. J. Braat, M. L. Smits, M. N. Braat *et al.* “ ^{90}Y hepatic radioembolization: an update on current practice and recent developments”. *Journal of Nuclear Medicine* 56, 1079–1087 (2015).

- [27] S. P. Kim, C. Cohalan, N. Kopek and S. A. Enger. “A guide to ^{90}Y radioembolization and its dosimetry”. *Physica Medica* 68, 132–145 (2019).
- [28] A. Kennedy, S. Nag, R. Salem *et al.* “Recommendations for radioembolization of hepatic malignancies using yttrium-90 microsphere brachytherapy: a consensus panel report from the radioembolization brachytherapy oncology consortium”. *International Journal of Radiation Oncology* Biology* Physics* 68, 13–23 (2007).
- [29] K. Liu, X. Zhang, W. Xu *et al.* “Targeting the vasculature in hepatocellular carcinoma treatment: Starving versus normalizing blood supply”. *Clinical and translational gastroenterology* 8, e98 (2017).
- [30] M. G. Stabin and J. A. Siegel. “RADAR dose estimate report: a compendium of radiopharmaceutical dose estimates based on OLINDA/EXM version 2.0”. *Journal of Nuclear Medicine* 59, 154–160 (2018).
- [31] R. S. Israeli, C. T. Powell, J. G. Corr, W. R. Fair and W. D. Heston. “Expression of the prostate-specific membrane antigen”. *Cancer research* 54, 1807–1811 (1994).
- [32] F. De Felice, A. Piccioli, D. Musio and V. Tombolini. “The role of radiation therapy in bone metastases management”. *Oncotarget* 8, 25691 (2017).
- [33] D. Sarrut, M. Bardiès, N. Boussion *et al.* “A review of the use and potential of the GATE Monte Carlo simulation code for radiation therapy and dosimetry applications”. *Medical physics* 41, 064301 (2014).
- [34] S. Seltzer, D. Bartlett, D. Burns *et al.* “ICRU report 85: Fundamental quantities and units for ionizing radiation”. *J. ICRU* 11 (2011).
- [35] G. Sgouros, E. Frey, R. Wahl *et al.* “Three-dimensional imaging-based radiobiological dosimetry”. In *Seminars in nuclear medicine*, vol. 38, 321–334 (Elsevier, 2008).
- [36] D. Bailey, J. Humm, A. Todd-Pokropek and A. v. Aswegen. “Nuclear Medicine Physics: A Handbook for Teachers and Students.”. *IAEA* (2014).
- [37] Y. K. Dewaraja, E. C. Frey, G. Sgouros *et al.* “MIRD pamphlet no. 23: quantitative SPECT for patient-specific 3-dimensional dosimetry in internal radionuclide therapy”. *Journal of Nuclear Medicine* 53, 1310–1325 (2012).
- [38] A. Delker, H. Ilhan, C. Zach *et al.* “The influence of early measurements onto the estimated kidney dose in [^{177}Lu][DOTA 0, Tyr 3] Octreotate peptide receptor radiotherapy of neuroendocrine tumors”. *Molecular imaging and biology* 17, 726–734 (2015).
- [39] S. R. Cherry, J. A. Sorenson and M. E. Phelps. *Physics in nuclear medicine e-Book* (Elsevier Health Sciences, 2012).
- [40] P. Suetens. *Fundamentals of medical imaging* (Cambridge university press, 2017).
- [41] J. A. Siegel, S. R. Thomas, J. B. Stubbs *et al.* “MIRD pamphlet no. 16: techniques for quantitative radiopharmaceutical biodistribution data acquisition and analysis for use in human radiation dose estimates”. *Journal of Nuclear Medicine* 40, 375–61S (1999).

- [42] J. Grimes and A. Celler. “Comparison of internal dose estimates obtained using organ-level, voxel S value, and Monte Carlo techniques”. *Medical physics* 41, 092501 (2014).
- [43] W. Snyder, M. R. Ford, G. Warner and S. Watson. “MIRD pamphlet no. 11: S, absorbed dose per unit cumulated activity for selected radionuclides and organs”. *New York: Society of Nuclear Medicine* (1975).
- [44] W. E. Bolch, L. G. Bouchet, J. S. Robertson *et al.* “MIRD pamphlet no. 17: the dosimetry of nonuniform activity distributions—radionuclide S values at the voxel level”. *Journal of Nuclear Medicine* 40, 11S–36S (1999).
- [45] M. Andersson, L. Johansson, K. Eckerman and S. Mattsson. “IDAC-Dose 2.1, an internal dosimetry program for diagnostic nuclear medicine based on the ICRP adult reference voxel phantoms”. *EJNMMI research* 7, 88 (2017).
- [46] R. W. Howell, B. W. Wessels, R. Loevinger, M. Committee *et al.* “The MIRD perspective 1999”. *Journal of Nuclear Medicine* 40, 3S–10S (1999).
- [47] F. Botta, A. Mairani, R. Hobbs *et al.* “Use of the FLUKA Monte Carlo code for 3D patient-specific dosimetry on PET-CT and SPECT-CT images”. *Physics in Medicine & Biology* 58, 8099 (2013).
- [48] W. Schneider, T. Bortfeld and W. Schlegel. “Correlation between CT numbers and tissue parameters needed for Monte Carlo simulations of clinical dose distributions”. *Physics in Medicine & Biology* 45, 459 (2000).
- [49] S. Jan, G. Santin, D. Strul *et al.* “GATE: a simulation toolkit for PET and SPECT”. *Physics in Medicine & Biology* 49, 4543 (2004).
- [50] P. Papadimitroulas. “Dosimetry applications in GATE Monte Carlo toolkit”. *Physica Medica* 41, 136–140 (2017).
- [51] K. Kossert and H. Schrader. “Activity standardization by liquid scintillation counting and half-life measurements of ^{90}Y ”. *Applied radiation and isotopes* 60, 741–749 (2004).
- [52] Y.-H. Kao, J. D. Steinberg, Y.-S. Tay *et al.* “Post-radioembolization yttrium-90 PET/CT-part 1: diagnostic reporting”. *EJNMMI research* 3, 1 (2013).
- [53] M. D’Arienzo. “Emission of β^+ particles via internal pair production in the $0^+ \rightarrow 0^+$ transition of ^{90}Zr : historical background and current applications in nuclear medicine imaging”. *Atoms* 1, 2–12 (2013).
- [54] R. Selwyn, R. Nickles, B. Thomadsen, L. DeWerd and J. Micka. “A new internal pair production branching ratio of ^{90}Y : the development of a non-destructive assay for ^{90}Y and ^{90}Sr ”. *Applied radiation and isotopes* 65, 318–327 (2007).
- [55] A. Delker, W. P. Fendler, C. Kratochwil *et al.* “Dosimetry for ^{177}Lu -DKFZ-PSMA-617: a new radiopharmaceutical for the treatment of metastatic prostate cancer”. *European journal of nuclear medicine and molecular imaging* 43, 42–51 (2016).

- [56] W. Siman, J. Mikell and S. Kappadath. “Practical reconstruction protocol for quantitative ^{90}Y bremsstrahlung SPECT/CT”. *Medical physics* 43, 5093–5103 (2016).
- [57] J. K. Mikell, A. Mahvash, W. Siman *et al.* “Selective internal radiation therapy with yttrium-90 glass microspheres: biases and uncertainties in absorbed dose calculations between clinical dosimetry models”. *International Journal of Radiation Oncology Biology Physics* 96, 888–896 (2016).
- [58] V. Preylowski, S. Schlögl, F. Schoenahl *et al.* “Is the image quality of I-124-PET impaired by an automatic correction of prompt gammas?”. *PLoS One* 8, e71729 (2013).
- [59] T. Greten, N. Malek, S. Schmidt *et al.* “Diagnostik und Therapie des hepatozellulären Karzinoms”. *Zeitschrift für Gastroenterologie* 51, 1269–1326 (2013).
- [60] J. Brosch, A. Gosewisch, L. Kaiser *et al.* “3D image-based dosimetry for Yttrium-90 radioembolization of hepatocellular carcinoma: Impact of imaging method on absorbed dose estimates”. *Physica Medica* 80, 317–326 (2020).
- [61] A. Gosewisch, H. Ilhan, S. Tattenberg *et al.* “3D Monte Carlo bone marrow dosimetry for Lu-177-PSMA therapy with guidance of non-invasive 3D localization of active bone marrow via Tc-99m-anti-granulocyte antibody SPECT/CT”. *EJNMMI research* 9, 76 (2019).
- [62] M. Hohberg, W. Eschner, M. Schmidt *et al.* “Lacrimal glands may represent organs at risk for radionuclide therapy of prostate cancer with [^{177}Lu] DKFZ-PSMA-617”. *Molecular imaging and biology* 18, 437–445 (2016).
- [63] M. Ljungberg, A. Celler, M. W. Konijnenberg *et al.* “MIRD pamphlet no. 26: joint EANM/MIRD guidelines for quantitative ^{177}Lu SPECT applied for dosimetry of radiopharmaceutical therapy”. *Journal of nuclear medicine* 57, 151–162 (2016).
- [64] L. Vomacka, A. Gosewisch, A. Delker *et al.* “Automatic image segmentation for 3D dosimetry in Lu-177 DKFZ-PSMA-617 therapy of castrate-resistant metastatic prostate cancer using a robust cluster algorithm on 4D SPECT data”. *Journal of Nuclear Medicine* 57, 497–497 (2016).
- [65] T. Ibrahim, E. Flamini, L. Mercatali *et al.* “Pathogenesis of osteoblastic bone metastases from prostate cancer”. *Cancer: Interdisciplinary International Journal of the American Cancer Society* 116, 1406–1418 (2010).
- [66] A. Gosewisch, A. Delker, S. Tattenberg *et al.* “Patient-specific image-based bone marrow dosimetry in Lu-177-[DOTA 0, Tyr 3]-Octreotate and Lu-177-DKFZ-PSMA-617 therapy: investigation of a new hybrid image approach”. *EJNMMI research* 8, 76 (2018).
- [67] S. Okamoto, A. Thieme, J. Allmann *et al.* “Radiation dosimetry for ^{177}Lu -PSMA I&T in metastatic castration-resistant prostate cancer: absorbed dose in normal organs and tumor lesions”. *Journal of Nuclear Medicine* 58, 445–450 (2017).
- [68] W. P. Fendler, S. Reinhardt, H. Ilhan *et al.* “Preliminary experience with dosimetry, response and patient reported outcome after ^{177}Lu -PSMA-617 therapy for metastatic castration-resistant prostate cancer”. *Oncotarget* 8, 3581 (2017).

- [69] C. Kratochwil, F. L. Giesel, M. Stefanova *et al.* “PSMA-targeted radionuclide therapy of metastatic castration-resistant prostate cancer with ^{177}Lu -labeled PSMA-617”. *Journal of Nuclear Medicine* 57, 1170–1176 (2016).
- [70] M. P. Yadav, S. Ballal, M. Tripathi *et al.* “Post-therapeutic dosimetry of ^{177}Lu -DKFZ-PSMA-617 in the treatment of patients with metastatic castration-resistant prostate cancer”. *Nuclear medicine communications* 38, 91–98 (2017).
- [71] A. Dieudonné, R. F. Hobbs, R. Lebtahi *et al.* “Study of the impact of tissue density heterogeneities on 3-dimensional abdominal dosimetry: comparison between dose kernel convolution and direct Monte Carlo methods”. *Journal of nuclear medicine* 54, 236–243 (2013).
- [72] I. R. N. 86. “Quantification and reporting of low-dose and other heterogeneous exposures” (2011).
- [73] L. Strigari, M. Konijnenberg, C. Chiesa *et al.* “The evidence base for the use of internal dosimetry in the clinical practice of molecular radiotherapy”. *European journal of nuclear medicine and molecular imaging* 41, 1976–1988 (2014).
- [74] A. Divoli, S. Chiavassa, L. Ferrer *et al.* “Effect of patient morphology on dosimetric calculations for internal irradiation as assessed by comparisons of Monte Carlo versus conventional methodologies”. *Journal of Nuclear Medicine* 50, 316–323 (2009).
- [75] W. E. Bolch, K. F. Eckerman, G. Sgouros and S. R. Thomas. “MIRD pamphlet no. 21: a generalized schema for radiopharmaceutical dosimetry—standardization of nomenclature”. *Journal of Nuclear Medicine* 50, 477–484 (2009).
- [76] Y. K. Dewaraja, S. Y. Chun, R. N. Srinivasa *et al.* “Improved quantitative ^{90}Y bremsstrahlung SPECT/CT reconstruction with Monte Carlo scatter modeling”. *Medical physics* 44, 6364–6376 (2017).
- [77] X. Hou, J. Brosch, C. Uribe *et al.* “Feasibility of single-time-point dosimetry for radiopharmaceutical therapies”. *Journal of Nuclear Medicine* jnumed–120 (2020).
- [78] K. P. Willowson, E. Eslick, H. Ryu *et al.* “Feasibility and accuracy of single time point imaging for renal dosimetry following ^{177}Lu -DOTATATE (‘Lutate’) therapy”. *EJNMMI physics* 5, 1–9 (2018).
- [79] J. Yue, T. Mauxion, D. K. Reyes *et al.* “Comparison of quantitative Y-90 SPECT and non-time-of-flight PET imaging in post-therapy radioembolization of liver cancer”. *Medical physics* 43, 5779–5790 (2016).
- [80] M. Elschot, B. J. Vermolen, M. G. Lam *et al.* “Quantitative comparison of PET and Bremsstrahlung SPECT for imaging the in vivo yttrium-90 microsphere distribution after liver radioembolization”. *PloS one* 8, e55742 (2013).
- [81] M. Kafrouni, C. Allimant, M. Fourcade *et al.* “Analysis of differences between $^{99\text{m}}\text{Tc}$ -MAA SPECT-and ^{90}Y -microsphere PET-based dosimetry for hepatocellular carcinoma selective internal radiation therapy”. *EJNMMI research* 9, 62 (2019).

-
- [82] P. A. Jackson, M. S. Hofman, R. J. Hicks, M. Scalzo and J. Violet. “Radiation dosimetry in ^{177}Lu -PSMA-617 therapy using a single posttreatment SPECT/CT scan: a novel methodology to generate time-and tissue-specific dose factors”. *Journal of Nuclear Medicine* 61, 1030–1036 (2020).
- [83] C. Chiesa, M. Bardiès and H. Zaidi. “Voxel-based dosimetry is superior to mean-absorbed dose approach for establishing dose-effect relationship in targeted radionuclide therapy”. *Medical physics* 46, 5403–5406 (2019).

List of Figures

1.1	Therapy numbers of ^{90}Y SIRT and ^{177}Lu -PSMA for 2015 compared against 2020 in the university hospital of LMU Munich.	2
1.2	Exemplary patient therapy response on pre- and post-therapeutic PET/CT images.	3
2.1	Different stages within the effect of ionizing radiation on tissue.	5
2.2	Schematic illustration of the concept of "theranostics": simultaneous emission of β^- , used for therapy, and γ , used for imaging.	6
2.3	Patient example showing the therapy response 6 months after ^{90}Y SIRT on the right MR image.	8
2.4	Time frame for ^{90}Y SIRT.	9
2.5	Prostate cancer metastasizes to lymph nodes and into the skeleton as demonstrated by this PSMA PET image of a patient.	10
2.6	Schematic representation of the principle of radioligand therapies.	11
2.7	Required processing steps within the general dosimetry workflow.	12
2.8	Example of the mono-exponential decay of activity when considering the physical half-life.	13
2.9	Illustrations of exemplarily activity values over time.	14
2.10	Photos of a PET/CT and a SPECT/CT in the department of nuclear medicine of the LMU Klinikum.	15
2.11	Patient example of fused CT and SPECT image and defined VOIs for whole-body, kidneys and tumors.	16
2.12	Illustration of the determination of the time-integrated activity \tilde{A} per organ or per voxel.	17
2.13	MIRD organ S value scheme: a source organ with homogeneous activity distribution yields a self irradiation of the source organ and a cross irradiation of other target organs.	19
2.14	Simplified representation of the concept of VSVs: a central source voxel irradiates a target voxel. The central source voxel of course irradiates itself and all surrounding voxels.	20
2.15	Simplified representation of a MC absorbed dose simulation set-up. TIAM: time-integrated activity map.	21
3.1	Photon spectrum of a ^{90}Y sample in a germanium detector.	24
3.2	^{90}Y SIRT activity images from different imaging modalities and with different reconstruction parameter choice.	25
3.3	Required processing steps within the general dosimetry workflow, modified for ^{90}Y SIRT.	26

3.4	NEMA IEC Body Phantom Set TM	27
3.5	Transversal slices of the ⁹⁰ Y BRS SPECT phantom image for different sphere-to-background ratios.	30
3.6	Transversal slices of the ⁹⁰ Y PET phantom image for different sphere-to-background ratios.	30
3.7	Results of ⁹⁰ Y PET and ⁹⁰ Y phantom measurements with different sphere-to-background ratios.	31
3.8	Required processing steps within the general dosimetry workflow, modified for ⁹⁰ Y SIRT.	32
3.9	RC and SNR of the four largest spheres of the NEMA IEC Body Phantom Set TM obtained from measurements with the identified patient acquisition and reconstruction parameters for ⁹⁰ Y BRS SPECT, ^{99m} Tc SPECT, and ⁹⁰ Y PET.	35
3.10	Absorbed dose estimates for healthy liver and tumor for all three investigated imaging modalities.	36
3.11	Density map of a mCRPC patient showing the increase in density in the metastasis in the vertebrae and very comparable densities in the soft tissue regions of the abdomen.	38
3.12	Percentage differences in average time-integrated activity per lesion VOI, obtained from QSPECT compared against the reference \bar{A}^{VOI}	40
3.13	Processing steps within the dosimetry workflow of ¹⁷⁷ Lu-PSMA therapy.	41
3.14	Percentage difference of average lesion absorbed dose from TSV methods compared against MC.	44
3.15	Percentage difference compared per voxel and then averaged per lesion VOI.	45
5.1	Pre-therapeutic MR image of a patient suffering from HCC and transversal slices of the 3D absorbed dose maps for ⁹⁰ Y SIRT. Top right: scaled ^{99m} Tc/ ⁹⁰ Y SPECT/CT based; bottom left: ⁹⁰ Y BRS SPECT/CT based; bottom right: ⁹⁰ Y PET/CT based.	52
5.2	Bland-Altman plot for the minimum absorbed dose to 75 % of the bone lesion VOI volume (D75) compared for the 3D voxel-wise dosimetry methods against MC.	53
5.3	Sagittal slices of 3D absorbed dose maps fused with the CT image (b) of a mCRPC patient receiving ¹⁷⁷ Lu-PSMA therapy; (a) shows the result of the full MC simulation; (c) displays the result of the application of voxel S values for soft tissue, weighted with voxel-wise density in (d); (e) stands for the use of voxel S values for soft tissue and cortical bone, and with subsequent voxel-wise density weighting in (f).	54
5.4	DVH of an exemplary bone lesion of a mCRPC patient receiving ¹⁷⁷ Lu-PSMA therapy.	54

List of Tables

2.1	Overview of absorbed dose estimation methods.	18
3.1	NEMA IEC Body Phantom Set TM parameters.	27
3.2	⁹⁰ Y BRS SPECT acquisition parameter; medium-energy-low-penetration (MELP).	28
3.3	RCs of the phantom background for ⁹⁰ Y PET and ⁹⁰ Y BRS SPECT and all sphere-to-background ratios.	30
3.4	PD of healthy liver and tumor absorbed dose estimates from scaled ^{99m} Tc/ ⁹⁰ Y SPECT and ⁹⁰ Y BRS SPECT compared to ⁹⁰ Y PET, averaged over all ten evaluated SIRTs and the minimum and maximum PD per methodology are shown.	35

Danksagung

Mein großer Dank gilt meinem Doktorvater, PD Dr. Guido Böning. Guido, Du hast mich während meiner Uni-Laufbahn vom Bachelor über Master bis hin zur Doktorarbeit begleitet, beraten, stets unterstützt, aufgemuntert, gefordert, gefördert und betreut. Ich danke Dir für all die kritischen Diskussionen, die Hilfestellungen und Deine stets offene Bürotür für Fragen aller Art! Das gemeinsame "Brainstormen" brachte die besten (und verrücktesten) Ideen bis hin zur Verwendung von "Lego Technic" für Phantommessungen. Du bist auch abseits von Forschungsfragen immer für deine Studenten da, nicht zu vergessen, wie Du Dich beim Klinikumsfußballturnier todesmutig vor den Ball geschmissen hast, damit ich im Tor nicht abgeschossen werde! Unseren Lieblingssatz "Kaffee ist fertig" werde ich auch immer in Erinnerung halten.

Frau Prof. Dr. Sibylle Ziegler möchte ich zutiefst für die Betreuung danken. Sie hatten stets ein offenes Ohr und haben mir bei allen Problemen sehr geholfen - ob nun direkt bei Medizinphysik Fragen, dem Publikationsprozess an sich, über das Vermitteln von Kontakten zu Forschungsgruppen auf der ganzen Welt bis hin zu einer Wohnung für meinen Auslandsaufenthalt in Vancouver.

Herrn Prof. Dr. Peter Bartenstein danke ich für die Ermöglichung einer Doktorarbeit in der Klinik und Poliklinik für Nuklearmedizin am Klinikum der Universität München. Zeitgleich ermöglichten Sie mir den Einblick in den klinischen Arbeitsalltag und die Weiterbildung zur Medizinphysikexpertin. Sie setzen sich unermüdlich für Ihre Studenten und Mitarbeiter ein und haben dabei auch stets den Einzelnen im Auge, um die nötige Unterstützung zu bieten und uns zu fördern.

Den NUKis, also dem gesamten Team der Nuklearmedizin, danke ich für all die Freude, die mir mein Arbeitsalltag stets bereitet hat. Astrid, du hast mir fortwährend geholfen und mich in allen Belangen unterstützt und ermutigt, danke Dir. Lena, Christian, Uli, Joe, die gemeinsamen Physikbesprechungen (und die Weißwurstfrühtücke mit Euch) werden mir immer im Gedächtnis bleiben. Ebenfalls großen Dank an "PET/CT-Andi", Isi und das ganze MTRA Team, das mir unheimlich viel über die Kameras, ihre Wehwehchen und Tipps und Tricks beigebracht hat - und die geheime Gummibärenschieblade gezeigt hat. An alle anderen Bachelorstudenten, Masteranden und Doktoranden: wir haben so viel Freude und Leid geteilt - Chrissi, Henny, Karin, Larissa, Mirjam, ich möchte Euch in meinem Leben nicht missen!

Dem Graduiertenkolleg GRK2274 und der Sprecherin Frau Prof. Dr. Katia Parodi spreche ich meinen Dank für die vielfältigen Möglichkeiten innerhalb des Graduiertenkollegs

aus. Die abwechslungsreichen Seminare, die namhaften Gastvortragenden sowie der Austausch mit den anderen Doktoranden ermöglichten mir einen weitreichenden Einblick in die aktuelle Forschung der Medizinphysik. Ich bin sehr dankbar, meine Doktorarbeit in diesem Rahmen, mit dieser Förderung durchführen zu können. Die Kontakte und Freundschaften, die hier geknüpft wurden, werden mich in meinem Leben weiter begleiten.

Anna, I miss you so deeply. I am grateful to have met you during my research stay in Vancouver in 2019. You were a great source of inspiration and motivation. You kept challenging your students to make them learn and develop. You've taught me to critically reflect on my results and to ask for help if needed. Besides the research aspect, you were personally interested in me and I loved our walks through Lynn valley. I can't tell how sad I am, that you will not have the chance to witness the finalization of my PhD thesis. I'll keep the memories of you in my heart and do my best to make you proud.

Dr. Arman Rahmim, I thank you so much for your mentoring during and after my research stay in Vancouver. I am deeply thankful that I had (and will have) the chance to work with you. I especially remember the coaching, that you've offered me to make me personally grow and to improve my working routines. Your way of teaching your students is unique in how you encourage and teach how to focus. My research and daily work routine has immensely benefitted under your advice. Thank you.

Special thanks to Dr. Carlos Uribe, you are very much like Anna. Thank you for your support during my first steps with GATE and the following collaboration project including the tough process of publishing. You were always available for questions, no matter how busy you were. Thanks a lot! I am happy to say that you became a good friend in the meantime and sharing photos of our dogs is always cheering me up.

Mama, Papa, ich danke Euch von ganzem Herzen! Was wäre ich nur ohne Euch? Ihr umsorgt mich, unterstützt mich und seid immer für mich da. Nur dank Euch bin ich, wer ich heute bin und wo ich heute bin. Ich danke auch zutiefst dem Rest meiner Familie, ich bin so froh, dass ich Euch habe.

Tom, ich liebe Dich. Du bist die größte Unterstützung, meine größte Kraftquelle und mein Ruhepol. Du hast mich den ganzen Weg meiner Doktorarbeit begleitet, mit Höhen und Tiefen, mit Freude und Frust, mit Sorgen und Motivation. Ohne Dich hätte ich das nicht geschafft.